

Development of Analytical Methods for Direct Macro Surface Texturing by Metal Laser Powder Bed Fusion



By

Prospera Sonuo Sibanda

March 2023

A Thesis submitted for the Degree of Doctor of Philosophy (Ph.D.)

Supervisors:

Dr Samuel Bigot

Dr Michael Ryan

Acknowledgements

I would like to acknowledge Safran Seats GB and Cardiff University School of Engineering, for supporting this PhD thesis. I would also like to appreciate Samuel Bigot, Michael Ryan, Stuart Watt, Joanna Hutchinson, Peter Carr, Lionel Ridosz, Franck Lacan and Arno Myburgh for their supervision and contribution.

I would like to say thank you to my family Mandla Eric Sibanda, Sindiswa Mikayla Sibanda, Sandile Mawutor Sibanda, Akpene Aboni-Prempeh, Leviel Edna Benni, Maviel Philomena Benni and Daafua Exornam Benni. Thank you for your support and Prayers.

Abstract

Additive Manufacturing (AM) is gaining much attention, particularly for end- use parts in the aerospace industry due to the advantages of the technique to produce complex parts, reduce part count and minimise part cost. Out of the AM techniques, metal Laser Powder Bed Fusion (LPBF) shows promising application to complement traditional manufacturing, specifically within aircraft interior industry where LPBF is attractive for the manufacture of bespoke, high-end luxury suite components. Unfortunately, LPBF suffers major drawback in terms of the surface finish, which can potentially limit its application, particularly with visible aircraft interior application where the surface finish is paramount to part acceptance. Surface texturing can potentially improve the surface finish of LPBF parts; however, this needs to be explored in the context of aircraft interior applications.

Whilst there are methods to design surface textures, there are still uncertainties on the definition of millimeter scale surface features for creating textures. An analytical equation was developed to provide design guidelines for the definition of such features. The results show significant improvement in the prediction accuracy when using the analytical equation compared to experimentation. By adopting the feature widths and spacing predictions for texture creation, individual assessments were conducted to establish a method for assessing the visuo-tactile perception of textured LPBF surfaces.

The main contribution of this thesis is in the development of analytical tools to aid designers to make a quick assessment of the suitability of their surface texture design for a particular LPBF machine/material.

Table of Content

1	Introduction	1
1.1	Motivation	1
1.2	Main Opportunities for LPBF in Aerospace (Aircraft Interiors).....	4
1.3	General Challenges of LPBF in Aerospace (Aircraft Interiors)	5
1.4	Research Aim and Questions	7
1.5	Thesis Structure	8
2	Literature review	9
2.1	Chapter Summary	9
2.2	General Overview of Additive Manufacturing (AM)	9
2.2.1	Categories of Metal AM	10
2.2.2	Overview of LPBF Manufacturing Process.....	12
2.3	Introduction to Surface Textures and Metrology	16
2.3.1	Macro Surface Textures.....	16
2.3.2	Metrology of Surface Textures	19
2.3.3	Surface Measurement.....	19
2.3.4	Surface Characterisation.....	20
2.3.5	Surface Characterisation in Relation to Surface Appearance	22
2.3.6	Techniques for Assessing Surface Appearance.....	23
2.4	Techniques for Surface Finish Improvement of AM Components.	26
2.4.1	Direct Texturing Techniques	26
2.5	Conclusion of Literature Review	35
3	Experimental Methods	37
3.1	Research Objective 1 (Chapter 4)	37
3.2	Research Objective 2 (Chapter 5)	37
3.3	Research Objective 3 (Chapter 6)	38
4	Parametric Approach for Millimeter Scale Feature Width Prediction.....	39
4.1	Summary.....	39

4.2	Introduction.....	39
4.3	Review of Melt-Pool Width Estimation.....	41
4.4	New Metal AM Feature Width prediction Model.....	46
4.4.1	Single Laser Scan Track.....	48
4.4.2	Double Laser Track	50
4.4.3	Case 3: Contouring and Infill Laser Track	51
4.5	Validating the new model using parts produced by LPBF (continuous laser) 54	
4.5.1	Experimental setup	54
4.5.2	Results Summary for Continuous Laser Samples	61
4.5.2.1	Positional Variation in Feature Width (Continuous Laser).....	61
4.5.2.2	Prediction Accuracy with Developed Model.....	65
4.6	New Tuneable Metal AM Feature Width prediction Model	74
4.6.1	Model modified using Optimised Coefficients.....	74
4.6.2	Model modified using coefficients optimised to all LPBF continuous laser data. 75	
4.6.3	Model modified using coefficients optimised using one LPBF continuous laser sample.....	81
4.7	New Model Validation using LPBF Pulse Width Modulated Laser (PWM) ...	86
4.7.1	Parts produced by LPBF (PWM laser)	86
4.7.2	Results Summary for PWM Laser samples	89
4.7.3	Model Prediction using coefficients optimised to all LPBF continuous laser data. 96	
4.7.4	Model prediction with coefficients optimised with all LPBF PWM laser data. 100	
4.7.5	Model coefficients optimised with data from one LPBF pulse laser sample. 107	
4.8	Discussion.....	112
4.9	Conclusion.....	115
5	Assessment of Minimum Spacing between Features produced by LPBF	117

5.1	Geometric Characteristics of Textures	117
5.2	Chapter's Objectives.....	118
5.3	Process Conditions for Minimum Spacing between Features	118
5.3.1	Sum of Squared Ratios.....	118
5.4	Experimentation for Feature Spacing Evaluation (PWM Laser)	123
5.4.1	Sample Design	123
5.4.2	Experimental Setup	128
5.4.3	Sample Measurement Process	129
5.4.4	Sample Data Characterisation	130
5.5	Results	131
5.5.1	Grading Analysis.....	131
5.6	Discussion.....	139
5.7	Conclusion.....	139
6	Aesthetic Evaluation of Textured LPBF Surfaces.....	141
6.1	Aesthetic considerations in LPBF	141
6.2	Chapter's Objectives.....	142
6.3	Textured Samples used for Aesthetic Evaluation	144
6.3.1	Samples Design	144
6.3.2	Samples Manufacturing (LPBF)	146
6.3.3	Post Processing of Samples	148
6.4	Aesthetic assessment.....	150
6.4.1	Method for capturing individual assessors' feedback.	150
6.4.2	Capturing Individual Surface Perception	152
6.5	Individual assessment setup.....	154
6.5.1	Visual Assessments: "Attractive" Adjective	154
6.5.1.1	<i>Batch 1 - As-built vs Polished: "Attractive"</i>	154
6.5.1.2	<i>Batch 2 - Textured vs Plain: "Attractive"</i>	155
6.5.1.3	<i>Batch 3 - Textured vs Plain: Attractive"</i>	156
6.5.2	Tactile Assessment - "Pleasant" Adjective	156

6.5.2.1	<i>Batch 4 - As-built vs Polished</i>	156
6.5.3	Visuo-tactile Assessment – “Preference Adjective”	157
6.5.3.1	<i>Batch 5 – Texture type comparison</i>	157
6.6	Initial Surface Qualitative Assessment	158
6.7	Aesthetic Assessment Results	161
6.7.1	Visual Assessment (Attractive Adjective)	161
6.7.1.1	<i>Textured vs Plain surfaces (polished)</i>	165
6.7.2	Tactile assessment (Pleasant Attribute).....	166
6.7.3	Visio-Tactile assessment: Preference Attribute	167
6.8	Discussion	168
6.9	Conclusion.....	170
7	Conclusion and Future Work	172
7.1	Thesis Summary.....	172
7.2	Contributions to the field	174
7.2.1	Literature review contributions.....	174
7.2.2	Chapter 4’s contribution.....	174
7.2.3	Chapter 5’s contribution.....	175
7.2.4	Chapter 6’s contribution.....	175
7.2.5	Final concluding remarks.....	175
7.3	Recommendation for future work	176
8	References	177
9	Appendix	196
9.1	Appendix 1: Chapter 4	196
9.2	Appendix 2: Chapter 5	199

List of Figures

Figure 1. 1: Stair casing effect on AM spherical part (Shi, 2021)	3
---	---

Figure 1. 2: Aesthetic Geometric Study of dimension 60mm height and 40mm diameter (Galimberti et al., 2015) (a); Structural aerospace bracket (Thales Group, 2019) (b); Titanium aircraft seat buckle (Crucible Design, 2021) (c).....	4
Figure 1. 3: Scopus Database search of publications in metal AM showing trends in aesthetics, mechanical and Design for Additive Manufacturing (DfAM). (Generated by Author)	6
Figure 2. 1: Cut and Stack approach for creating a wzx tool set by Blather (Blather, 1892) (a); Layered metal parts using Cut and Stack approach (Das et al., 2016)..	10
Figure 2. 2: Classification of Metal AM process(Williams et al., 2020)	11
Figure 2. 3: AM process used in the aerospace industry (Williams et al., 2020)	11
Figure 2. 4: Illustration of Laser Powder Bed Fusion Process (Newton, 2020)	12
Figure 2. 5: Classification of Process Parameter for Selective Laser Melting (Kim et al., 2018)	14
Figure 2. 6: Scan strategies for Meander (A), Stripe (B), Chessboard (C) and Total Fill (D)(O'Regan, 2019).....	15
Figure 2. 7: Honeycomb-like macro texture illustrating globally bumpy and locally smooth surface (Zuo and Jones, 2005).....	17
Figure 2. 8: Textured Test Sample (Armillotta, 2006).....	18
Figure 2. 9: Illustration of Roughness, Waviness and Surface Profile (Sahay and Ghosh, 2018)	20
Figure 2. 10: Visual representation of a single surface obtained by optical profilometry (Diaz, 2019).....	21

Figure 2. 11: Two visually distinct theoretical surface (a) Dominated by surface peaks and (b) Dominated by surface troughs with the same Ra value(BS 1134, 2010). ...	22
Figure 2. 12: Surface Finish Classification review (Sibanda et al., 2019).....	29
Figure 4. 1: Illustration of contour scan tracks (blue circles) and infill scan tracks (orange circles)	46
Figure 4. 2: Schematic of the generic formula for theoretical peak width.	47
Figure 4. 3: Illustration of infill scan track for Case 1 (Single Laser Track).....	48
Figure 4. 4: Schematic of Case 1 feature width (X-Z plane).....	49
Figure 4. 5: Illustration of theoretical feature width for Case 2 (Double Laser Track).....	50
Figure 4. 6: Schematic of Case 2 feature width (X-Z plane).....	51
Figure 4. 7: Illustration of the theoretical feature width for Case 3 (Contouring and Infill)	52
Figure 4. 8: Schematic of the theoretical feature width for Case 3 (Contouring and Infill Laser Track)	52
Figure 4. 9: Schematic of SLM system showing hatch spacing, laser power, scan speed and layer thickness (Yap et al., 2015).	55
Figure 4. 10: CAD Design for Sample 1 with section view showing design feature widths 0.3 (Case 1), 0.47 (Case 2), 0.66 (Case 3).	57
Figure 4. 11: Pre-manufacture of AlSi7Mg showing build positions for samples 1-6 on the build platform.....	58

Figure 4. 12: Plan view of sample measurement positions P1, P2 and P3 corresponding to feature height 0.10, 0.20 and 0.30mm.	59
Figure 4. 13: Procedure for characterising feature widths on Sensomap Software showing 3D view (A), plan view (B) and extracted profile (C).....	60
Figure 4. 14: Average measured width and standard deviations for Sample 1.	61
Figure 4. 15: Build layer comparing Left- and Right-hand laser track for Case 2 (A, B) to Case 1 (C, D)	67
Figure 4. 16: Plot of MPE and standard deviations for samples 1-6. Where C1, C2, C3 represent Case 1, Case2, Case 3.	70
Figure 4. 17: Plot of MPE for Samples 1-6 tuned to all the experimental data. Where C1, C2, C3 represent Case 1, Case2, Case	80
Figure 4. 18: Plot of Prediction Error for Samples 1-6 tuned to sample 1 data. Where C1, C2, C3 represent Case 1, Case2, Case 3.	85
Figure 4. 19: Pre-manufacture simulation of SS316L showing build positions for samples 1-6 on the build platform.	88
Figure 4. 20: Graphical representation of average measured width and standard deviations for Sample 1 (1 Front).	89
Figure 4. 21: Graphical representation of average measured width and standard deviations for Sample 2.....	90
Figure 4. 22: Graphical representation of average measured width and standard deviations for Sample 3.....	90
Figure 4. 23: Graphical representation of average measured width and standard deviations for Sample 4.....	91

Figure 4. 24: Graphical representation of average measured width and standard deviations for Sample 5.....	91
Figure 4. 25: Graphical representation of average measured width and standard deviations for Sample 6.....	92
Figure 4. 26: Plot of MPE for original model of Samples 1-6. Where C1, C2, C3 represent Case 1, Case2, Case 3.	105
Figure 4. 27: Plot of MPE for optimised model of Samples 1-6 (PWM laser). Where C1, C2, C3 represent Case 1, Case2, Case 3.	106
Figure 5. 1: Examples of textures which are applicable for aircraft interiors (Adobe, 2020).....	117
Figure 5. 2: Image showing Hf and Lf parameters (adapted from (Armillotta, 2006)	120
Figure 5. 3: Melt-pool schematic showing relationship between melt pool width (W) and Melt-pool Depth (D) (Tang et al., 2017).....	122
Figure 5. 4: CAD Front view showing inner circle with radius 1.35mm (2.7mm diameter)	124
Figure 5. 5: Modified Siemens star with a total of 12 spacing (orange) and 12 spokes (grey).....	124
Figure 5. 6: CAD Isometric view of modified Siemens Star with thickness of 4mm and external radius of 8mm.....	125
Figure 5. 7: Modified Siemens' star showing gap angle of 15 degrees (A) and minimum width section (B).....	126

Figure 5. 8: Modified Siemens' star showing variation in build layer height from 25µm (1) to 300µm (12)	127
Figure 5. 9: Set up for sample measurement with Talysurf contact profiler.	129
Figure 5. 10: Balling effect in feature spacings.....	132
Figure 5. 11: Comparison between measured (red) and design feature (dotted blue) for 0.2mm spacing and 25µm feature height.	134
Figure 5. 12: Comparison between measured (red) and design feature (dotted blue) for 0.2mm spacing and 100µm feature height.	134
Figure 5. 13: Comparison between measured (green) and design feature (dotted blue) for 0.4mm spacing and 150µm feature height.	135
Figure 5. 14: Comparison between measured (green) and design feature (dotted blue) for 0.5mm spacing and 50µm feature height.	135
Figure 5. 15: Comparison between measured (red) and design feature (dotted blue) for 0.5mm spacing and 125µm feature height.	135
Figure 5. 16: Comparison between measured (green) and design feature (dotted blue) for 0.5mm spacing and 150µm feature height.	136
Figure 5. 17: Circular extracted profile for 0.35mm spacing and 25-300µm feature height, 3D view for 0.35mm spacing.	138
Figure 6. 1: 50x45x5mm (LxWxD) sample with designed texture	144
Figure 6. 2: Three texture sizes $T < \min$, T_{\min} $T > \min$	145
Figure 6. 3: Build Tray showing sample pairs with variation in texture size.	147

Figure 6. 4: Level of understanding of LPBF from 24 individual assessors.	151
Figure 6. 5: Experimental set up impression (A); Pleasant adjective / Tactile assessment (B); Tactile Assessment Question (C).	153
Figure 6. 6: LPBF textured surfaces ($T > \min$). As Built: (A) Photograph, (B) Optical Surface Profile (Sensomap). Bead Blasted: (C) Photograph, (D) Optical Surface profile (Sensomap).....	158
Figure 6. 7: LPBF textured surfaces ($T = \min$). As Built: (A) Photograph, (B) Optical Surface Profile (Sensomap). Bead Blasted: (C) Photograph, (D) Optical Surface profile (Sensomap).....	159
Figure 6. 8: LPBF textured surfaces ($T < \min$). As Built: (A) Photograph, (B) Optical Surface Profile (Sensomap). Bead Blasted: (C) Photograph, (D) Optical Surface profile (Sensomap).....	159
Figure 6. 9: LPBF surfaces (Plain). As Built: (A) Photograph, (B) Optical Surface Profile (Sensomap). Bead Blasted: (C) Photograph, (D) Optical Surface profile (Sensomap).	160
Figure 6. 10: Variation in post-processing (same design per set).	161
Figure 6. 11: Variation in presence/absence of texture, textured verses plain (as-built, different design).	163
Figure 6. 12: Photographs of As Built (red) and Bead blasted Sample (green) illustrating the difference surface homogeneity and lightness.	164
Figure 6. 13: Variation in presence/absence of texture, textured verses plain (bead blasted, different design).	165

List of Tables

Table 2. 1: Summary of Relevant Research in AM texture applications.....	26
Table 2. 2: Overview of post processing suitability for AM components.....	30
Table 4. 1: SLM280 machine parameters and AlSi10Mg	44
Table 4. 2: Comparison between Promoppatum et al., (2017): C 1, Metelkova et al (2018): C 2 using the parameters in Table 4. 1	45
Table 4. 3: Chemical composition of AlSi7Mg (MSE Supplies LLC, 2022).....	54
Table 4. 4: Input parameters for the manufacture of samples 1-6 in AlSi7Mg material.	56
Table 4. 5: Percentage Difference in Measured width with Sample 1 as reference (Sample 1- Sample 2).	62
Table 4. 6: Percentage Difference in Measured width with Sample 3 as reference (Sample 3- Sample 4).	63
Table 4. 7: Percentage Difference in Measured width with Sample 5 as reference (Sample 5- Sample 6)	64
Table 4. 8: Mean Percentage Errors (MPE) and standard deviations from the mean. MPEs in red, orange, and green indicate the maximum MPE for each Case.....	68
Table 4. 9: Difference in MPE for Case 1, 2 and 3 features (Sample 1- Sample 2) ..	71
Table 4. 10: Difference in Mean Prediction Error (PE) for Case 1, 2 and 3 features (Sample 3- Sample4)	72

Table 4. 11: Difference in Mean Prediction Error (PE) for Case 1, 2 and 3 features (Sample 5- Sample 6)	72
Table 4. 12: Results samples 1-6 showing the Mean Percentage Error (MPE) and standard deviations.	77
Table 4. 13: Summary of Process parameters and coefficients from tuned model ..	79
Table 4. 14: MPE and standard deviation comparisons between “all data” and sample 1 optimisation	81
Table 4. 15: Summary of Process parameters and coefficients from tuned model to data from sample 1.....	84
Table 4. 16: Chemical composition of SS316L (thyssenkrupp Materials (UK) Ltd, 2022)	86
Table 4. 17: Input parameters for the manufacture of samples 1-6 in SS316Lmaterial.	87
Table 4. 18: Percentage Difference in Measured width for Case 1, 2 and 3 features with Sample 1 as reference (Sample 1- Sample 2).	93
Table 4. 19: Percentage Difference in Measured width for Case 1, 2 and 3 features with Sample 3 as reference (Sample 3- Sample 4).	94
Table 4. 20: Percentage Difference in Measured width for Case 1, 2 and 3 features with Sample 5 as reference (Sample 5- Sample 6).	94
Table 4. 21: Mean percentage errors (MPE) and standard deviations (SD) for the original verses optimised model based on Continuous Laser.	97
Table 4. 22: Mean percentage errors (MPE) and standard deviations (SD) for the original verses optimised model.	101

Table 4. 23: Summary of Process parameters and coefficients from tuned model to all data from samples 1-6.....	104
Table 4. 24: Summary of Process parameters and coefficients from tuned model to sample 1 data.....	108
Table 4. 25: Comparison between average percentage error using all sample data to sample 1 data.....	108
Table 4. 26: Summary of coefficients from L-BFG optimisation algorithm.....	114
Table 5. 1: Predicted melt-pool width to depth ratio for steady state moving point heat source for five samples (Adapted from Mirkoohi et al, 2019). 122	
Table 5. 2: Parameters of Siemens star	125
Table 5. 3: Chemical composition of AlSi10Mg powder (Renishaw PLC, 2015)	128
Table 5. 4: Machine Build Parameters and Thermo physical properties of AlSi10Mg	128
<i>Table 5. 5: Sum of squares for combination of layer height ranging from 25-300μm and design spacing ranging from 0.2 to 1.4mm</i>	<i>133</i>
Table 5. 6: Sum of squares for combination of layer height ranging from 25- 125 μ m and design spacing ranging from 0.25 -0.35mm	137
Table 6. 1: Summary of Baseline Design Parameters where Hf refers to the feature spacing and Lf refers to the feature height.....	146
Table 6. 2: Build power and speed for AM250 for Stainless Steel SS316L processing.	147

Table 6. 3: Chemical Composition of SS316L. (Renishaw, 2001).....	148
Table 6. 4: Sample set for "attractive" adjective with variation in post processing .	155
Table 6. 5: Sample set for "attractive" adjective with presence/absence of texture (As Built).....	155
Table 6. 6: : Sample set for "attractive" adjective with presence/absence of texture (bead blasted).	156
Table 6. 7: Sample set for "pleasant" adjective with variation in postprocessing ...	157
Table 6. 8: Sample set for "preference" adjective with variation in Texture Size....	157

List of Abbreviations

AM	Additive Manufacturing
ASME	American Society of Mechanical Engineers
ASTM	American Society of Testing and Materials
CAD	Computer Aided Design
CAM	Computer Aided Design
CL	Continuous Laser
CMP	Chemo-Mechanical Polishing
CNC	Computer Numerical Control
CW	Continuous Wave
DfAM	Design for Additive Manufacturing
EBM	Electron Beam Melting
EDM	Electrical Discharge Machining
FDM	Fused Deposition Modelling
FE	Finite Element
FEA	Finite Element Analysis
FV	Focus Variation
ISO	International Organisation for Standardization
L-BFGS	Limited-Broyden Fletcher Goldfarb Shanno
LMD	Laser Metal Deposition
LPBF	Laser Powder Bed Fusion
MDF	Medium Density Fibreboard
MPE	Mean Percentage Error
PE	Percentage Error
PWM	Pulse Width Modulation

QFD	Quality Function Deployment
RQ	Research Question
RUM	Rotary Ultrasonic Machining
SD	Standard Deviation
SEM	Scanning Electron Microscopy
SLA	Stereolithography
SLM	Selective Laser Melting
SS	Stainless Steel
ST	Surface Texturing
STD	Standard Deviation
TEM	Tunneling Electron Microscopy
TRL	Technology Readiness Level
UNSM	Ultrasonic Nanocrystal Surface Modification
VED	Volumetric Energy Density
XCT	X-ray Computed Tomography

1 Introduction

1.1 Motivation

This PhD research was sponsored by Safran Seats GB, a leading aerospace company with particular focus on weight reduction and environmentally friendly processes for aircraft interior application. Aerospace component design and manufacture predominantly relies on well-established traditional manufacturing techniques for reliability, functionality, process repeatability and certification (Eres *et al.*, 2014). The nature of these techniques, however, often presents limitations in the geometric complexity which can be achieved in component designs, and therefore increases the need for part assemblies and restricts weight optimisation (Tato *et al.*, 2020).

At the same time, ongoing advancements in Additive Manufacturing (AM), for metal parts, have created a shift in its application from prototyping to the manufacture of fully functional components. In light of this, AM has the potential to complement, or even rival, traditional subtractive and formative processes (Diaz, 2019) in aerospace applications. The increased geometric freedom and part integration possible with AM technologies creates opportunities to reduce part count, optimise material use and minimise the weight of components, but barriers remain for its full integration in the production of “high spec” components such as in the aerospace industry.

A major challenge with Metal Additive Manufacturing is the relatively high per-part cost of production, when compared with traditional manufacturing techniques, which generally can be more easily scaled up for high volume production. However, by identifying the best use cases of AM (such as low volume, or customised products), and fully considering all costs associated with traditional manufacturing techniques, AM can become competitive. For example, assemblies can be redesigned as a single part, hence reducing part count, which increases the cost effectiveness of the process.

Factors such as low build quality, inconsistencies in part build as well as surface and internal defects are just some of the other reasons why AM parts struggle to gain potential industrial use. This is particularly true in the aerospace sector, which applies very strict quality standards. (Buchanan and Gardner, 2019) struggle to gain potential industrial use. This is particularly true in the aerospace sector, which applies very strict quality standards. (Buchanan and Gardner, 2019).

One opportunity for AM adoption, however, is in aircraft interiors. While the nature of AM processes makes aerospace approval highly complex, far less stringent requirements are applied to non-structural interior components. With penalties for overweight interior components currently around €1500/kg, optimisation of the package weight is highly important. AM can therefore be considered as a means of reducing the weight of interior component designs and gives opportunities for assembly time optimisation by consolidating parts. AM also allows greater opportunities for part customization, which is beneficial in an industry where customers often require bespoke designs in low volumes.

Unlike many structural components, some interior components are visible to the customer, so different requirements must be given careful consideration. The surface roughness of an AM part, for example, is generally far greater than that of a conventionally manufactured part. It is often characterised by scan lines, “stair casing effect” (Figure 1. 1) and surface defects (e.g. porosity, partially melted powders) resulting from variations in the melt pools and fusion process (Newton, 2020). Thus, in addition to uncertainties in mechanical performance, these phenomena can make the AM process on its own unsuitable to produce components that require specific aesthetic qualities or textures.

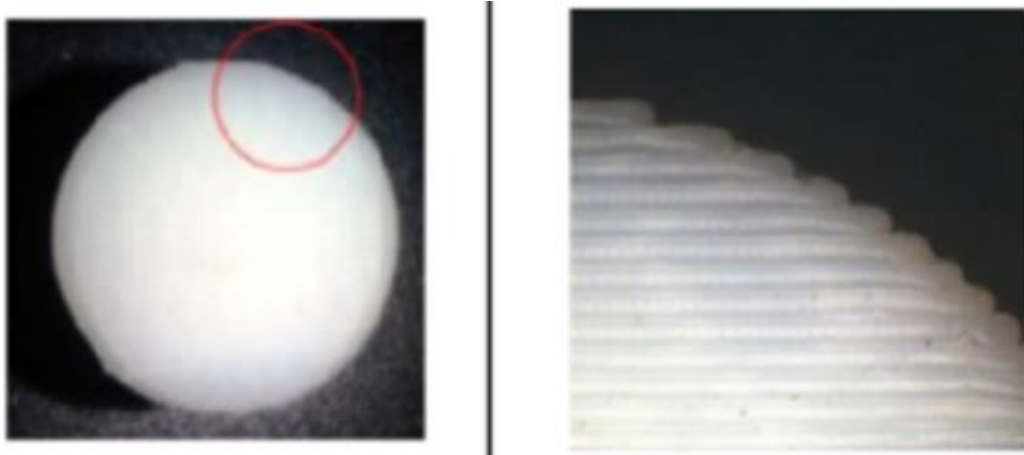


Figure 1. 1: Stair casing effect on AM spherical part (Shi, 2021)

Surface textures (macro) are intentionally designed textures for aesthetic or functional purposes while the general surface texture refers to the small-scale features on the outside of a part, unique to each manufacturing process. Using AM, bespoke surface macro textures can be designed and printed in one go, potentially improving the aesthetic characteristics of the AM surface texture.

1.2 Main Opportunities for LPBF in Aerospace (Aircraft Interiors).

AM allows part design to be geometrically optimised, enabling designers to reap the benefits of topology optimisation, reducing the component weight without reducing the part functionality. Figure 1. 2 shows examples of LPBF for unique designs such as an aesthetic geometric study (a), antenna bracket (b), titanium aircraft seat buckle(c), which were all optimised to make use of the high levels of geometric complexity enabled by metal AM. This is highly beneficial for aerospace industry as the advantage of weight reduction pays off significantly in terms of reduced fuel usage during aircraft operations, thus lowering both costs of fuel and emissions of greenhouse gases (Ngo *et al.*, 2018).

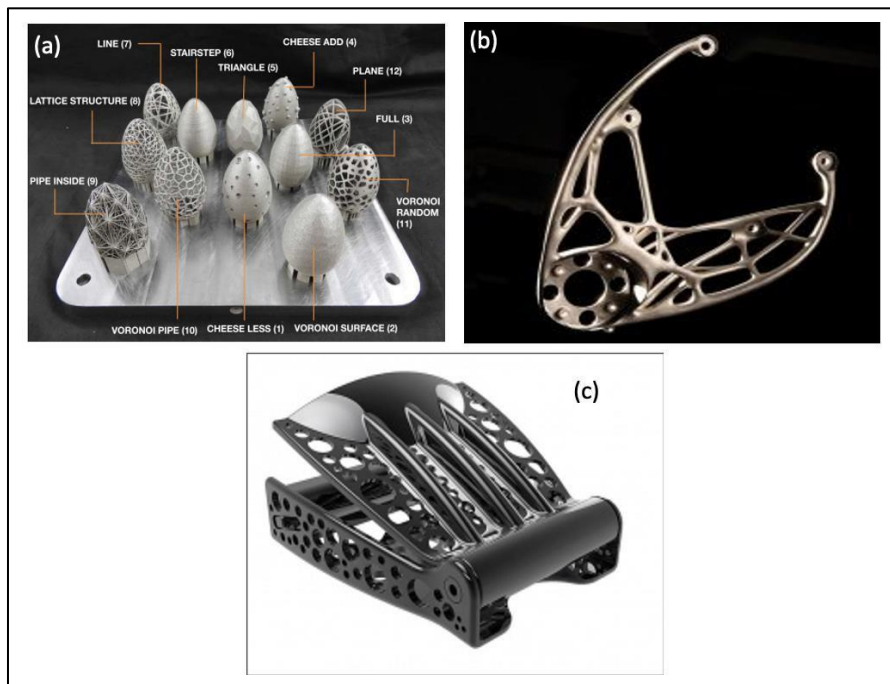


Figure 1. 2: Aesthetic Geometric Study of dimension 60mm height and 40mm diameter (Galimberti et al., 2015) (a); Structural aerospace bracket (Thales Group, 2019) (b); Titanium aircraft seat buckle (Crucible Design, 2021) (c).

From the perspective of the interior of an aircraft, the additional aesthetic appeal that surface geometrical optimization can provide opens up the possibility of creating unique decorative cabin designs. However, as the section 1.1 makes clear, there are still surface quality issues that need to be resolved in LPBF in order to better understand the achievable surface qualities and, ultimately, to encourage their

integration in various industrial applications, such as the production of visible aircraft interior components.

As a result of the flexible nature of LPBF, unique textures can be designed and printing as part of the LPBF build process rather than post processing after printing. This direct texturing approach paves the way for low cost manufacture of bespoke designs compared to techniques such as diamond milling, laser machining or photo etching which come at an additional cost (Armillotta, 2006). Also, there may be added benefit from the surface texturing effect of disguising the inherent irregularities on the surface of LPBF parts. This could potentially provide further time and cost savings from post processing surface finish techniques.

1.3 General Challenges of LPBF in Aerospace (Aircraft Interiors)

The new benefits of metal AM technologies also presents new challenges with regards to the development of design rules to assist designers with how to design parts for the capability of the technology as well as methods for improving the as- built surface quality. In literature, there have been significant efforts to develop new Design for Additive Manufacturing (DfAM) approaches for concept and evaluation phases of design, particularly with regards to achieving desired mechanical properties such as fatigue, stiffness and friction (Galimberti *et al.*, 2016), however DfAM with regards to surface aesthetics have been minimal. The number of publications archived in the Scopus database searched in the title, abstract and keywords, shows a clear trend of increasing interest in AM research when searching the keywords” metal additive manufacturing’ or ‘powder bed fusion’ and ‘design for additive manufacturing (DfAM). However, only around 1% of the results are returned when including the search term “aesthetics”, compared to 25% when including the search term “mechanical properties”. This research trend is illustrated in Figure 1. 3.

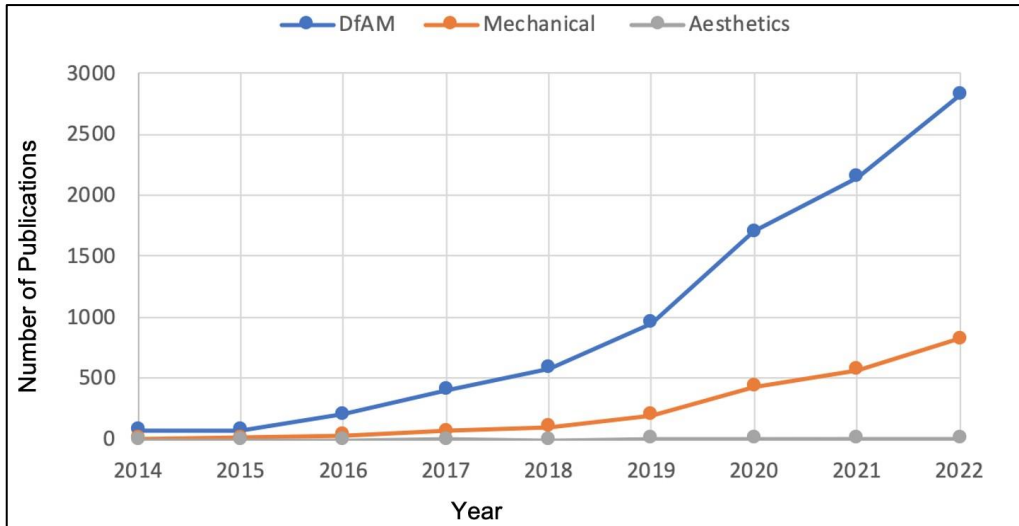


Figure 1. 3: Scopus Database search of publications in metal AM showing trends in aesthetics, mechanical and Design for Additive Manufacturing (DfAM). (Generated by Author)

As highlighted in Figure 1. 3, issues related to surface aesthetics and surface quality, particularly how to tackle it from a DfAM perspective, remains to be solved in LPBF to better understand the achievable surface qualities and therefore to ultimately promote its integration in various industrial applications, such as to produce visible macro textured aircraft interiors components where the surface finish is paramount to part acceptance.

The next section will outline the Aim and Research Questions (RQs) for the thesis.

1.4 Research Aim and Questions

The possibility of direct macro surface texturing can improve the competitiveness of metal AM for visible aircraft interior parts due to the added benefit of design customisation and lower cost compared to post processing macro surface texturing. However, current design rules and DfAM techniques do not address direct macro surface texturing and how to aid engineers to assess the suitability and aesthetic benefit of textures for manufacturing.

Therefore, the aim of this thesis is to develop method(s) to assist with the prediction of the feasibility and aesthetic characterisation of direct textures manufactured by Laser Powder Bed Fusion (LPBF).

The following research questions have been identified:

RQ1: What are the current gaps in literature particularly in the improvement and characterisation of the LPBF surface?

RQ2: What approach(es) can be used to quickly assess whether a design for macro surface texture is feasible for LPBF fabrication?

RQ3: How can engineers assess whether the macro surface texture design will be aesthetically pleasing and deliver the required functionality in a safe manner?

The RQs will be refined after the literature review to identify specific objectives for this research.

1.5 Thesis Structure

The remaining sections of the thesis are structured as follows:

Chapter 2: Literature Review. This chapter is a review of approaches to enhance the as-built surface of metal AM parts and the current state of the art for direct and post process surface optimisation techniques. The gaps in surface finish and characterisation techniques are reviewed.

Chapter 3: Experimental Methods. This chapter outlines the methods selected to address the RQs and Objectives.

Chapter 4: Parametric Approach for Small feature Width Prediction. This chapter presents an analytical approach for the prediction of small feature width produced in the X-Y plane by the LPBF process, which can be used for the design and production of direct macro surface textures.

Chapter 5: Assessment of Minimum Spacing between featured produced by LPBF. In this Chapter, an approach is proposed for determining the minimum measurable spacing between two adjacent features for a specified design feature depth.

Chapter 6: Aesthetic Evaluation of Textured LPBF Surfaces: This chapter aims to assess whether an aesthetically pleasing texture can be fabricated with a combination of the smallest feasible feature sizes (width and spacing) which a machine and material combination can produce to generate a texture.

Chapter 7: Conclusion and Future work: This chapter provides the conclusion to this research including research contribution to knowledge. It also outlines the recommendations and suggestions for future work.

2 Literature review

2.1 Chapter Summary

The intention of this Chapter is to review the state of the art in metal Additive Manufacturing (AM) by first providing a general overview of AM which discusses the inception of AM and the evolution of the technology till date. This is followed by an overview of the Laser Powder Bed Fusion Technique (LPBF) considering the differences in laser types, process parameters and scanning techniques. Next, a review of AM surface texture definition, measurement, characterisation, and post processing is presented in the context of aesthetic aircraft interior applications.

2.2 General Overview of Additive Manufacturing (AM)

Additive Manufacturing (AM) is a layer wise technology which allows components with very high geometric complexity to be manufactured (Atzeni and Salmi, 2012). As such, AM enables the realisation of parts which will be challenging or impossible to manufacture by traditional subtractive or formative processes; parts are built in a layer-by-layer fashion, enabling high complexity geometries and part integration with traditionally multi-component assemblies manufactured as a single part. In the early days of AM, the technique was used for manufacturing moulds for topographical maps (Leach *et al.*, 2019). This is evidenced by the patent filed by Blather, (1892) on the cut and stack technique where wax sheets were used to develop laminated moulds (Figure 2.1a). By the 1970s, a similar approach was used to create 3d shapes with the main difference being that, the cross section of the part was cut out of metallic sheets, joined together and finally machined for a smooth outer surface finish (DiMatteo, 1974; Das *et al.*, 2016).

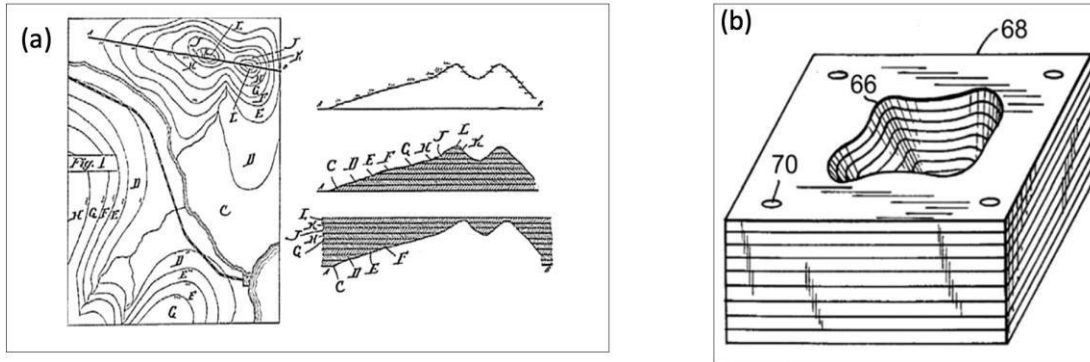


Figure 2. 1: Cut and Stack approach for creating a wzx tool set by Blather (Blather, 1892) (a); Layered metal parts using Cut and Stack approach (Das et al., 2016).

In addition to the cut and stack approach, a layered approach was developed in 1925 by Baker, (1925) where beads of metal were layered on top of each other to create a 3D geometry. This process is referred to as weld overlay (Baker, 1925). A similar modern-day AM technique will be the Wire and Arc Additive Manufacturing. Following the 1990s, 3D printing in metal has evolved from sintering, indirect sintering with polymer binders and then laser melting. A comprehensive record of the evolution of the metal additive manufacturing process has been outlined by (Das et al., 2016) on metallic materials for 3D printing.

2.2.1 Categories of Metal AM

There are seven types of metal AM technologies classification. The classification shown in Figure 2.2 is based on the heat source, which is used for joining the feedstock to create the part and the type of feedstock, which refers to the material used for building the part.

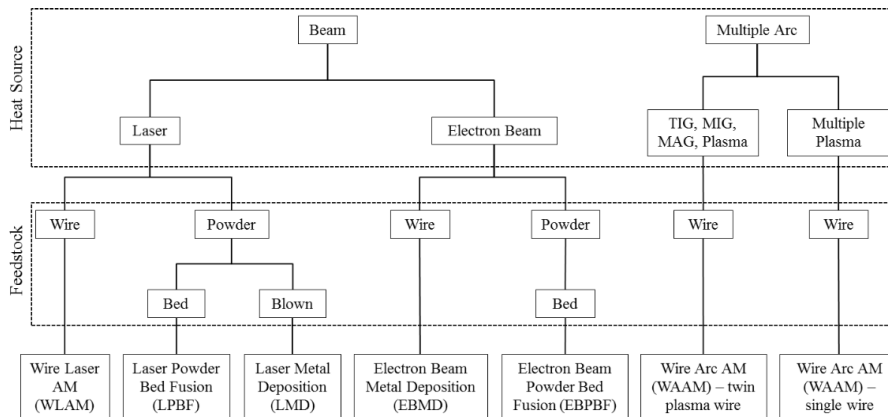


Figure 2. 2: Classification of Metal AM process (Williams et al., 2020)

There are two main types of feedstock, powder or wire. In the case of powder feedstock, the powder can either be on a platform or bed as in Laser Powder Bed Fusion (LPBF) or Electron Beam Melting (EBM) or blown as in the case of Laser Metal Deposition LMD). Compared to other metal AM techniques, Laser Powder Bed Fusion (LPBF) offers better surface quality, dimensional accuracy and part complexity as illustrated in Figure 2.3. Also, LPBF technology is more accessible to Safran Seats GB, hence the most desired process for this research. Therefore, LPBF will be the focus of this thesis.

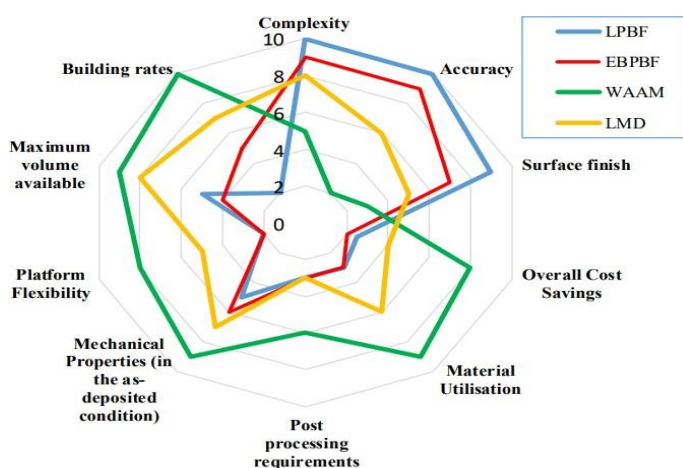


Figure 2. 3: AM process used in the aerospace industry (Williams et al., 2020)

2.2.2 Overview of LPBF Manufacturing Process

A typical LPBF manufacturing process is shown in Figure 2.4. Generally, an inert atmosphere is generated in the build chamber to prevent oxidation during the melting process followed by heating of the chamber to minimize thermal gradient during the melting process. The powder feeding system deposits a thin layer of powder on the build platform which is distributed by the powder spreading device to ensure that the powder layer meets the pre-defined build thickness. The laser melts the powder by selectively scanning the exposed powder layer according to the CAD data. Once the melted part solidifies, it sticks to the previously melted layer underneath. The build platform moves down and the powder distribution, melting and solidification process repeats until the part fabrication is complete (Newton, 2020).

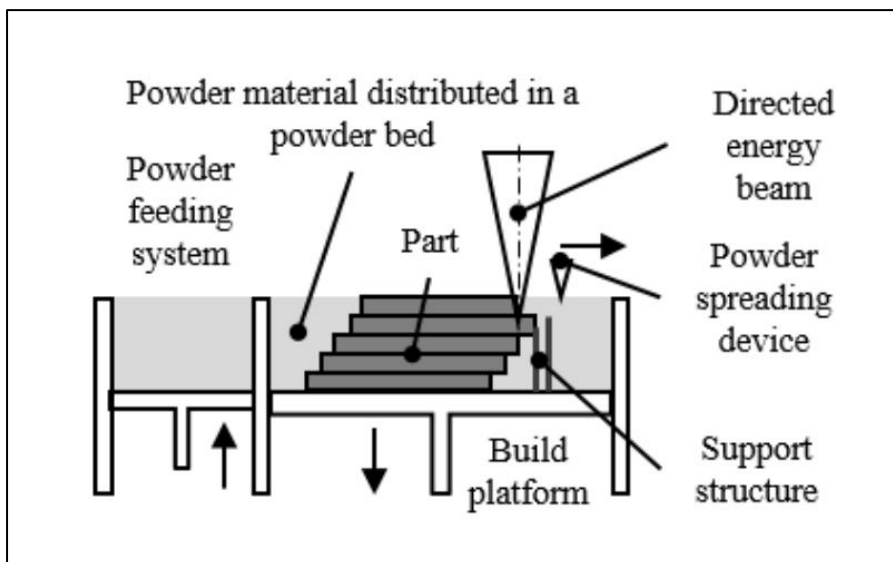


Figure 2. 4: Illustration of Laser Powder Bed Fusion Process (Newton, 2020)

2.2.2.1 Laser Types and Build Process Parameters

There are two main types of lasers used in the LPBF process namely the Continuous Wave (CW) laser and the Pulse Width Modulated (PWM) laser. The CW laser discharges consistent energy to the powder whereas the PWM laser emits energy for a precise time interval (Kim *et al.*, 2018). Due to the variations in process parameters and subsequently the melting mechanisms of the PWM and CW lasers, the melt-pool characteristics differ. From Figure 2.5, there are sixteen different process parameters, which can potentially influence the melt-pool characteristics however, the four main parameters, which have been extensively researched on, are:

- Laser Power, P (watts)
- Scanning Speed, v (mm/s)
- Hatch Spacing, h (mm)
- Powder layer thickness, t (μm)

These parameters combine to give the Volumetric Energy Density (VED) which is a measure of the amount of energy stored in a unit volume of powder. The VED affects the melt pool in the following ways:

- Optimum VED results in high relative density of parts (close to 100%).
- Low VED can lead to pore formation from lack of fusion resulting in low relative density of parts. This could impact the mechanical properties such as fatigue and stiffness.
- Excessive VED leads to porosity and keyhole formation hence low relative density of parts (Kempen *et al.*, 2014).

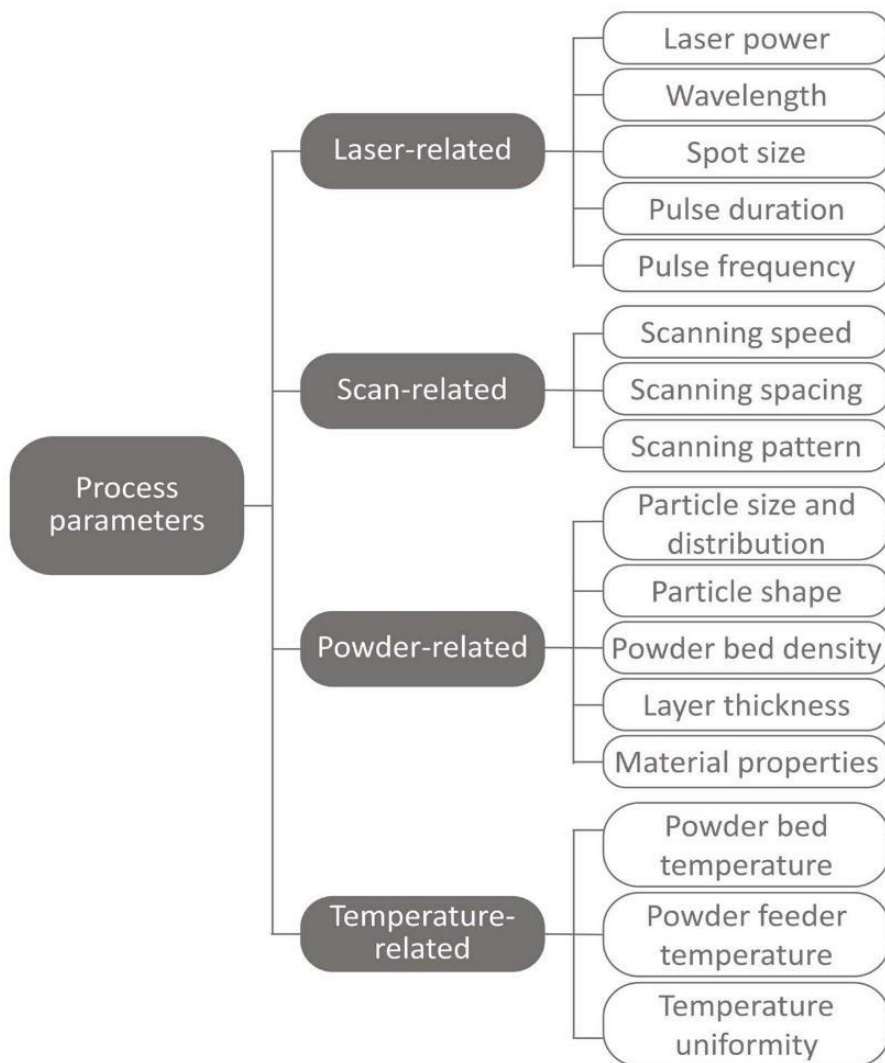


Figure 2. 5: Classification of Process Parameter for Selective Laser Melting (Kim et al., 2018)

2.2.2.2 Scanning Strategies

There are four main types of laser scanning strategies namely stripe, chessboard, meander and total fill (O'Regan, 2019). This is shown in Figure 2.6. The stripe scan or chess board strategies are usually ideal because they allow heat to be distributed evenly across the powder bed hence preventing the occurrence of heat concentrations within the build (O'Regan, 2019).

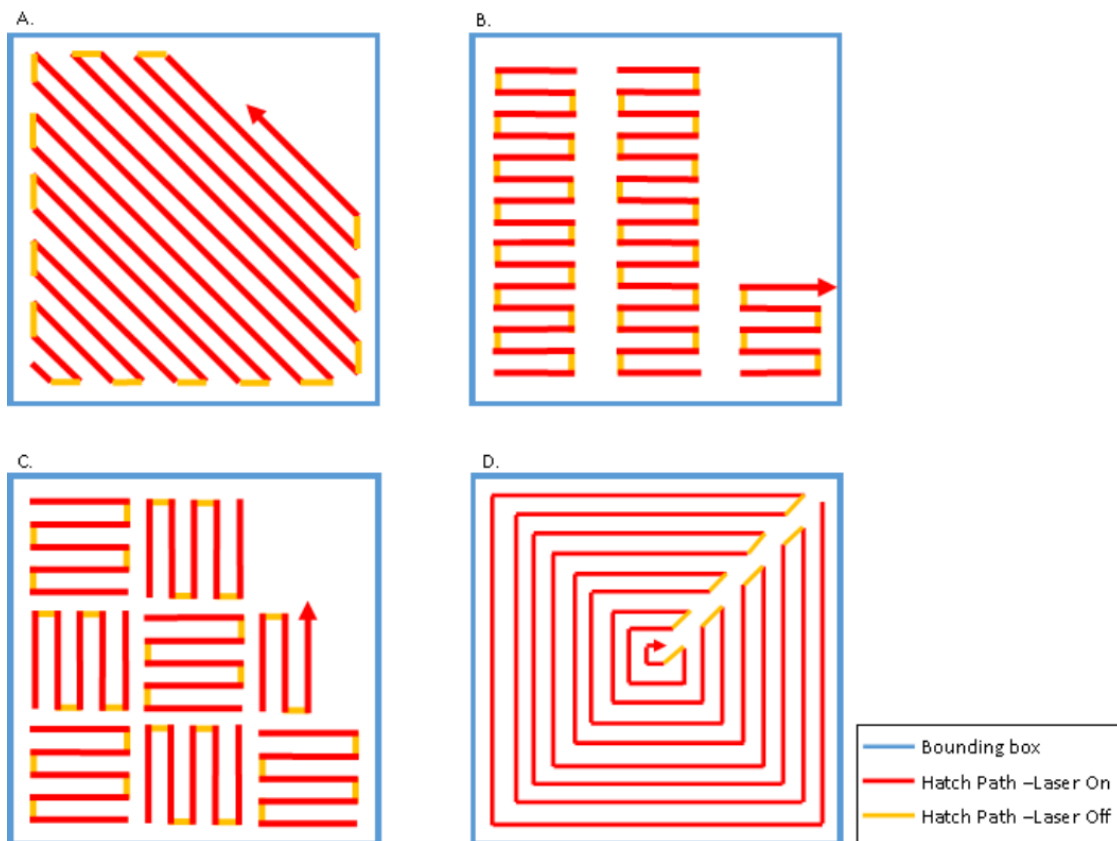


Figure 2. 6: Scan strategies for Meander (A), Stripe (B), Chessboard (C) and Total Fill (D)(O'Regan, 2019).

2.3 Introduction to Surface Textures and Metrology

In the context of this thesis, and in order to differentiate from macro surface features, plain surface texture refers to the features and inconsistencies on a surface which show divergence from the contemplated geometry as defined in ASME B46.1-2009 (Diaz, 2019). When examining LPBF surface textures, vertical surfaces are often characterised by partially melted powder and staircasing effect, with down skin surfaces typically having higher roughness than up skin surfaces (Mohammadi and Asgari., 2018) . Surfaces which are in contact with support structures often have remains of the support attached to them which also influences the surface texture. In addition, top surfaces are often characterised by the existence of surface irregularities and partially bonded particles (Strano *et al.*, 2013).

Even though different LPBF machines generate variations in inherent surface textures, many of their features are common. These features are the main identifiers of LPBF parts, and are driven by parameters such as component orientation, contour parameters (Abele and Kniepkamp, 2015; Chen *et al.*, 2018) layer thickness (Doubenskaia *et al.*, 2016; Nguyen *et al.*, 2018), laser power (Brown *et al.*, 2018; Mohammadi and Asgari, 2018) and scan speed (Abele and Kniepkamp, 2015).

2.3.1 Macro Surface Textures

Macro surface textures, in the context of this thesis, refer to random or periodic surface patterns which are intentionally designed for aesthetic, functional or visual effects (Zuo and Jones, 2005).

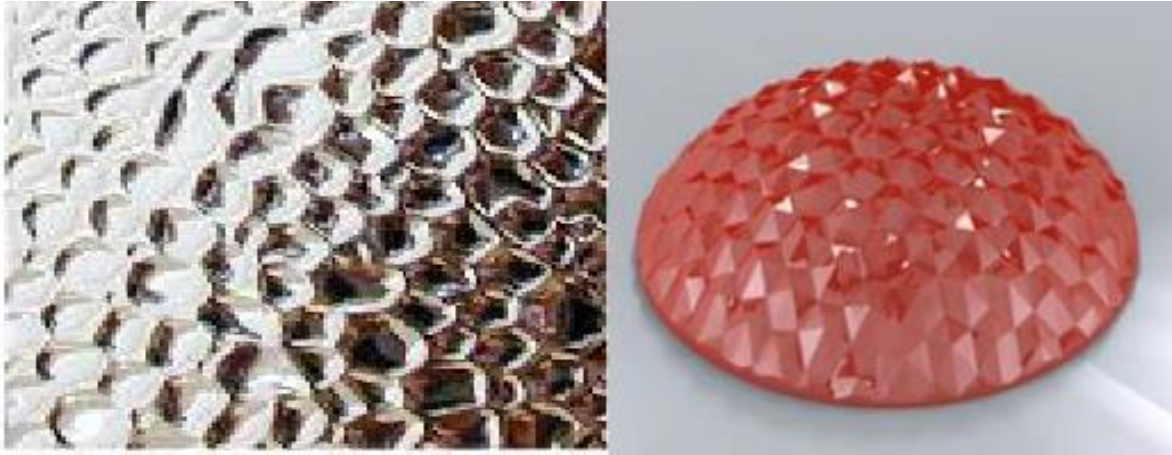


Figure 2. 7: Honeycomb-like macro texture illustrating globally bumpy and locally smooth surface (Zuo and Jones, 2005).

Figure 2.7 shows an example of macro surface textures which can be purposely manufactured for functional or aesthetic reasons. Unlike traditionally manufactured parts, the cost of printing a macro surface texture or a plain surface texture is the same (Slant 3D, 2019), hence one approach at texturing can be considered in AM processes by using their inherent plain surface texture as purposed built macro textures. This can be difficult to control because the final surface state of an AM part will be strongly dependent on various factors such as processing parameters, powder size, build orientation and build position (Chen *et al.*, 2018; Mohammadian, Turenne and Brailovski, 2018). Another approach could be to purposely design macro textures, independent of the plain surface texture.

A good example of a previous attempt at direct texturing was an experimental study on the surface quality of macro textured FDM prototypes (Armillotta, 2006). The aim of the exercise was to test the feasibility of macro/direct texturing as well as achievable resolutions of direct textured surfaces (Armillotta, 2006). In this experiment, a benchmark part was designed with a regular surface pattern but with different aspect ratios (the ratio of height to width) and different build orientations (shown in Figure 2.8). Feature sizes ranged from 1 to 4mm and height from 0.5 to 2mm were produced both perpendicularly and parallel to the build direction. The printed parts were inspected visually and with an optical microscope. It was concluded that for surfaces parallel to the build direction, feature sizes must be a minimum of 1mm to minimise

the staircasing effect. Also, for perpendicular surfaces, aspect ratio should not be less than 0.3- 0.4 and features should be spaced at least 1mm apart for the proper visualisation of valleys (Armillotta, 2006). Thus, this study shows that, despite typical AM imperfections such as features created by the staircasing effect, purposely built macro textures could be considered when designing a component.

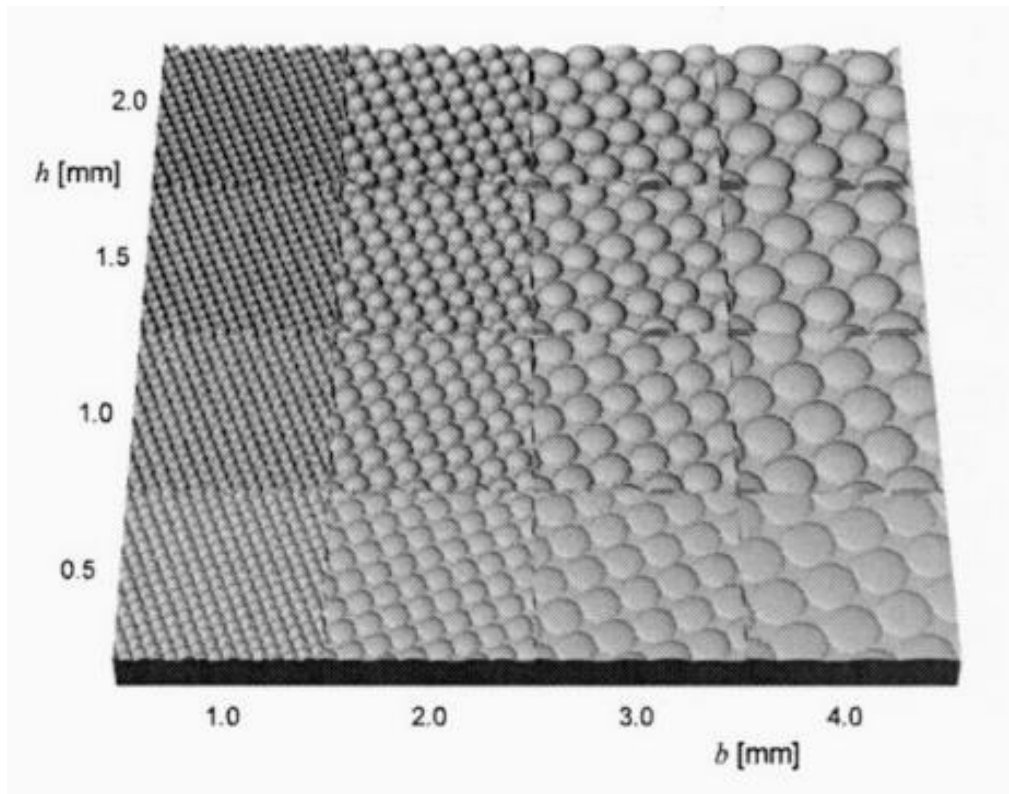


Figure 2. 8: Textured Test Sample (Armillotta, 2006)

2.3.2 Metrology of Surface Textures

By gathering data on the surface, a better understanding of the surface morphology can be gained. Typically, the complete surface information, known as the surface topography or the plain surface texture (as defined in ISO25178-3, 2012) can be obtained by the application of a number of operations to the primary surface extracted during the metrology process (Townsend *et al.*, 2016).

Surface metrology is a collective term used to describe the process of measurement and characterisation of a surface (Townsend, 2018). Engineering surfaces can be considered as a complex combination of features at different scales. These different geometrical components can be categorised depending on their scale, and in combination, can be used to describe the nature of the surface.

2.3.3 Surface Measurement

The simplest methods of surface profile acquisition involve subjective visual and or tactile comparison between “standard” surfaces, and the surface of interest. In some situations, this may be sufficient, however in many engineering applications more in-depth analysis of a surface is required and so the surface must be measured (Newton *et al.*, 2018). There are two broad classes of measurement systems available, namely contact, and non-contact profilers. Contact profilers make use of a stylus to acquire the 2D profile of the surface whereas noncontact methods commonly use optical height sensing to capture the 3D profile of a surface (Townsend *et al.*, 2016; Newton *et al.*, 2018). In some instances, X-ray Computed Tomography (XCT), Scanning Electron Microscopy (SEM) (Zhihao *et al.*, 2018) or Tunneling Electron Microscopy (TEM) (Senin, Thompson and Leach, 2017) can be used for non-contact surface metrology, however, it is important to assess the advantages and disadvantages of each technique in order to determine the suitability for the surface under analysis.

2.3.4 Surface Characterisation

The surface measurement process is usually followed by the extraction of meaningful quantitative information from the measured data. This process is known as surface characterisation (Townsend, 2018). In order to characterise the measured data, surface filtration is often applied to differentiate the surface measurement into its components of form, waviness and roughness (Lou *et al.*, 2019). This is illustrated in Figure 2.9: Illustration of Roughness, Waviness and Surface Profile (Sahay and Ghosh, 2018)

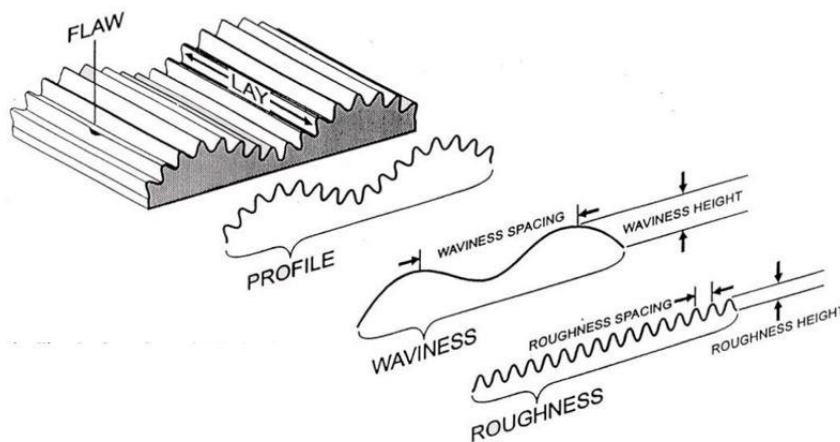


Figure 2. 9: Illustration of Roughness, Waviness and Surface Profile (Sahay and Ghosh, 2018)

Current studies about the use of filtering techniques for AM surfaces are often based on standard methods for characterising surfaces made by traditional manufacturing techniques. Firstly, a filter is applied to the surface in order to separate the waviness and roughness components after which the cut off wavelength can be applied, followed by the process of calculating surface parameters (Lou *et al.*, 2019). ISO-4288, (1998) indicates the procedure for sampling and evaluation length selection based on periodic or non-periodic profile estimation. Visual inspections, graphical comparisons, or roughness comparison specimens are often used for the estimation of surface roughness for conventional surfaces as a guide to determine the sampling wavelength which corresponds to the cut off wavelength.

Also, as shown in the example given in Figure 2.10, there is a considerable difference in the visual representation of the surface with a cut-off of 80 μm compared to a cut-off of 250 μm applied to the same surface.

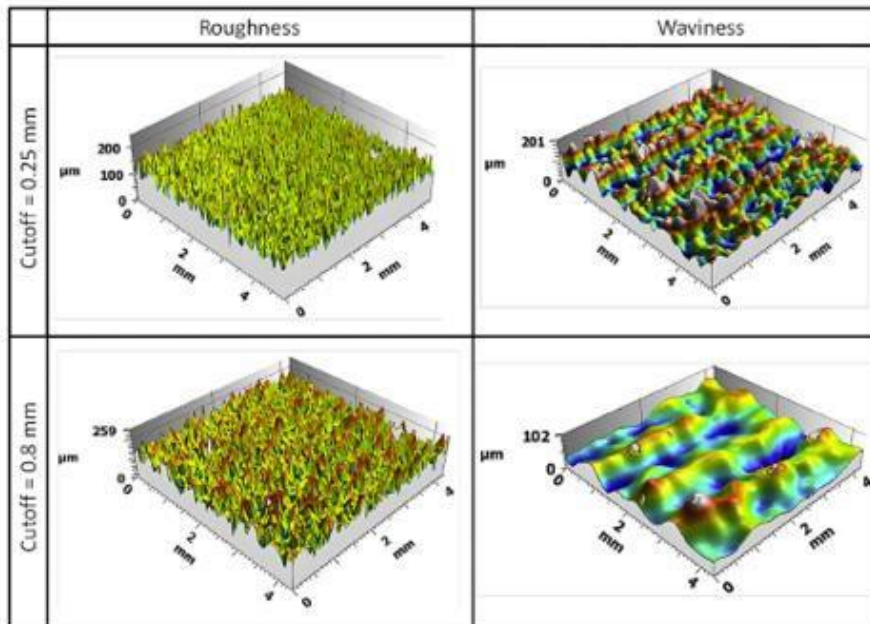


Figure 2. 10: Visual representation of a single surface obtained by optical

Changing the cut off wavelength also changes the measured surface roughness and reconstructed waviness images obtained from optical profilometry. For example, for the same surface, adjustments to the filtering applied can cause S_a/R_a parameters to vary significantly. Figure 2.11 shows that two surfaces with the same R_a can behave very differently due to the specifics of the morphology of the structuring element.

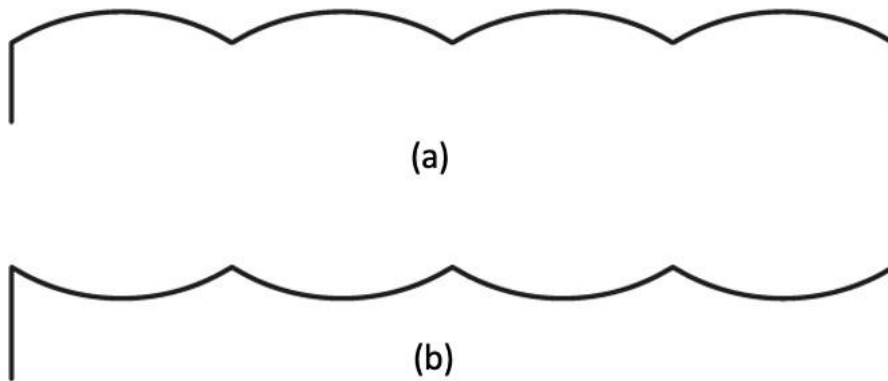


Figure 2. 11: Two visually distinct theoretical surface (a) Dominated by surface peaks and (b) Dominated by surface troughs with the same Ra value(BS 1134, 2010).

To allow purposely built macro textures to be incorporated into component design standard approaches enabling the formal characterisation of aesthetic qualities of AM surface textures are required.

2.3.5 Surface Characterisation in Relation to Surface Appearance

Surface characterisation in relation to perceived appearance is a complex challenge as surface appearance is influenced by factors such as texture, colour, and transparency (Eriksson, Rosen and Bergman, 2018) and attempts to quantify an objects appearance with a single measurement technique often prove inadequate. Biondani *et al.*, (2019) investigated the characterisation of surface gloss for mould manufacturing and noted that the use of Sa or Sq for defining the quality of a surface is insufficient. The authors noted that affective engineering, which is a method of correlating objective surface information with subjective human surface perception, can be useful for defining surface appearance. Out of the affective engineering techniques, Kansei technique has been stated to provide a suitable framework for characterising surface appearance (Eriksson, Rosen and Bergman, 2018).

This technique can be described as a customer-focused method for developing new products. The fundamental principle is that, when a project advances from the conception stage to the production stage of the product development process, it is important to consider the client's sentiments throughout the project lifecycle. Kansei is considered superior to techniques such as Quality Function Deployment, QFD, and Kano technique. These techniques (QFD and Kano) are excellent at handling psychological sensation, but struggle to convert subjective feelings into design specifications—that is, qualities of the actual product that affect how it is perceived (Eriksson, Rosen and Bergman, 2018).

Hence for visual characterisation, benchmarking was achieved with the aid of SEM (Scanning Electron Microscope) images to accurately identify parameters with the closest link to visual surface quality. In most cases, multiple measurement technologies and techniques are often used to correlate the aspects of surface appearance to provide an adequate description of surface appearance.

2.3.6 Techniques for Assessing Surface Appearance.

There have been reports of the use of Kansei technique to characterise surface appearance of materials ranging from wood to polymer FDM surfaces. Ramanantoandro, et al., (2014) assessed the correlation between 3D roughness parameters and surface visuo-tactile perception. Maritime pinewood and Medium-Density Fibreboard (MDF) samples were sanded with a range of sandpaper sizes from P60 –P320. The authors found that the valley material component, Sr2 had the highest correlation to tactile roughness for MDF samples and suggest using a 300µm cut off wavelength of the roughness profile when analysing tactile perception of the surfaces. Also, Li et al., (2017), to determine the perceivable difference between FDM, SLA and Polyjet samples, from a visuo-tactile perspective, found that maximum peak-to-valley height (Rz) had higher correlation with tactile and visual perception and kurtosis of the topography height distribution (Rku) had the highest correlation with hedonic sensation.

Similarly, Ramanakoto et al., (2019) found that for planed and sanded surfaces of beach and oak, tactile sensation can be correlated with S_{sk} , V_{mc} and S_k , and state that the waviness profile is more closely linked to human perception.

Hence, it is apparent that the material type and subsequently, the material texture has an impact on the perceived appearance of the part. Objective surface characterisation together with the Kansei technique will still yield useful indication of which surface parameters are closely linked to the visuo- tactile characteristics of LPBF surface however, till date, efforts to apply affective engineering on macro textured LPBF surfaces remain minimal.

The lack of agreement in literature, or guidance through standards, for the proper assessment of surfaces, both from an objective characterisation and subjective affective engineering restricts the progression of AM metrology through both the current reliance on a researcher's discretion when processing collected surface data, and an inability to directly compare results from different studies (compounded by lack of full reporting over the data processing applied).

It is hoped that, in lieu of standards being developed for the metrology of AM surfaces, there is a widespread shift for researchers to include more complete information regarding the measurement and analysis of surfaces, and for greater understanding of how the different parameters available influence different mechanical, physical and aesthetical properties of a surface. For example, it is difficult to ascertain trends for what cut offs / nesting indexes are used. It appears that most publications do not state the values used, or indeed any other processing applied. Diaz (2019) makes the strong point that without this information any parameters provided are all but meaningless it is still unclear what the standard cut off wavelength should be for non- periodic, granular, and non-uniform surfaces manufactured by AM. Clearly, R_a/S_a values alone do not describe a surface and from the mathematical definition it is clear R_a/S_a gives no information about the distribution of peaks/valleys, if there is a bias in the proportion of peaks to valleys, or the average shape of elements.

Also, research on the objective quantification of surface quality in relation to aesthetics has led to some determination of which surface parameters correspond to the tactile or visual response of human perception. However, to date, there has been no consensus on the most appropriate characterisation parameters, filters, and cut-off wavelengths to allow these comparisons to be reliably made. Certainly, attempting to measure surface appearance is a very challenging task since the human influence and psychological response is subjective, hence it is important to understand which aspects of surface appearance can be measured now and which aspects are relevant, will require further research work.

In the context of aircraft interior components, the development of appropriate surface quality assessment techniques would help further explore the potential of LPBF, to establish if inherent plain surface texture can be disguised by direct manufacture of macro textures purposely built for their aesthetic qualities.

2.4 Techniques for Surface Finish Improvement of AM Components.

Surface defects such as balling, surface pits and non-periodic nature of AM surfaces are prevalent on the as-built surface of LPBF parts and for most applications, post processing surface finish techniques are typically applied to improve the surface quality (Diaz, 2019; Ye *et al.*, 2021). In the review of “state-of-the-art of surface finishing processes and related ISO/ASTM standards for metal additive manufactured components (Lee *et al.*, 2020), the authors focused on the impact of surface finish, high porosity and tensile residual stresses on the fatigue performance of metal AM parts. Post processing methods such as surface finish techniques, heat treatment and hot isostatic pressing, were discussed in relation to improvements in the fatigue performance of metal AM parts. In this literature review, in process surface techniques, in specifically direct texturing applications, will be discussed in 2.4.1 whereas post processing techniques will be reviewed in 2.4.2.

2.4.1 Direct Texturing Techniques

In literature, textures have been applied for a wide range of applications including tribology, food quality and preference. The main references are summarised in Table 2.1

Table 2. 1: Summary of Relevant Research in AM texture applications

Reference	Application	Summary
Hong <i>et al.</i> , (2017)	Tribology	<p>Hong <i>et al.</i> investigated the effect of biomimicry textures on the tribological properties of 3D printed polymer surface.</p> <p>The authors noted that the friction properties of the surface could be significantly altered through texturing.</p> <p>This was dependent on the type of texture used, with the circular concave feature having the best friction and wear performance.</p>

Reference	Application	Summary
Guo <i>et al.</i> , (2022)	Tribology	In Guo et al (2022), surface texturing (ST) could be used as a method of improving wear resistance of GCr15 bearing steel under certain conditions.
Mekhiel et al.,(2021)	Hydrophobicity	Mekhiel et al (2021) used textures to control the wettability behaviour of stainless steel SLM samples.
Kovacı and Seçer, (2020)	Tribology	Kovacı and Seçer (2020) used a combination of surface texturing and plasma nitriding to improve the tribological behaviour of 316L stainless steel SLM parts. Eight different ranges of textures were experimented on. The authors concluded that the friction and wear properties improved due to the addition of textures.
van Rompay <i>et al.</i> ,(2017)	Food Quality and preference	van Rompay et al (2017) found that the perceived quality of beverages was improved by designing and printing regular patterns on the drinking cups.
Armillotta, (2019)	Generic	Armillotta (2019), investigated the feasibility of adding textures to triangle meshes of AM models with the focus on improving the software processing time and texture fabrication quality. The author investigated various constraints and found that processing constraints were less onerous compared with computational constraints. The proposed method improves the uniformity and consistency of textures compared to existing approaches and can support future systematic studies on the detail resolution of AM processes.

2.4.2 Post Processing Techniques

A systematic literature review was conducted which resulted in the classification of post processing techniques as mechanical, electro-chemical or thermal, derived from the nature of the energy used to create the polishing effect. Figure 2.12 shows the surface finish technique classification based on the review. Significant research and development is still on-going to improve traditional techniques to suite the complexity afforded by AM. Interestingly, some hybrid processes such as a combination of chemical and mechanical polishing, Chemo-mechanical polishing (CMP), have been developed recently in order to take advantage of the benefit of two or more techniques (Jain, 2008). An evaluation of finishing techniques, considering their suitability for application on AM components, is shown in Table 2. 2.

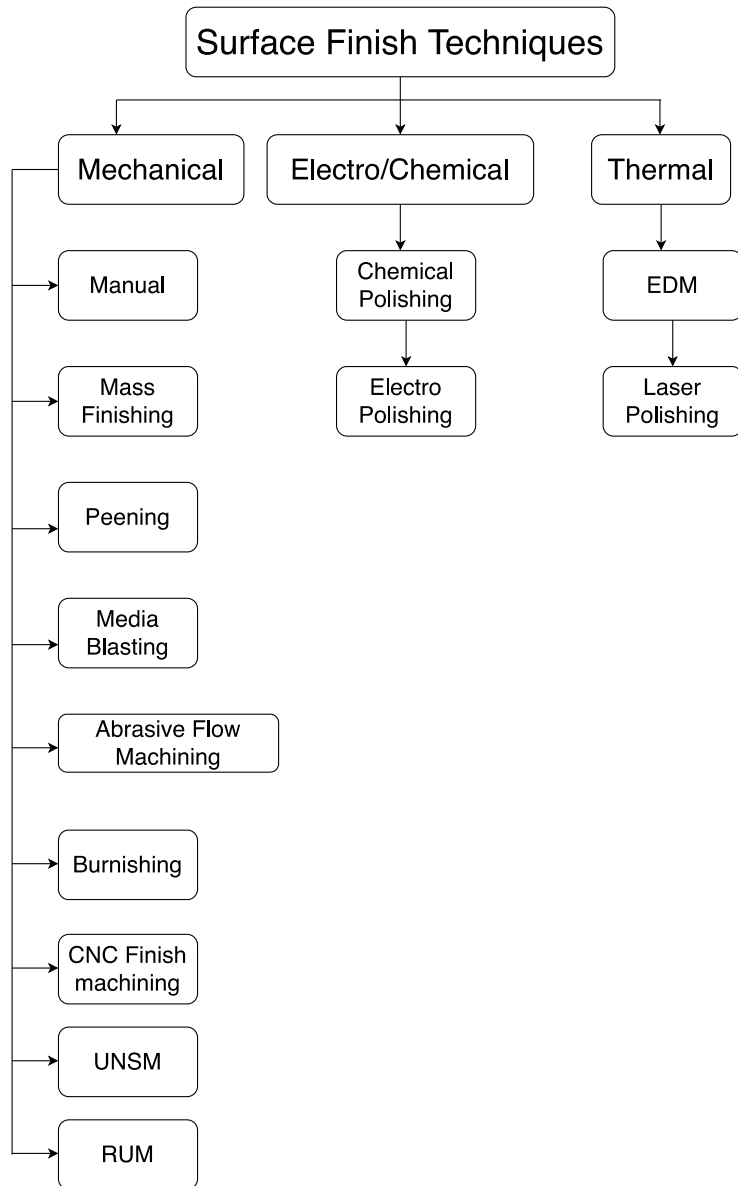


Figure 2. 12: Surface Finish Classification review (Sibanda et al., 2019)

Table 2. 2: Overview of post processing suitability for AM components

Material Removal Mechanism	References	Advantage(s)	Disadvantage(s)
Mechanical			
Manual: Hand Sanding, grinding, or polishing	(Bordatchev, Hafiz and Remus Tutunea-Fatan, no date; Niknam and Songméné, 2013; Morton <i>et al.</i> , 2011; Jamal and Morgan, 2017)	High flexibility for range of geometric complexities. Relatively low cost.	Uncovering of sub-surface features
Mass finishing: Processing parts by relative motion between abrasive and part surface.	(Kaynak and Kitay, 2019)(Gillespie, 2007; Morton <i>et al.</i> , 2011; Mediratta, Ahluwalia and Yeo, 2016; Ahluwalia, Mediratta and Yeo, 2017; Vijayaraghavan and Castagne, 2018; Zhang <i>et al.</i> , 2018; Kaynak and Kitay, 2019) (Boschetto <i>et al.</i> , 2020)	Low cost Minimizes subsurface porosity. Allows for process automation.	Lengthy processing times (up to 48h). Media wastage.

Material Removal Mechanism	References	Advantage(s)	Disadvantage(s)
Mechanical			
Peening: Use of laser or spherical shots to improve surface roughness by impact.	(Hackel <i>et al.</i> , 2018; Luo <i>et al.</i> , 2019; Wang <i>et al.</i> , 2019), (Newton, Senin and Leach, 2018)	Improves surface fatigue and hardness	Potential damage to thin parts. Shot craters resulting from shape and size of shots.
Media blasting: Work piece surface targeted with intense media stream.	(Bagehorn, Wehr and Maier, 2017; Tan, Yeo and Ong, 2017; Mohammadian, Turenne and Brailovski, 2018; Zhang <i>et al.</i> , 2019)(Tan, Yeo and Ong, 2017; Hackel <i>et al.</i> , 2018)	Applicable to wide variety of materials Wide range of blasting media availability	Low material removal rate. Part complexity restrictions e.g., Blind holes
Abrasive Flow machining: Internal surfaces targeted with high pressure (up to 220bar), media laden fluid	(Jain, 2008; Tan, Yeo and Ong, 2017), (Kim and Kim, 2004)(Rhoades, 1991),	Suitable for internal channels	May cause damage to thin-walled structures. Internal channel contamination by abrasives

Material Removal Mechanism	References	Advantage(s)	Disadvantage(s)
Mechanical			
Burnishing: Surface plastic deformation with hard or smooth roller.	(A. P., 2013; Verma and Mahato, 2013; Jaya Prasad <i>et al.</i> , 2018)	Improves fatigue and stress corrosion resistance of parts	Unsuitable for small and fragile parts due to high force applied during process
CNC finish machining: Usage of cutting tool to remove exterior of part surface.	(Kaynak and Kitay, 2019; Zhang <i>et al.</i> , 2019)	Generates good surface finish for low complexity parts. Relatively inexpensive and well understood process	Not applicable to highly complex parts
UNSM: Use of tungsten carbide tip to strike surface combined with burnishing effect under static loading.	(Chi Ma, Mohsen Taheri Andani, Haifeng Qin <i>et al.</i> , 2017; Kattoura <i>et al.</i> , 2018)	Minimizes near surface porosity. Improved corrosion, fatigue, and wear resistance of parts	Unsuitable for fragile part
RUM: Combination of traditional milling with ultrasonic machining.	(Ahmed <i>et al.</i> , 2017)	Cost effective for machining high strength materials like titanium	High machining time. Low process maturity for industrial purpose

Material Removal Mechanism	References	Advantage(s)	Disadvantage(s)
Chemical			
Chemical polishing: Usage of chemical solution to dissolve rough surface.	(Mohammadian, Turenne and Brailovski, 2018; Tyagi <i>et al.</i> , 2018)	Suitable for complex geometries. Suitable for freeform and porous structures.	Potential for low dimensional accuracy due to material removal (~80 μm for parts of high roughness).
Electro polishing: Material removal by anodic dissolution of surface layer.	(Rokosz and Hryniewicz, 2012; Chatterjee, 2015; Rotty <i>et al.</i> , 2016; Yang <i>et al.</i> , 2017; Han and Fang, 2019)	Cost effective method of surface improvement for fragile parts. Improves part corrosion resistance.	Often utilizes harsh chemicals as electrolyte. Setup cost for large components. High voltage supply requirement.

Material Removal Mechanism	References	Advantage(s)	Disadvantage(s)
Thermal			
EDM: Discharges from tool aperture is used to heat and melt surface irregularities. (PEDM, MEDM, WEDM)	(Wu <i>et al.</i> , 2005; Gnanavel <i>et al.</i> , 2017) (Boban <i>et al.</i> , 2020)	Applicable to wide range of electrically conductive materials.	Low material removal rate
Laser polishing.	(Temmler, Willenborg and Wissenbach, 2012; Rosa, Mognol and Hascoët, 2015; Bhaduri <i>et al.</i> , 2017; Yung <i>et al.</i> , 2018; Zhihao <i>et al.</i> , 2018; Li <i>et al.</i> , 2019)	Selective polishing of small areas (<0.1mm ²) Surface hardness improvement.	Costly to operate and cost increases with complexity. Weld track appearance on surface.

2.5 Conclusion of Literature Review

This Chapter presents a review of LPBF surfaces and surface finish techniques based on existing related literature. The adoption of AM components has clear advantages to the aerospace industry; however, certification requirements can limit their implementation at present. Opportunities exist to use AM in less critical interior components, but the poor quality of the as-build surfaces also presents barriers in this area. The research highlights the surface morphology of LPBF parts and the potential difficulty in characterising surfaces qualitatively based solely on current practices, such as using roughness parameters (e.g., influence of filtering method could result in incomparable or even meaningless roughness values).

The current surface finish of LPBF parts prohibits the large-scale adoption of the technology, particular in the aerospace industry. Techniques such as mechanical processes are more traditional and well understood however, there may be limitations in terms of the complexity of parts which can be finished by such techniques. Thus, following a review of current capabilities and practices in LPBF, surface characterisation, direct texturing and surface post processing, research directions are presented which should enable a better understanding and control of surface textures produced by LPBF.

Understanding and improving the aesthetic quality of surfaces made by Metal AM will help accelerate the adoption of the technology for manufacturing visible aircraft interior components, allowing part integration, reduced component weight, and end- user customization by creating bespoke components that can meet various customers' needs, hence enhancing overall satisfaction.

The opportunity to manufacture bespoke textures directly as part of the LPBF build is an interesting prospect however, specific guidelines on texturing DfAM is lacking. Also, improving and characterising the surface appearance or aesthetics of surface produced by LPBF is an ambitious challenge however, significant progress can be made by achieving the following.

- Improvement in the interest and proactiveness of standardisation organisations such as the ASTM in the aspect of affective techniques for surface quality characterisation. Affective engineering techniques such as the Kansei technique have not yet been applied to LPBF surfaces, however, it is likely that such a study will provide clarity on which surface parameters provide a better indication of visual and tactile surface quality.
- The assessment of the perspective of surface appearance using aircraft interior related objects to determine the response of people to “visual” and “tactile” surface quality. Introducing the use of soft metrology will build an understanding of which aspects of surface quality can be characterised.
- To take into consideration the development of new measure(s) which will correlate the subjective data from human assessment to objective surface topographic measurement. These will potentially need to be specific to the specific industry (e.g., aircraft interiors) and may even require specific measures tailored to a particular product or application.
- With respect to LPBF parts and achievable surface features, the determination of feature sizes which can be built, again based on a combination of machine and material specifications.
- The extension of aesthetic evaluation to different texture types and presentation of the results in a meaningful way to designers is fundamental to direct texturing adoption for LPBF surfaces for visible aircraft interior applications.

Since this thesis intends to focus on texturing of LPBF parts, and ultimately the adoption of direct texturing in the aerospace industry, the three main objectives of this thesis to answer the research questions in section 1.4, are as follows:

- The development of a quick assessment for determining the dimensions of surface features that can be manufactured, based on the technology capability (e.g., the machine and material combination)
- Proposal of an approach for determining the minimum measurable spacing between two adjacent features for a specified design feature depth.
- Assessment of whether an aesthetically pleasing texture can be created by combining the smallest feasible feature sizes (width and spacing) that a machine can produce to generate a texture.

3 Experimental Methods

This research explores LPBF for aircraft interior applications with the overarching aim of developing method(s) to assist with the prediction of the feasibility and aesthetic characterisation of direct surface textures manufactured by Laser Powder Bed Fusion (LPBF). The following sections will explain the methodology for achieving the three main objectives of this research.

3.1 Research Objective 1 (Chapter 4)

The first objective of this research is to develop a rapid analytical approach for determining the minimum width of surface features which can be produced by a given machine and material combination, to be validated by experimentation. In order to achieve this objective, a literature review will be conducted on the existing analytical methods for predicting feature width. Preference will be given to methods, which are quicker for predicting feature widths compared to longer prediction times. This may have an impact on the prediction accuracy hence considerations for improving prediction accuracy will be examined. SLM 280 machine and ALSi7Mg material will be used for manufacturing the samples to align with the overall global strategy of Safran LPBF part manufacture. Details are in section 4.2 and 4.3.

3.2 Research Objective 2 (Chapter 5)

The second objective of this research is to propose of an analytical approach for determining the minimum measurable spacing between two adjacent features for a specified design feature depth. Similar to Objective 1, a literature review will be conducted on existing approaches to determine the best method for determining the minimum measurable spacing. This will be validated by experimentation. Details are in section 5.2 and 5.3.

3.3 Research Objective 3 (Chapter 6)

The third objective is the assessment of whether an aesthetically pleasing texture can be created by combining the smallest feasible feature sizes (width and spacing) which a machine can produce to generate a texture. Ultimately, designers will benefit from the knowledge of whether or not the textures produced by LPBF will be aesthetically pleasing. To assess this, the results from Chapter 4 and 5 will be used to produce bespoke textured parts. Experimental methodology from existing literature will be used to determine the best approach for gathering and analyzing feedback from surface assessments based on human interactions. Details are in section 6.3-6.5.

By achieving the set objectives in 3.1, 3.2 and 3.3, the summative knowledge of this thesis can be used to design and manufacture surface textures which are not only within the machine and material capability but also aesthetically pleasing to the customer or consumer.

4 Parametric Approach for Millimeter Scale Feature Width Prediction

4.1 Summary

As discussed in Chapter 2, to facilitate DfAM guidelines in macro surface textures, there is a need for development of a quick assessment approach to determine which surface features can be fabricated, based on the LPBF technology capability (e.g., the machine and material combination). This chapter presents a theoretical parametric model developed for the prediction of millimeter scale feature width produced in the X-Y plane by the LPBF process, which can be used to design and directly produce macro surface texture. The model considers the build parameters of the LPBF process, as well as the material's thermo-physical properties including laser absorptivity, specific heat capacity, density, melting and ambient temperature.

4.2 Introduction

Enabling direct texturing is particularly interesting for aircraft interior applications for two main reasons. Firstly, it would allow bespoke and complex designs to be fabricated with surface textures without additional costly post processing steps.

Secondly, the surface macro features, used for creating the direct texturing effect, have an added benefit of aesthetically disguising the irregularities inherent of the LPBF process (Slant 3D, 2019) such as scan lines or stair casing effect, partially melted powders and surface porosity.

Current improvements in Computer Aided Design (CAD) software have made it easier for design engineers to create three Dimensional (3D) models for manufacturing (Adobe, 2020). In addition, Computer Aided Manufacture (CAM) software are capable of generating the laser path for each layer, which corresponds to the cross section of the sliced model (Liu, Yang and Wang, 2017). Thus, from a design perspective, the textured part can be digitally modelled and visualised on CAD software and from a manufacturing perspective, the laser path can also be generated from CAM. However, due to uncertainties in achievable geometries at sub-millimetre scales, it is challenging

to assess which design of textures are feasible, considering the combined capability of the LPBF machine and the specific material powder.

Hence, the continuous improvements in the capability and resolution of LPBF machines coupled with eager research into novel AM compatible materials have resulted in the need to understand how the technology resolution (machine and material capability) can be assessed quickly in relation to direct texturing, pre-manufacture and without costly trial and error experiments, to evaluate easily if a design intent can be manufactured for a specific machine and material combination. Therefore, to allow the design of textures, which are sensitive to the machine and material combination, it is important to understand how the minimum texture size can be assessed pre-manufacture.

Previous research activities have focused on determining the melt-pool width experimentally or numerically, aimed at predicting and improving the overall dimensional accuracy of LPBF parts (Promoppatum *et al.*, 2017; Tang *et al.*, 2017; Metelkova *et al.*, 2018, Zhang *et al.*, (2018)). Some analytical models have been developed for the prediction of dimensional accuracies of LPBF parts (L. Zhang *et al.*, 2018, 2019; Zhang, Zhang and Zhu, 2021), but in these publications, the melt- pool widths were derived experimentally which can be time consuming and costly. Finite Element Analysis based simulations can also be used for such predictions, but they generally are computationally expensive. Thus, methods for quick estimation at design stages of achievable small feature sizes, based on a specific machine and material combination, are still lacking in current research, particularly with a focus on direct texturing.

Therefore, the focus of this research work will be on the quick assessment of machine and material capability, for direct texturing of LPBF parts. The first step is to take a closer look at the melt- pool geometry. Since the melt-pool geometry is the fundamental building block of every single laser scan, of which characteristics are dependent on machine process parameters and on material properties, the following sections of this chapter provides a review of research efforts on the characterisation of the melt-pool geometry. Next, a new metal AM feature width prediction approach is proposed, and an experimental validation of the model is carried out with a continuous laser. After the initial validation experiment, results showed the need to improve the accuracy of this width prediction approach hence, model optimisation was carried out.

The optimised model was used to tune a Pulsed Width Modulated laser machine after which the optimised coefficients for the machine parameters were used to improve the model prediction accuracy.

4.3 Review of Melt-Pool Width Estimation

To create a single laser scan track, a laser beam selectively melts metallic powder in the scanning direction (y) to create a melt-pool. The laser may either melt the powder by keeping a continuous value of power, as in the case of a continuous wave (CW) laser or by emitting a specific quantity of power for a specific exposure time, referred to as Pulsed Width Modulation (PWM) laser (Kim *et al.*, 2018). For both laser melting mechanisms, the melt-pool characteristics are dependent on the thermo-physical properties of the material and the build parameters of the machine (Metelkova *et al.*, 2018).

Some studies have focussed on determining the melt-pool width generated by the LPBF process. Most authors refer to the Rosenthal equation (4.1), an analytical method which was originally developed for application in fusion welding as a process of predicting melt pool thermal history (Promoppatum *et al.*, 2017). As a result of the similarities between fusion welding and LPBF, authors Promoppatum *et al.*, (2017), Tang, *et al.*, (2017) and Metelkova *et al.*, (2018), have applied the Rosenthal equation to the LPBF process due to its simplicity (in comparison to FEA and experimentation), accuracy and speed in estimating melt-pool characteristics such as melt pool width and shape.

The simplified Rosenthal equation used by Promoppatum *et al.*, (2017) is as shown in equation 4.1.

$$W_{mp} \approx \sqrt{\frac{8}{\pi e} \cdot \frac{\lambda \cdot P}{\rho \cdot C_p \cdot v (T_m - T_o)}} \quad (4.1)$$

Where W_{mp} is melt-pool width(m), λ is absorptivity, P is laser power (W), e is the natural exponent, ρ is the density of the material($kg \cdot m^{-3}$), C_p is specific heat capacity ($J \cdot kg^{-1} \cdot K^{-1}$), v is laser velocity ($m \cdot s^{-1}$), T_m is melting temperature (K), T_o is initial temperature before melting (K).

For the estimation of a melt-pool width in LPBF, using the Rosenthal equation, the following assumptions were made by Promoppatum *et al.* (2017):

- Laser power and scan speed are constant during the melt-pool formation.
- The source of heat is considered as a point source.
- Loss of heat due to radiation and convection from the surface are considered as negligible.
- Negligible convection in liquid melt-pool and negligible loss of heat from radiation and surface convection.
- Purely conductive heat transfer.
- Powder deposition does not significantly affect the size of the melt-pool.
- Exclusion of latent heat due to phase changes.
- Thermo-physical properties of the material are independent of the temperature changes.

Promoppatum *et al.*, (2017) intended to compare the results of melt-pool width estimation for SLM Inconel 718 products from analytical calculation (using the Rosenthal equation), Finite Element Analysis (FE) and experimental results from literature. The authors found that the melt-pool widths from the analytical, FE and experimental results were similar. However, because of keyholing effect, differences

were seen when comparing melt-pools created under conditions of high power. When keyholing occurs, there are changes in the melt-pool shape and reduction of width due to thermal radiation and convection losses. Since the Rosenthal equation does not consider these thermal losses, the analytical width was wider than the experimental width. Hence, for high power, the FE model has higher accuracy.

However, adequate energy inputs lead to a melt pool formation free of keyholing and porosity (e.g., 0.4J/mm or less for Inconel 718 material, Promoppatum et al., 2017).

Promoppatum et al., (2017) demonstrated that the Rosenthal equation was accurate and provided a quick method for estimation of melt-pool width. In this thesis, since the intention is to manufacture samples with adequate energy inputs for each processed material (neither keyholes nor porosity formation), the Rosenthal equation will be applicable for the test conducted.

The Rosenthal equation used by Metelkova et al., (2018) also used the Rosenthal equation, similar to the one used by Promoppatum et al., (2017). The main difference is that Metelkova *et al.*, (2018) simplification of the Rosenthal equation calls for the inclusion of thermal diffusivity, D , which is a method of quantifying heat distribution through an object (Boucher, 2019).

Also, with Metelkova et al., (2018) simplification of the Rosenthal equation, thermal diffusivity needs to be calculated before the melt-pool width can be estimated. This equation (thermal diffusivity variant) is shown in the equation 4.2.

$$W_{mp} \approx \sqrt{\frac{P}{v} \cdot \frac{8 \cdot A \cdot D}{e\pi K(T_m - T_0)}} \quad (4.2)$$

Where D is the thermal diffusivity, (m^2s^{-1}), K is thermal conductivity, (W/mK),

In order to determine whether there is any difference between the results in calculated melt-pool width, W_{mp} for both equations, the following parameters were used in this research based on processing conditions for SLM280 machine and AISi10Mg material

to calculate W_{mp} using both equations. The machine and material combination were selected to align with Safran group AM strategy.

Table 4. 1: SLM280 machine parameters and AISi10Mg

Thermo-Physical Property	Value (AISi10Mg)	Reference(s)
Absorptivity, A, λ	0.32	(Tang et al., 2017)
D, Thermal Diffusivity ($m^2 s^{-1}$)	4.50×10^{-5}	Calculated property, $\frac{K}{\rho \times C_p}$
P, Laser Power (W)	650	(SLM Solutions, 2012)
V, Laser Speed (m/s)	2.1	SLM Solutions
e, Natural Exponent	≈ 2.72	
π	3.14	
K, Thermal Conductivity (W/mK)	110	(Tang et al., 2017)
C_p , Specific heat capacity (J/ kg. K)	915	(Tang et al., 2017)
ρ , Density, (kg/m^3)	2670	Tang et al., 2017)
T_m , Melting temperature (K)	849	Tang et al., 2017)
T_o , Ambient temperature before melting (K)	423.15	SLM Solutions

Table 4. 2: Comparison between Promoppatum et al., (2017): C 1, Metelkova et al (2018): C 2 using the parameters in Table 4. 1

C1 (Promoppatum et al., 2017)	C2 (Metelkova et al 2018)
$W_{mp} = \sqrt{\frac{8}{\pi e} \cdot \frac{\lambda \cdot P}{\rho \cdot C_p \cdot v (T_m - T_o)}}$	$W_{mp} \approx \sqrt{\frac{P}{v} \cdot \frac{8 \cdot A \cdot D}{e \pi K (T_m - T_o)}}$
$\sqrt{\frac{8}{3.14 \times 2.72} \times \frac{0.32 \times 650}{2670 \times 915 \times 2.1(849 - 423.15)}}$	$\sqrt{\frac{650}{2.1} \times \frac{8 \times 0.32 \times 4.50 \times 10^{-5}}{3.14 \times 2.72 \times 110(849 - 423.15)}}$
$W_{mp} = 298.62 \mu\text{m}$	$W_{mp} = 298.62 \mu\text{m}$

Both equations resulted in the same output of melt-pool width of $W_{mp} \approx 298.62 \mu\text{m}$ as shown in Table 4. 2 hence Promoppatum et al., (2017) version of the Rosenthal equation will be adopted for the development of the new theoretical parametric model described in this chapter. This is due to the relative ease of deriving the melt-pool width in comparison to the simplified Rosenthal equation by Metelkova et al (2018).

The next section describes in detail the developed theoretical parametric model, which has been designed for the quick prediction of small feature widths producible in the forming direction (x) for various machine/material combinations.

4.4 New Metal AM Feature Width prediction Model

A Metal AM layer is typically produced using a combination of infill laser scan tracks, to produce the bulk of the component, and of contour laser scan tracks, to obtain optimum surface quality. This is controlled automatically by most CAM software used in Metal AM machines. Therefore, the new parametric model should be able to consider these dual scanning strategies of infill and contouring. However, as the aim of the model is to predict millimeter scale features widths achievable for the creation of surface textures, it is assumed that the infill and contour tracks generated by the CAM software for the designed small features will always be parallel as more complex in fill scanning strategies will only be generated for larger features. This prediction model derives its novelty from the combination of the Rosenthal equation, for predicting melt pool width, with the interaction between two successive melt pools, the hatch spacing.

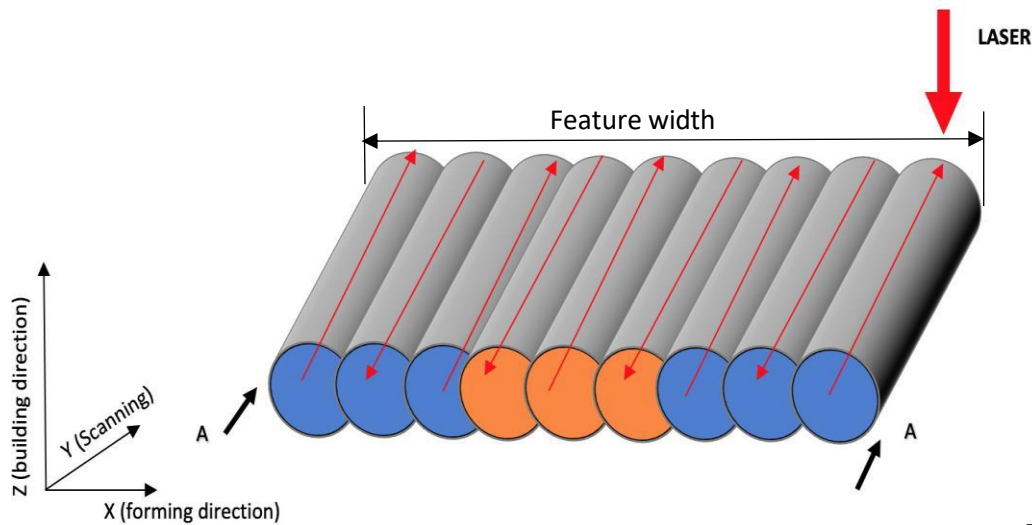


Figure 4. 1: Illustration of contour scan tracks (blue circles) and infill scan tracks (orange circles)

Thus, as an example, the width of a small feature produced in a single layer with three contour and three infill laser scan tracks, perpendicular to the build direction (Z), is shown in Figure 4. 2. To predict the overall feature width in the forming direction (X), the melt-pool width and the hatch spacing between adjacent tracks need to be known.

Figure 4. 2 shows the contour and infill track filling modes for a single layer scan in the X-Z plane.

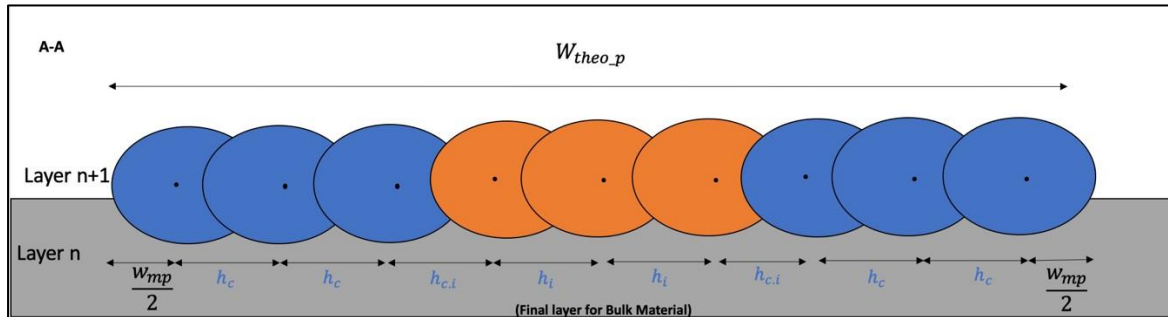


Figure 4. 2: Schematic of the generic formula for theoretical peak width.

Hence, the generic formula for estimating the theoretical peak width for a combination of contour and infill laser scans can be calculated using equation 4.3.

$$w_{theo.p} = \sqrt{\frac{8}{\pi e} \cdot \frac{\lambda \cdot P}{\rho \cdot C_p \cdot v(T_m - T_o)}} + 2(n_c - 1)h_c + 2h_{c,i} + (n_i - 1)h_i \quad (4.3)$$

Where n_c is the number of contour tracks, n_i is the number of infill tracks, h_c is the hatch distance between adjacent contour tracks, h_i is the hatch distance between adjacent infill tracks, $h_{c,i}$ is the hatch distance between adjacent contour and infill tracks and w_{mp} is the melt-pool width that can be calculated based on the material properties and build parameters.

The aim of this chapter is to investigate millimeter scale features used in creating macro textures. The prediction model focusses on parallel scan tracks and after three scan tracks, the CAM slicing software usually alters the scanning strategy from parallel to oblique scan tracks. If the number of scan tracks are increased beyond three laser tracks, the small features may not always be represented by parallel tracks. Since the CAM slicing software was owned and managed by an external supplier, it was decided that only three distinct cases would be investigated in this thesis to validate the

proposed model, namely Single laser scan track as the smallest possible feature discussed in section 4.4.1 (Case 1), Double laser scan track discussed in section 4.4.2 (Case 2) and Contouring with infill scan strategy discussed in section 4.4.3 (Case 3). These tests should be adequate for an initial evaluation of the analytical model while maintaining the parallel scanning strategy.

4.4.1 Single Laser Scan Track

For the single laser scan track scenario (Case 1), a single laser melt track in the scanning direction (Y) represents the feature. This is illustrated in Figure 4. 3 and a schematic is shown in Figure 4. 4.

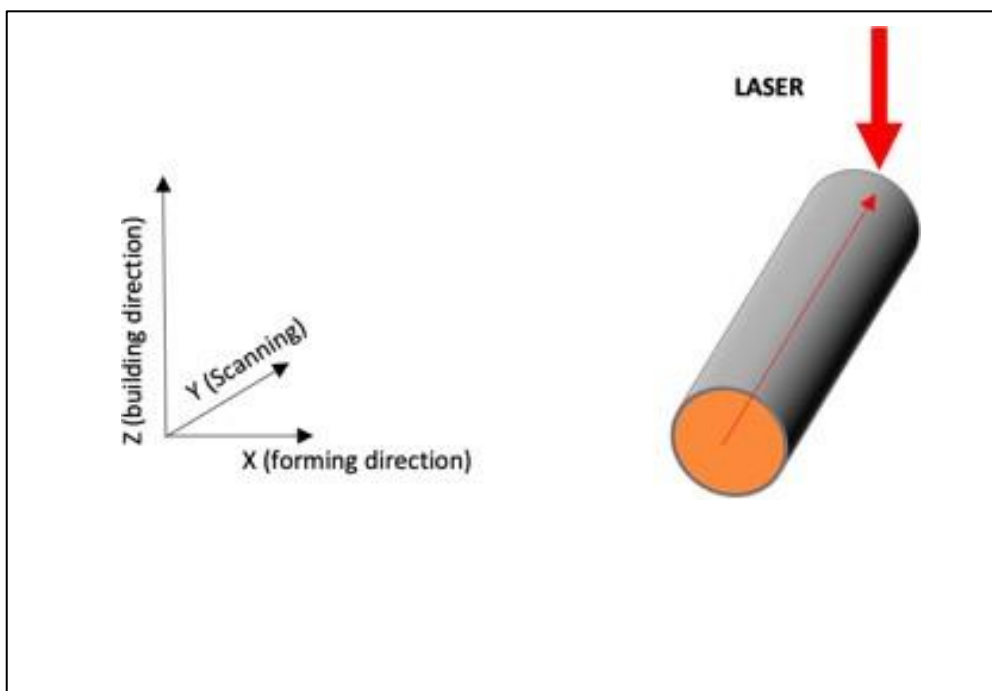


Figure 4. 3: Illustration of infill scan track for Case 1 (Single Laser Track)

Therefore, for Case 1 condition, minimum feature width is equal to the melt-pool width calculated based on the thermo-physical properties of the material and build parameters of the machine. Assuming that the laser parameters is the same as the infill parameters, the $w_{mp} = w_i$, where w_i is the infill melt-pool width.

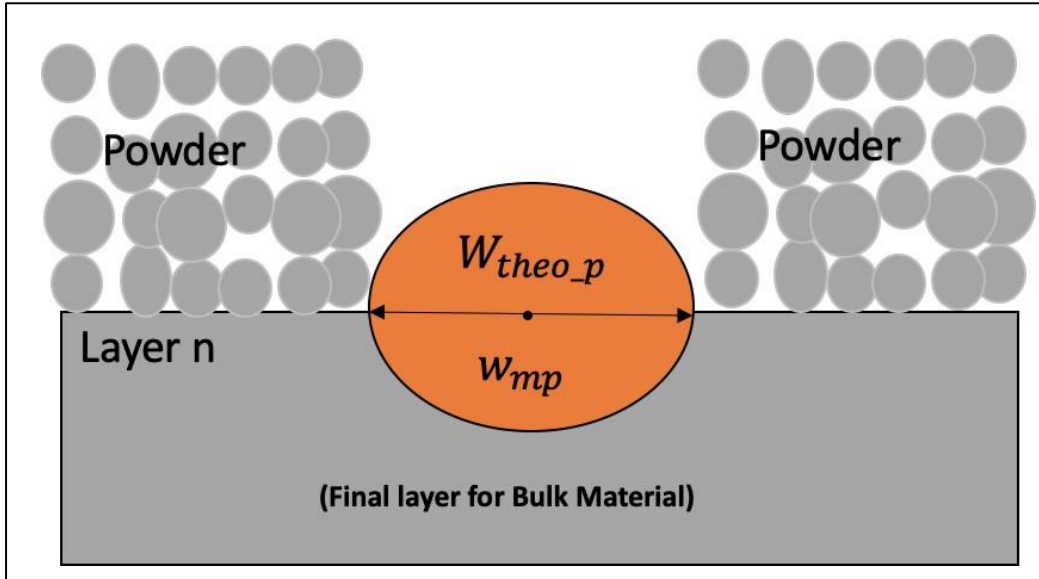


Figure 4. 4: Schematic of Case 1 feature width (X-Z plane)

The number of contours $n_c=0$ and the number of infills, $n_i=1$, hence, by referring to the generic formula, substituting for Case 1, $w_{mp} = w_i$, $n_c=0$, $n_i=1$ into equation 4.3. Therefore, the formula for determining the theoretical peak width for Case 1, single scan track is shown in equation 4.5.

$$w_{theo_p} = (w_i) + 2(0 - 1)0 + 2(0) + (1 - 1)0$$

$$w_{theo_p} = (w_i) \tag{4.4}$$

$$w_{theo_p} = \sqrt{\frac{8}{\pi e} \cdot \frac{\lambda \cdot P}{\rho \cdot C_p \cdot v \cdot (T_m - T_o)}} \tag{4.5}$$

4.4.2 Double Laser Track

For the double laser scan track scenario (Case 2), the feature is represented, in the CAM, by two laser scan tracks in the scanning direction (Y). The hatch distance or hatch spacing determines the distance between the scan tracks. This is illustrated in Figure 4. 5 and a schematic is shown in Figure 4. 6.

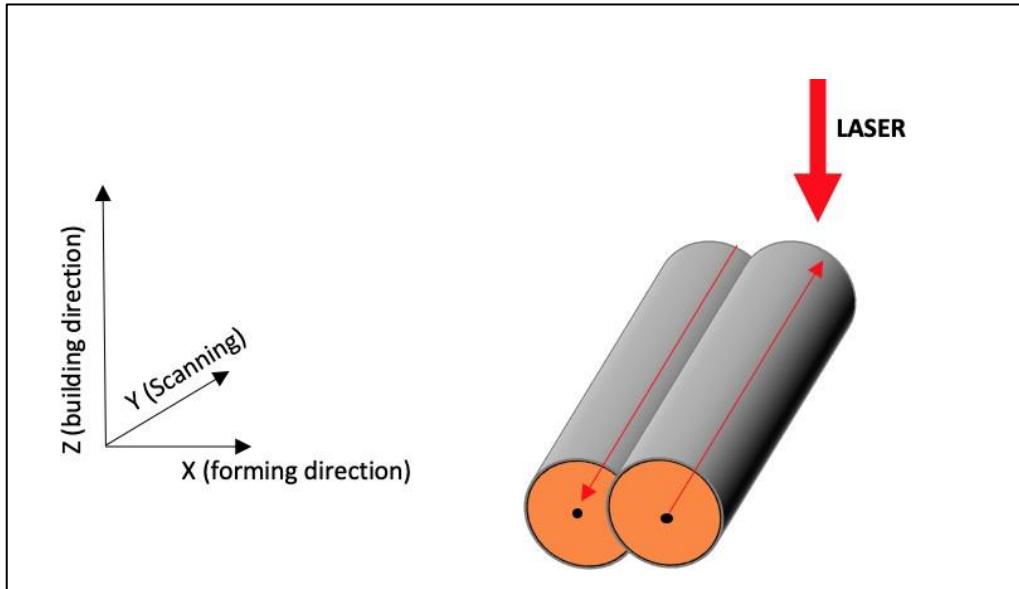


Figure 4. 5: Illustration of theoretical feature width for Case 2 (Double Laser Track)

In the Case 2 condition, the melt-pool width, w_{mp} is equal to the width calculated based on the build parameters and material properties. Similar to Case 1, it can be assumed that the build parameters are the same as the infill parameters, then $w_{mp} = w_i$, where w_i is the infill melt-pool width. In addition, the number of contours $n_c = 0$ and the number of infills, $n_i = 2$.

Hence, by referring to the generic formula (equation 4.3) and substituting for Case 2, $w_{mp} = w_i$, $n_c = 0$, $n_i = 2$, the formula for determining the theoretical peak width for Case 2 is shown in equation 4.6.

$$w_{theo_p} = (w_i) + 2(0 - 1)h_c + 2(0) + (2 - 1)h_i$$

$$w_{theo_p} = \left(\sqrt{\frac{8}{\pi e} \cdot \frac{\lambda \cdot P}{\rho \cdot C_p \cdot v (T_m - T_o)}} \right) + h_i \quad (4.6)$$

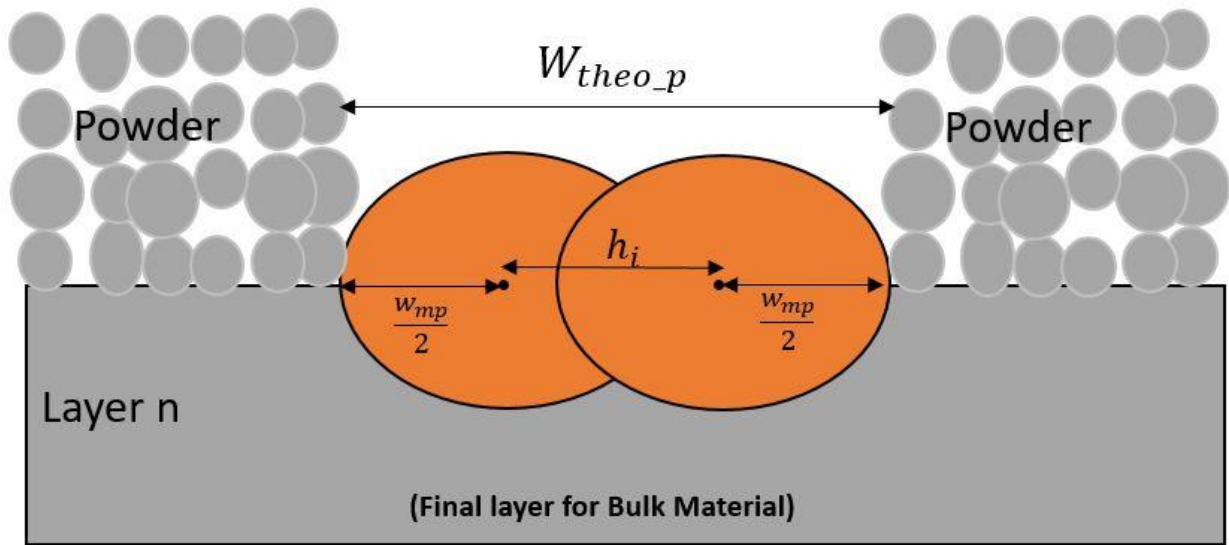


Figure 4. 6: Schematic of Case 2 feature width (X-Z plane)

4.4.3 Case 3: Contouring and Infill Laser Track

For Case 3 (contouring and infill laser track), the feature is represented by a contour scan and an infill laser scan in the scanning direction (Y). Similar to Case 2, the hatch distance or hatch spacing determines the distance between the scan tracks. For Case 3, the hatch distance will be the distance between the contour scan and the infill scan track. This is illustrated in Figure 4. 7 and Figure 4. 8 shows the schematic diagram of the mode of track filling for Case 3.

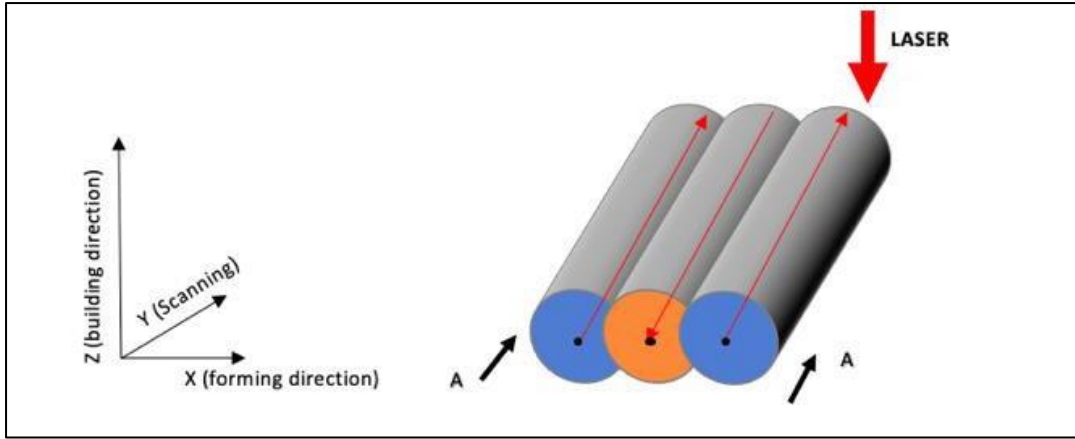


Figure 4. 7: Illustration of the theoretical feature width for Case 3 (Contouring and Infill)

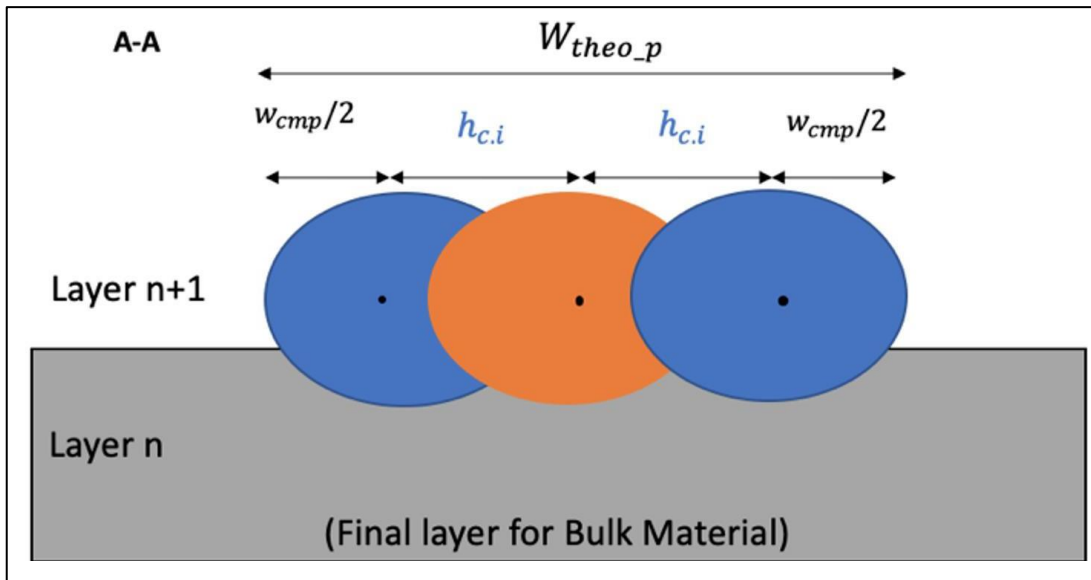


Figure 4. 8: Schematic of the theoretical feature width for Case 3 (Contouring and Infill Laser Track)

To develop the theoretical peak width equation for Case 3 condition, the melt-pool width, w_{mp} is equal to the width calculated based on the contour build parameters. Hence $w_{mp} = w_{cmp}$, where w_{cmp} is the contour melt-pool width. In addition, the number of contours $n_c = 2$ (based on the cross section in the X-Z plane) and the number of infills, $n_i = 1$. By referring to the generic formula, substituting for Case 3 conditions, $w_{mp} = w_{cmp}$, $n_c = 1$ (based on a single continuous contour track), $n_i = 1$ into equation 4.3, the formula for determining the theoretical peak width for Case 3, contouring and infill laser track is shown in equation 4.7.

$$w_{theo_p} = (w_{cmp}) + 2(1 - 1)0 + 2h_{c,i} + (1 - 1)h_i$$

$$w_{theo_p} = \left(\sqrt{\frac{8}{\pi e} \cdot \frac{\lambda \cdot P}{\rho \cdot C_p \cdot v(T_m - T_o)}} \right) + 2h_{c,i} \quad (4.7)$$

4.5 Validating the new model using parts produced by LPBF (continuous laser)

4.5.1 Experimental setup

To evaluate the accuracy of the parametric model described in the previous section, six samples were produced by the LPBF process using an SLM280 machine equipped with a 700W continuous laser and a printing volume of 280 x 280 x 365 mm. The material used was AlSi7Mg, whose chemical composition is shown in Table 4. 3. Aluminium alloys are generally used in aerospace application due to their high strength, corrosion resistance and low weight. The four main parameters that were varied were:

- Laser Power.
- Hatch Spacing.
- Build Position.
- Build Height.

Table 4. 3: Chemical composition of AlSi7Mg (MSE Supplies LLC, 2022)

Element	Si	Mg	Cu	Ti	Fe	Mn	Zn	Al
%	6.5-	0.5-	<0.05	<0.30	<0.20	<0.1	<0.1	Bal.
Composition	7.5	0.8						

4.5.1.1 Variations in Laser Power and Hatch Spacing

The energy input is expressed in the form of Volumetric Energy Density (VED) and this is used to determine whether the metal powder will sufficiently melt to create a high density part (Galimberti *et al.*, 2016). The VED is calculated using equation 4.8 (Tang *et al.*, 2017).

$$VED = \frac{P}{v \cdot h_s \cdot t} \quad (4.8)$$

Where VED is Volumetric Energy Density, Jmm^{-3} , P is laser power, W, v is laser speed, $mm s^{-1}$, h_s is hatch spacing in mm and t is the layer thickness in mm. As shown in Figure 4. 9, the hatch spacing is the distance between two successive melt- pools and increasing this spacing result in an increase between the centres of two successive melt-pools, which may result in lack of fusion porosity in the part.

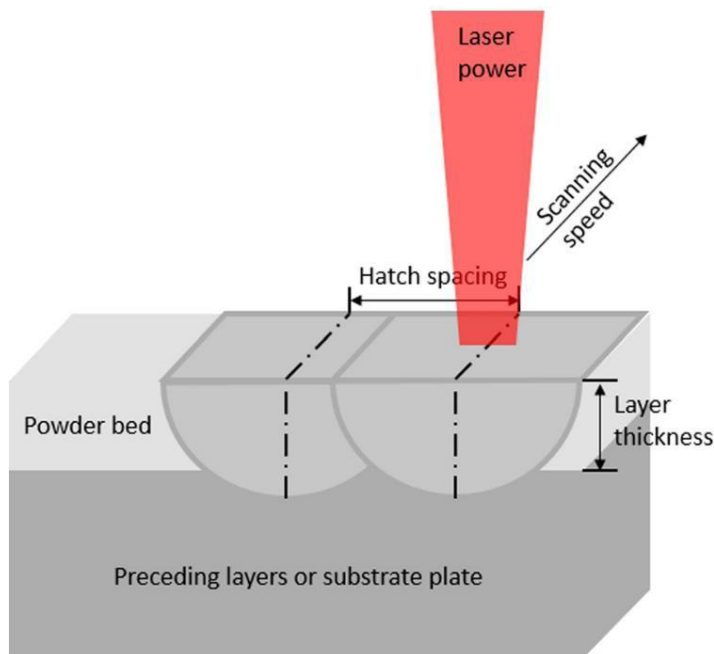


Figure 4. 9: Schematic of SLM system showing hatch spacing, laser power, scan speed and layer thickness (Yap et al., 2015).

To ensure a stable AM process and staying within appropriate processing windows of the materials used while adopting the Rosenthal equation, it was decided to keep the VED constant while evaluating effect of variations in build parameters (e.g., laser power and hatch spacing) on the model accuracy. With the Magics software (SLM 280 system standard slicing software), this was achieved by maintaining a constant scanning speed of $2100mm s^{-1}$ and $600mm s^{-1}$ (default manufacturing laser speed for processing the AlSi7Mg material) for the hatch and contour scans respectively while

finding suitable laser power and hatch spacing settings to keep the VED within a targeted range. Three build strategies (X, Y and Z) were used, keeping similar VED with different combinations of laser power and hatch spacing. The strategy X used the recommended setting provided by the manufacturer (SLM Solutions for AlSi7Mg), with hatch power 650W, contour power 350W and hatch spacing 0.17mm, which lead to a VED of approximately 36.41J/mm³. This was used as reference for build strategy Y and Z manufacturing settings. For Strategy Y, the hatch spacing was reduced to 0.13mm to keep the VED within a range of 36J/mm³±1.1% the contour and hatch power and were reduced to 500W and 270W respectively, which lead to a VED of approximately 36.63J/mm³. Likewise, for Strategy Z, the hatch distance was reduced to 0.15mm and the hatch and contour power were reduced to 580W and 310W.

All six samples were manufactured by applying the strategies in Table 4. 4, with each strategy applied to fabricate two samples. Hence the Default Strategy X, Strategy Y and Strategy Z were applied to Sample number 1, 2; Sample 3, 4; and Sample 5, 6 respectively.

Table 4. 4: Input parameters for the manufacture of samples 1-6 in AlSi7Mg material.

Sample No.	Strategy	Hatch Power (W)	Contour Power (W)	Hatch Spacing (mm)	Calculated V.E.D (J/mm ³)
1	X	650	350	0.17	36.41
2					
3	Y	500	270	0.13	36.63
4					
5	Z	580	310	0.15	36.82
6					

4.5.1.2 Variation in Feature Size and Build position.

The basis of the feature design resembles a set of six rectangular extrusion with height varying from 0.1 to 0.3mm with increments of 0.1mm (100 μ m). The process parameters from Table 4. 4 in combination with the powder thermophysical properties, were used to calculate the theoretical feature widths for Case 1, Case 2, and Case 3. Six samples were produced to compare the effect of build position on the feature size for each build strategy X, Y and Z. The samples were designed using CATIA V5 software with dimensions of 30x15x 4mm (LxWxH). The geometry shown in Figure 4. 10, was selected due to its simplicity of manufacture for demonstrating Case 1, 2 and 3 with considerations for measurement with the optical profilometer. Figure 4. 10 illustrates the CAD Design for Sample 1 with section view showing design feature widths 0.3mm (Case 1), 0.47mm (Case 2), 0.66mm (Case 3). After the completion of the 3D design process, samples 1-6 were positioned on the build platform, parallel to the X-Y plane, as indicated in Figure 4. 11.

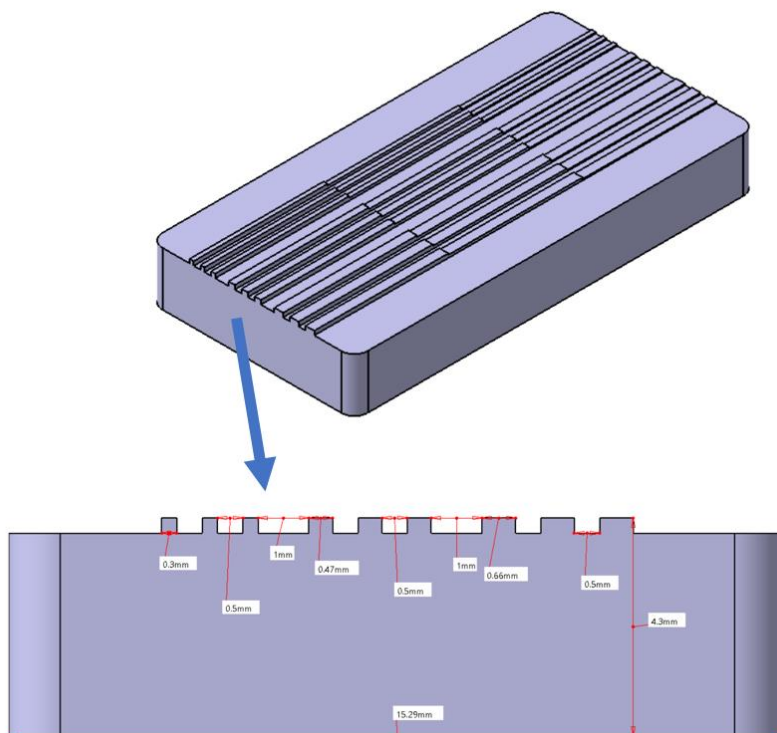


Figure 4. 10: CAD Design for Sample 1 with section view showing design feature widths 0.3 (Case 1), 0.47 (Case 2), 0.66 (Case 3).

The build position shown in Figure 4. 11 were determined by the machine operators as the best based on the number of manufactured parts and the size of the build plate.

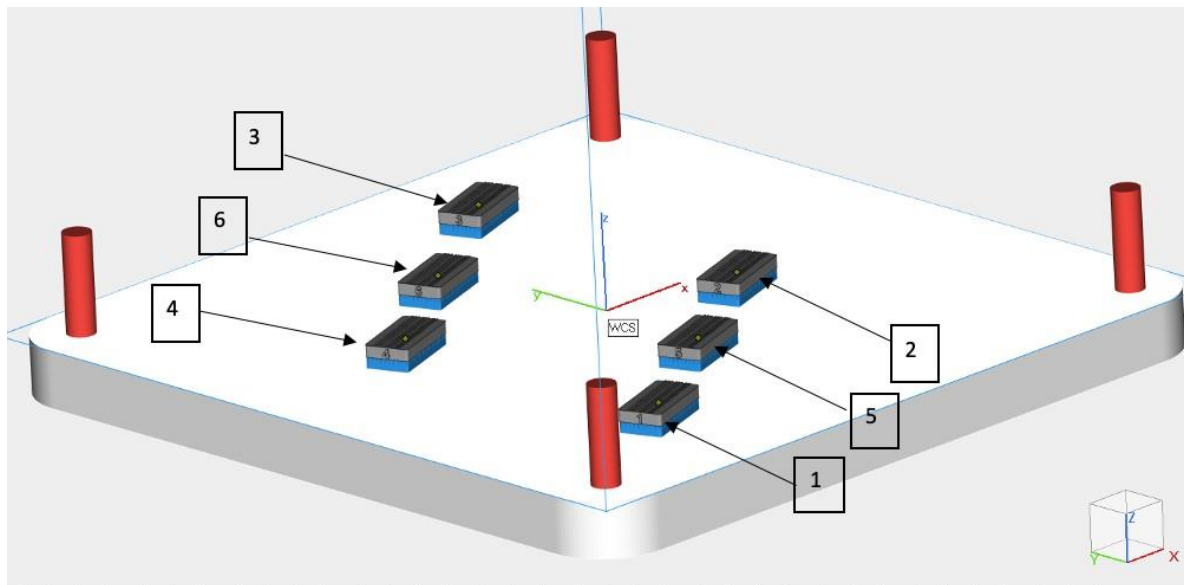


Figure 4. 11: Pre-manufacture of AlSi7Mg showing build positions for samples 1-6 on the build platform.

4.5.1.3 Features Widths Characterisation

The measured data characterisation process is represented in Figure 4. 13. Sensofar Smart 3D profiler was used to scan each feature using a 10x magnification lens with optical resolution of $0.55\mu\text{m}$ (Sensofar, 2019) and the Focus Variation (FV) technology. The FV method was selected out of other optical technologies such as confocal microscopy and interferometry because FV is easy to operate, requires less measurement time and gives an ideal balance between measured topographic datapoints and quality of results (Newton et al., 2018).

Scanned datapoints were used to generate three-Dimensional (3D) surface profiles of the features. These 3D profiles were used for the evaluation of the feature widths by extracting Two-Dimensional (2D) profiles from the 3D profiles. The measured points from the extracted 2D profiles were averaged followed by the calculation of their standard deviations. The measurement positions P1, P2 and P3 are shown in Figure 4. 12.

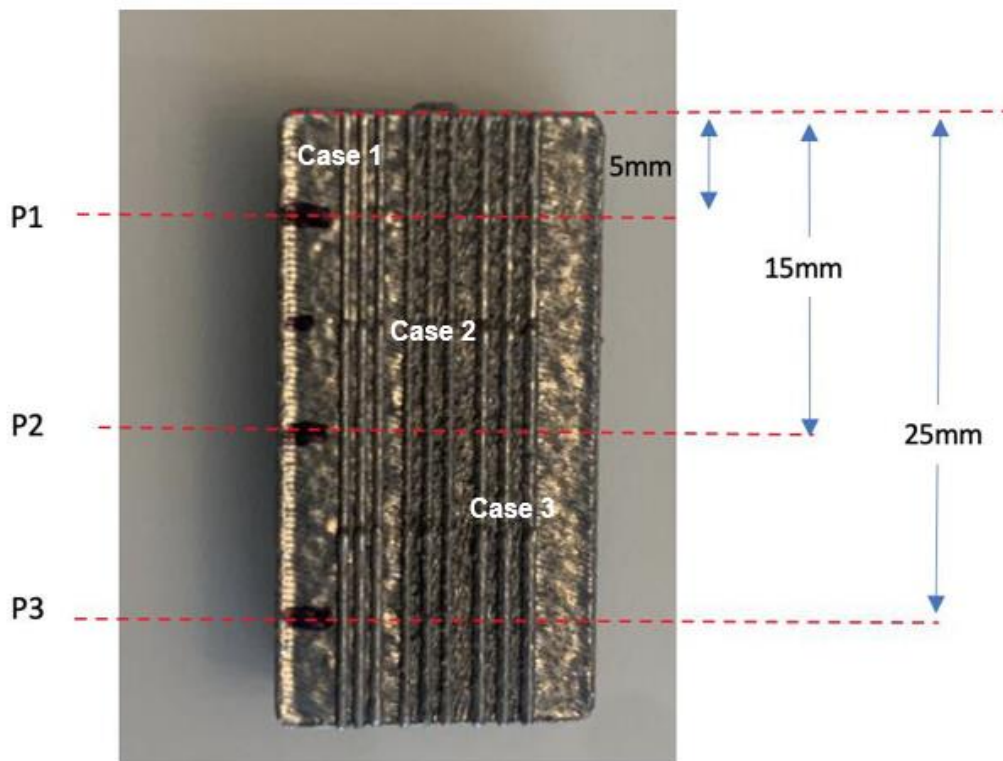


Figure 4. 12: Plan view of sample measurement positions P1, P2 and P3 corresponding to feature height 0.10, 0.20 and 0.30mm.

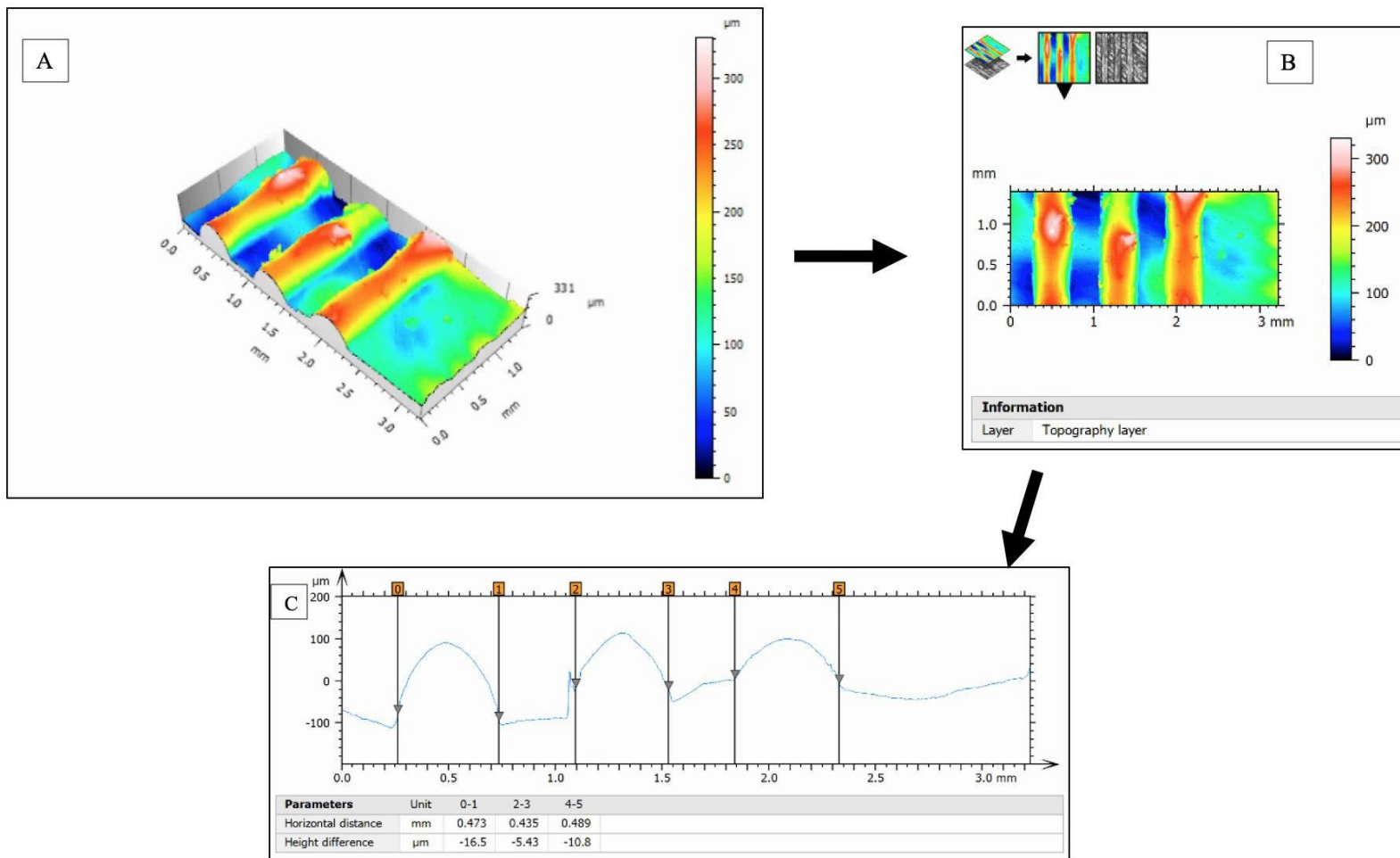


Figure 4. 13: Procedure for characterising feature widths on Sensomap Software showing 3D view (A), plan view (B) and extracted profile (C).

4.5.2 Results Summary for Continuous Laser Samples

Figure 4. 14 shows the average measured widths and the corresponding standard deviations for Samples 1 (average width for samples 2 to 6 in Section 9.1: Appendix 1). For all samples, the standard deviations from the mean remain relatively stable with changes in measurement positions 1, 2 and 3.

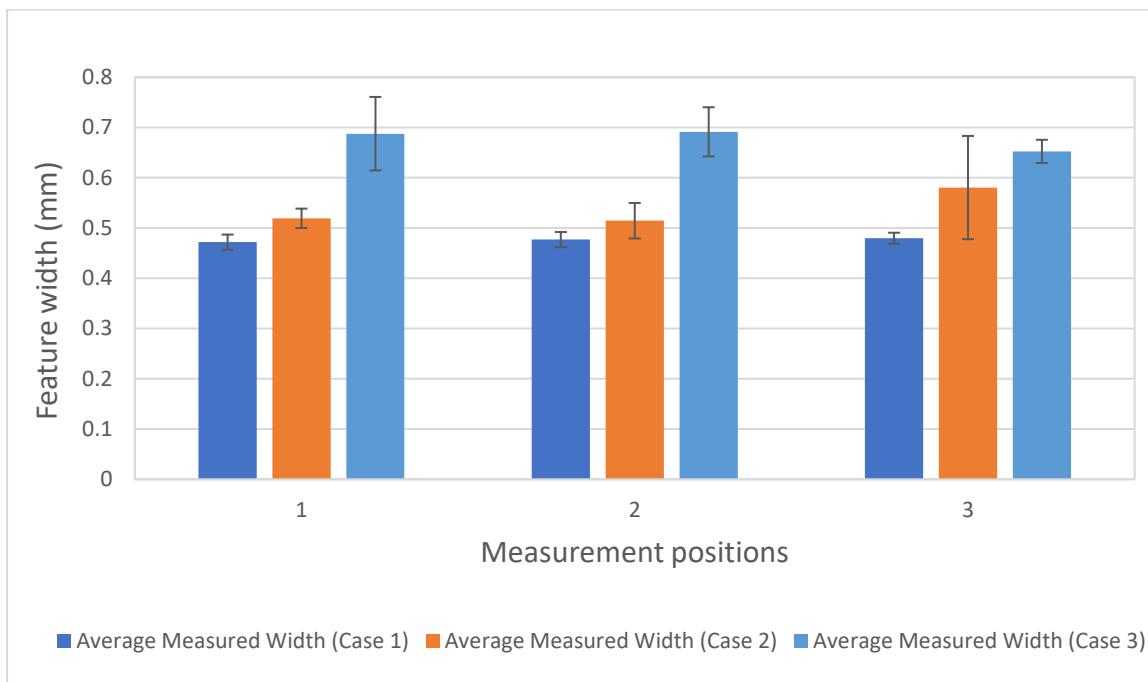


Figure 4. 14: Average measured width and standard deviations for Sample 1.

4.5.2.1 Positional Variation in Feature Width (Continuous Laser)

A comparison was made between samples with the same build parameters but at different build positions. The aim of this exercise was to clarify the influence of build position on the accuracy and repeatability of the measured feature widths. A summary of the percentage differences in measured widths for Case 1, 2 and 3 are shown in Table 4. 5 - Table 4. 7.

Sample 1 and Sample 2 were built with the same build parameters (Strategy X, refer to Table 4. 4) with the main variation being the position on the build plate. The observed difference in measured width ranged from 0.19% (H2, Case 1) to 17.88% (H3 case 2) which is higher than the repeatability error of measurement on a single location thus displaying a non-negligible effect of the print location. About 88% of the features built on sample 1 were also larger than features on sample 2. Most of the time sample 1 features were bigger than sample 2 features.

There appears to be an influence of build height on the difference in measured width however, there is no clear pattern as the maximum and minimum difference varies depending on Case 1, 2 and 3.

Table 4. 5: Percentage Difference in Measured width with Sample 1 as reference (Sample 1- Sample 2).

Case	Height	Difference in Measured Width (%)
1	H1	6.33
	H2	0.19
	H3	0.49
2	H1	10.40
	H2	7.13
	H3	17.88
3	H1	9.92
	H2	6.03
	H3	1.72

Table 4. 6: Percentage Difference in Measured width with Sample 3 as reference (Sample 3- Sample 4).

Case	Height	Difference in Measured Width (%)
1	H1	4.26
	H2	7.67
	H3	-0.70
2	H1	-17.64
	H2	-10.72
	H3	-4.35
3	H1	-2.03
	H2	-0.94
	H3	-4.43

Similarly, Sample 3 and Sample 4 were built with the same build parameters (Strategy Y, see Table 4. 4) with variation in the position on the build plate. The observed difference in measured width ranged from 0.94% (H2, Case 3) to 17.64% (H1 case 2). For samples 3 and 4, there seems to be no clear pattern on the influence of build height on feature width for Case 1, 2 and 3 for samples 3 and 4.

Table 4. 7: Percentage Difference in Measured width with Sample 5 as reference (Sample 5- Sample 6)

Case	Height	Difference in Measured Width (%)
1	H1	-4.15
	H2	-0.52
	H3	2.87
2	H1	0.89
	H2	-0.77
	H3	4.07
3	H1	0.22
	H2	3.41
	H3	0.63

Also, Sample 5 and Sample 6 were built with the same build parameters (Strategy Z, refer to Table 4. 4) with the main variation in the position on the build plate. The observed difference in measured width ranged from 0.22% (H1, Case 3) to 4.15% (H1 case 1). Overall, Samples 5 and 6 have better dimensional precision compared to Sample pairs 1, 2 and 3,4. Samples 5 and 6 were built at the centre of the build platform (Figure 4. 11). It is probable that the central position favours higher geometric precision compared to the outer positions.

4.5.2.2 Prediction Accuracy with Developed Model

From Figure 4. 16, the vertical axis of the graph shows the average percentage error of the model prediction for each case at given heights H1, H2 and H3 corresponding to 0.1, 0.2 and 0.3mm respectively. For the nine width measurements performed at each height, the Mean Percentage Errors (MPE) of the prediction and the standard deviations (STD) recorded in Table 4. 8 were determined as follows:

$$PE_n = \left(\frac{|pWidth - mWidth_n|}{mWidth_n} \right) \times 100 \quad (4.9)$$

$$MPE = \left(\sum_{n=1}^9 PE_n \right) / 9 \quad (4.10)$$

$$STD = \sqrt{\sum_{n=1}^9 (PE_n - MPE)^2 / 9} \quad (4.11)$$

Where, for a width measured n times, $pWidth$ is the predicted width and $mWidth_n$ is the value of the n^{th} measured width.

Horizontal axis shows Case 1-2 for samples 1- 6. A total of 54 bars are plotted together with respective standard deviations. For Sample 1, the maximum and minimum average percentage error were 37.72 (Case 1) and 3.72 (Case 3). Percentage error for Case 2 and Case 3 ranges from 3 to 17%.

This is a much better accuracy compared to Case 1 however, there is room for improvement for Cases 2 and 3. In all cases, particularly for Case 1, the theoretical model under predicted the minimum feature size because the measured width from the experiment was always larger than the theoretical predicted width. Generally, the maximum MPE was in Case 1 and the minimum MPE varied between Case 2 and Case 3.

From Table 4. 8, MPE coloured in Blue, Orange or Red refer to positions where the highest MPE was calculated for each Case at either H1 (0.1mm), H2 (0.2mm) or H3 (0.3mm). It shows that generally, MPE increases with increase in build height H, with H3 usually showing the largest error in Red. A possible explanation for this variation could be linked to the double scan effect shown in Figure 4. 15 which has not been accounted for in the original equation.

After close examination of the CAM layer 123 (Figure 4. 15), it was noticed that the Case 1 features were represented differently from Case 2 and Case 3. For each laser path, a small circle at the beginning of the path indicates the starting position of the laser and an arrow represents the end position. From Figure 4. 15, A and B (Case 2), the circle and arrow can be seen at two distinct positions indicating a single laser pass at each position. However, for C and D (Case 1), the circle and arrow are both in the same position, indicating that the laser scanned twice at the same location. This suggests that there will have been more power exposure to the powder than initially estimated with the prediction model, hence a significantly higher percentage error in Case 1 compared to Case 2 and Case 3.

This possibility of underestimation of the effect of the power parameter (Case 1), the hatch spacing, and speed parameters (Case 2 and Case 3) needs to be investigated further as these factors affect the melt-pool size and ultimately the feature width.

The next step was to determine the feasibility of tuning the current model to predict the actual width more accurately from manufacturing. This could compensate for the potential underestimation mentioned above.

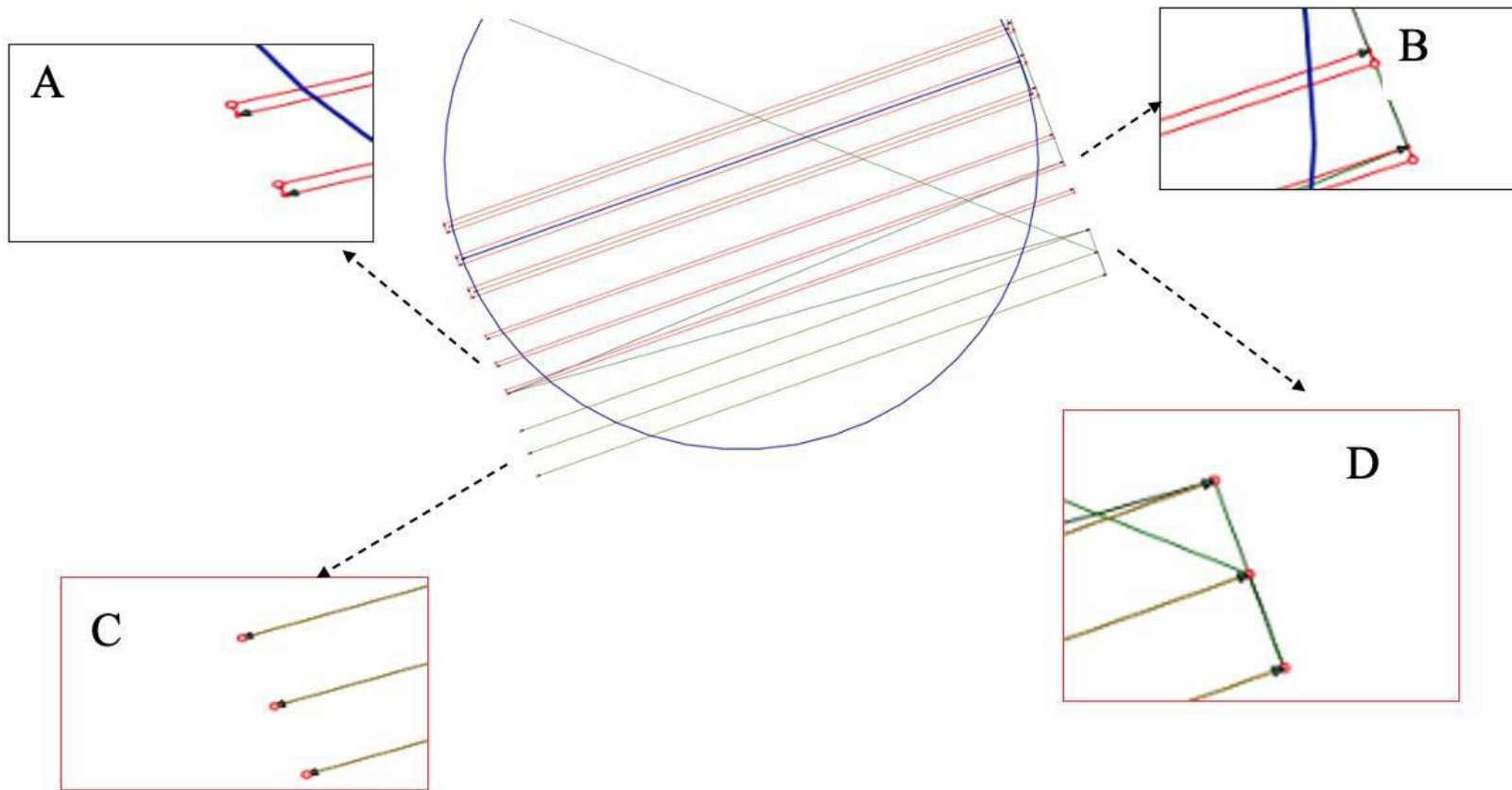


Figure 4. 15: Build layer comparing Left- and Right-hand laser track for Case 2 (A, B) to Case 1 (C, D)

Table 4. 8: Mean Percentage Errors (MPE) and standard deviations from the mean. MPEs in red, orange, and green indicate the maximum MPE for each Case.

Sample Number	Case	Height	MPE	Standard Deviation
1	1	H1	36.65%	2.13%
		H2	37.33%	2.03%
		H3	37.72%	1.41%
	2	H1	9.64%	3.20%
		H2	8.51%	6.03%
		H3	17.57%	13.10%
	3	H1	6.72%	6.73%
		H2	5.19%	4.80%
		H3	3.72%	2.61%
2	1	H1	32.30%	2.99%
		H2	37.19%	2.30%
		H3	38.03%	1.30%
	2	H1	3.56%	1.25%
		H2	3.19%	3.20%
		H3	2.02%	1.45%
	3	H1	8.45%	5.95%
		H2	5.18%	3.51%
		H3	5.12%	4.02%
3	1	H1	34.71%	2.47%
		H2	37.22%	3.58%
		H3	40.75%	2.76%
	2	H1	5.37%	3.86%
		H2	5.30%	4.16%
		H3	9.00%	4.74%
	3	H1	3.44%	2.46%
		H2	5.03%	2.63%
		H3	2.26%	0.76%

Sample Number	Case	Height	MPE	Standard Deviation
4	1	H1	31.86%	1.76%
		H2	32.05%	3.54%
		H3	41.23%	1.83%
	2	H1	10.94%	5.34%
		H2	13.71%	4.87%
		H3	12.79%	4.69%
	3	H1	3.36%	3.09%
		H2	5.19%	2.63%
		H3	3.71%	2.88%
5	1	H1	22.32%	3.54%
		H2	26.06%	4.04%
		H3	31.09%	3.02%
	2	H1	3.92%	2.76%
		H2	4.72%	2.76%
		H3	7.89%	3.80%
	3	H1	7.26%	2.62%
		H2	5.94%	2.53%
		H3	4.46%	2.69%
6	1	H1	25.47%	2.70%
		H2	26.44%	4.18%
		H3	28.54%	6.80%
	2	H1	2.98%	2.06%
		H2	5.10%	3.70%
		H3	4.69%	2.86%
	3	H1	8.05%	3.74%
		H2	9.67%	2.42%
		H3	5.16%	2.68%

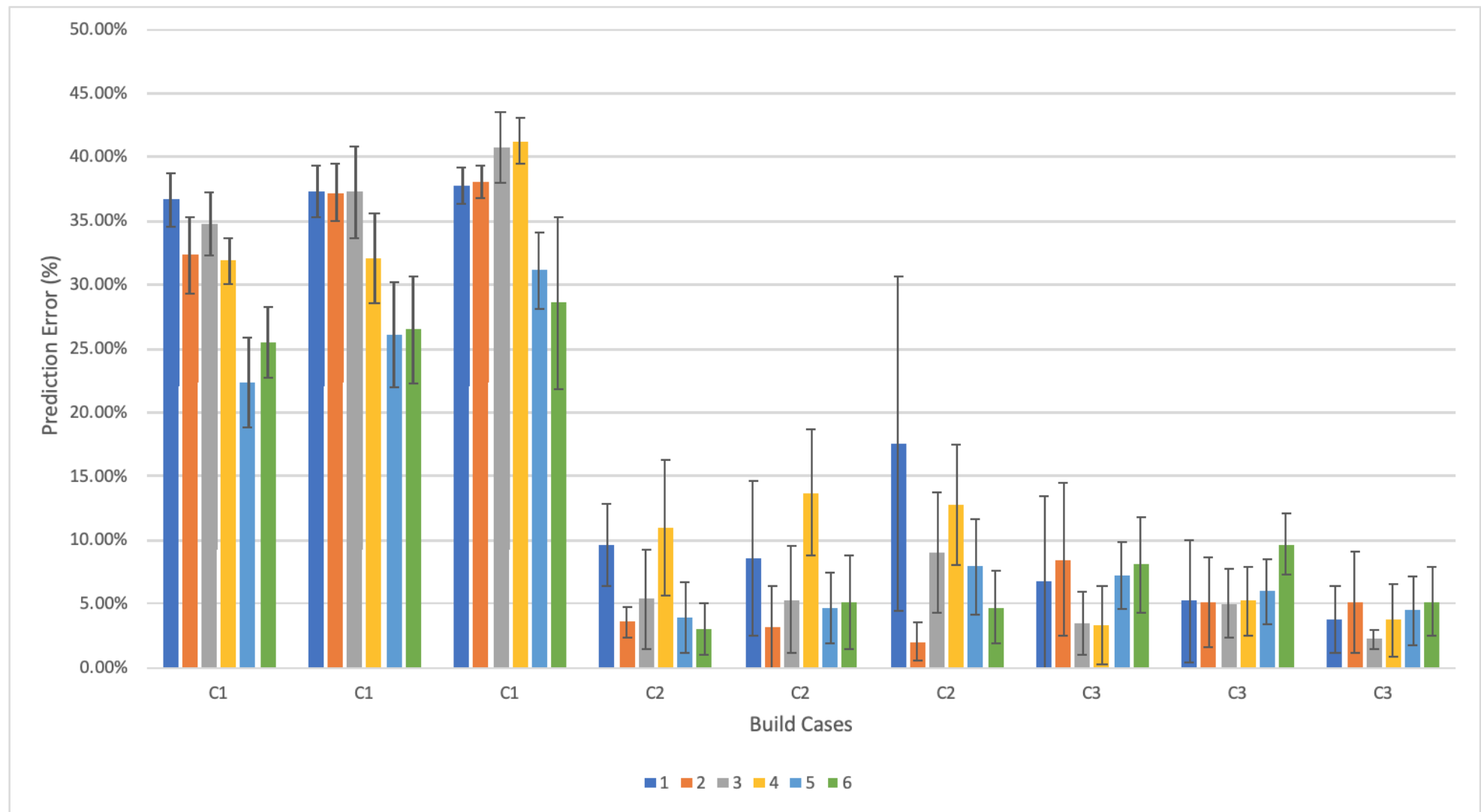


Figure 4. 16: Plot of MPE and standard deviations for samples 1-6. Where C1, C2, C3 represent Case 1, Case2, Case 3.

The overall difference in MPE for Samples 1 and 2 ranges from low of 0.01% to 15.55%. When comparing the difference in MPE, height, H2, had the minimum range from 0.01 (Case 3) to 5.32 (in Case 2). This suggest that H2 has the highest precision compared to H1 and H3

Table 4. 9: Difference in MPE for Case 1, 2 and 3 features (Sample 1- Sample 2)

Case	Height	Difference in M.P. E
1	H1	4.35%
	H2	0.14%
	H3	0.31%
2	H1	6.08%
	H2	5.32%
	H3	15.55%
3	H1	1.73%
	H2	0.01%
	H3	1.40%

Similarly, Sample 3 and 4 have an overall difference in MPE ranges from low of 0.08% to a high of 8.41%. This PE range is about 50% lower than that of samples 1 and 2. When comparing the difference in MPE, Height, H2, always has the smallest difference, ranging from 0.01 (Case 3) to 5.32 (in Case 2).

Table 4. 10: Difference in Mean Prediction Error (PE) for Case 1, 2 and 3 features (Sample 3- Sample4)

Case	Height	Difference in M.P. E
1	H1	2.85%
	H2	5.17%
	H3	-0.48%
2	H1	-5.57%
	H2	-8.41%
	H3	-3.79%
3	H1	0.08%
	H2	-0.16%
	H3	-1.45%

Also, Sample 5 and 6 have an overall difference in MPE ranges from low of 0.38% to a high of 3.73%. This MPE range is over 50% lower than that of samples 3 and 4. Similarly, when comparing the difference in MPE based on height, H2, always has the smallest difference, ranging from 0.01 (Case 3) to 5.32 (in Case 2). This suggests that the height parameter may have an impact on the prediction accuracy and should be considered when predicting feature width.

Table 4. 11: Difference in Mean Prediction Error (PE) for Case 1, 2 and 3 features (Sample 5- Sample 6)

Case	Height	Difference in M.P. E
1	H1	-3.15%
	H2	-0.38%
	H3	2.55%
2	H1	0.94%
	H2	-0.38%

	H3	3.20%
--	----	-------

Case	Height	Difference in M.P. E
3	H1	-0.79%
	H2	-3.73%
	H3	-0.70%

Of all three sample pairs, samples 5 and 6 (positioned in the middle of the build plate) have lower MPE difference followed by samples 3 and 4 and finally samples 1 and 2 (positioned on the left- and right-hand side of samples 5 and 6).

4.6 New Tuneable Metal AM Feature Width prediction Model

4.6.1 Model modified using Optimised Coefficients.

In section 4.5, the Rosenthal equation and hatch spacing were used to predict the theoretical feature width for Case 1, 2 and 3. This is summarised in equations 4.3-4.7. The parameters which can be varied in this equation are power, speed and hatch spacing. Layer height may be varied as well as a function of the build height. The relatively poor width prediction accuracy of the developed model may be due to discrepancy between the theoretical parameters used in the equation to the actual parameter value delivered by an AM machine. Thus, it is proposed to modify the model to facilitate its tuning, using real experiment. by enabling modification of the influence of machine parameters (power, speed, hatch spacing and layer height) on the predicted widths.

This can be achieved by multiplying these parameters with coefficients that can be optimised based on the widths measured experimentally. These equations are applicable in general however, the coefficients will be specific for a given machine and material combination.

For Cases 1 and 2:

$$w_{\text{theo}_p} = \left(\sqrt{\frac{8}{\pi e} \cdot \frac{\lambda \cdot C_f_p \cdot P}{C_f_s \cdot \rho \cdot C_p \cdot v(T_m - T_o)}} \right) + C_f_h \cdot h_i + C_f_{Lh} \cdot Lh \quad (4.12)$$

For Case 3:

$$w_{\text{theo}_p} = \left(\sqrt{\frac{8}{\pi e} \cdot \frac{\lambda \cdot C_f_p \cdot P}{C_f_s \cdot \rho \cdot C_p \cdot v(T_m - T_o)}} \right) + C_f_h \cdot 2h_{c,i} + C_f_{Lh} \cdot Lh \quad (4.13)$$

Where C_f_p , C_f_s , C_f_h and C_f_{Lh} refer to the coefficient of power, speed, hatch spacing and layer height respectively.

The algorithm chosen for the optimisation process is the Limited Broyden–Fletcher–Goldfarb–Shanno algorithm (L-BFGS) with C++ programming environment. This algorithm enables a reference value to be matched to an observation. For this experiment, the algorithm uses the equations and specified boundaries to define coefficients. This algorithm was selected because it is well established and easy to apply with specific boundaries (Byrd *et al.*, 1995). The optimisation algorithm was run to determine which coefficients Cf_p , Cf_s , f_h and Cf_{Lh} returned the best results for the predicted feature widths. The boundaries selected for Cf_p , Cf_s , were 0.1,10 to avoid negative square root for w_{theo_p} calculation. In addition, the boundaries for layer height were specified as -10:10 because there might be a negative error due to the melting and solidification of metallic powder for the final layer, unevenness of the build surface layer and thermal shrinkage.

4.6.2 Model modified using coefficients optimised to all LPBF continuous laser data.

A first optimisation process was performed using all LPBF continuous laser data to investigate if a more accurate model can indeed be generated.

Table 4. 12 shows the results from the optimisation process for samples 1-6. Mean Percentage Error (MPE) in red and green indicate the maximum and minimum MPE respectively, for a particular sample. By comparing the MPE from the optimised to the original model, a significant reduction in the error can be observed particularly for Case 1 (single scan). In the initial model, the MPE ranged from 30-40% in Case 1 whereas in the optimised model, the MPE ranges from 3-13%. From the graphical representation in Figure 4. 17, the MPE for all cases varies between 2 and 15%. Previously, the standard deviations for the original model were lower however for the optimised model, standard deviations are higher.

After optimising the predicted widths for Case 1, Case 2, and Case 3 to all the data from the experiment, the overall prediction error reduced significantly. A summary of the coefficients of power, speed, hatch spacing, and layer height are shown in Table 4. 13.

From Table 4. 13, the following observations were made:

- The coefficient of Power, 1.36, implies that the effect of power in the original model was underestimated by 36%. Higher power effect means that more energy was available to melt the powder than was originally accounted for in the original equation. This resulted in larger melt pool formation in the actual feature compared to the predicted feature.
- For Speed, a 32% decrease in the influence of speed is suggested by the coefficient of 0.68. Hence, the original model overestimates the effect of speed by 32%. Lower effect of speed implies more time for the powder to be exposed to the laser hence larger melt-pool width.
- Also, the Hatch spacing optimisation coefficient decreases the impact of hatch spacing by 73%. This is particularly significant for Case 2 and Case 3 scenarios where multiple scans are present.
- The height coefficient of 0.1. In the original equation, the layer height was not included however, from the optimised equation, the height coefficient of 0.1 makes the height parameter insignificant compared to power, hatch spacing and speed.

The results achieved are a significant improvement from the original model. However, this may be due to overfitting the data, which may not guarantee the prediction accuracy outside of the experimental space provided by the tuning process.

It is therefore proposed to evaluate the possibility of tuning the model to a single sample from the experimental set. This will be discussed in section 4.6.3.

Table 4. 12: Results samples 1-6 showing the Mean Percentage Error (MPE) and standard deviations.

Sample Number	CASE	Height	Original Model		Optimised Model	
			Mean Percentage Error (MPE)	Standard Deviation	MPE	Standard Deviation
1	Case 1	H1	36.65%	2.13%	7.85%	3.09%
		H2	37.33%	2.03%	6.27%	2.66%
		H3	37.72%	1.41%	3.96%	2.17%
	Case 2	H1	9.64%	3.20%	7.51%	3.28%
		H2	8.51%	6.03%	5.87%	4.50%
		H3	17.57%	13.10%	13.71%	12.11%
	Case 3	H1	6.72%	6.73%	6.79%	6.94%
		H2	5.19%	4.80%	5.18%	4.58%
		H3	3.72%	2.61%	5.78%	3.03%
2	Case 1	H1	32.30%	2.99%	3.64%	2.82%
		H2	37.19%	2.30%	5.89%	3.44%
		H3	38.03%	1.30%	4.43%	2.00%
	Case 2	H1	3.56%	1.25%	4.51%	2.06%
		H2	3.19%	3.20%	4.67%	2.91%
		H3	2.02%	1.45%	6.14%	1.99%
	Case 3	H1	8.45%	5.95%	6.95%	5.86%
		H2	5.18%	3.51%	5.40%	3.83%
		H3	5.12%	4.02%	7.31%	4.66%

Sample Number	CASE	Height	Original Model		Optimised Model	
			Mean Percentage Error (MPE)	Standard Deviation	MPE	Standard Deviation
3	Case 1	H1	34.71%	2.47%	4.67%	2.91%
		H2	37.22%	3.58%	5.87%	4.62%
		H3	40.75%	2.76%	7.85%	3.70%
	Case 2	H1	5.37%	3.86%	11.35%	5.06%
		H2	5.30%	4.16%	5.61%	4.71%
		H3	9.00%	4.74%	5.03%	3.49%
	Case 3	H1	3.44%	2.46%	3.66%	2.14%
		H2	5.03%	2.63%	6.41%	3.56%
		H3	2.26%	0.76%	2.11%	0.91%
4	Case 1	H1	31.86%	1.76%	2.47%	0.88%
		H2	32.05%	3.54%	4.25%	4.19%
		H3	41.23%	1.83%	8.28%	2.85%
	Case 2	H1	10.94%	5.34%	6.37%	4.32%
		H2	13.71%	4.87%	6.04%	4.44%
		H3	12.79%	4.69%	4.76%	2.69%
	Case 3	H1	3.36%	3.09%	5.27%	3.26%
		H2	5.19%	2.63%	7.14%	3.05%
		H3	3.71%	2.88%	4.19%	2.96%
5	Case 1	H1	22.32%	3.54%	13.19%	5.16%
		H2	26.06%	4.04%	11.16%	6.08%
		H3	31.09%	3.02%	7.57%	3.28%
	Case 2	H1	3.92%	2.76%	5.08%	2.56%
		H2	4.72%	2.76%	5.40%	4.05%
		H3	7.89%	3.80%	3.22%	3.21%
	Case 3	H1	7.26%	2.62%	2.17%	1.15%
		H2	5.94%	2.53%	1.90%	1.53%
		H3	4.46%	2.69%	1.95%	2.02%

Sample Number	CASE	Height	Original Model	Optimised Model	Sample Number	CASE
6	Case 1	H1	25.47%	2.70%	8.59%	3.94%
		H2	26.44%	4.18%	10.60%	6.28%
		H3	28.54%	6.80%	12.62%	8.23%
	Case 2	H1	2.98%	2.06%	4.65%	2.68%
		H2	5.10%	3.70%	5.59%	3.37%
		H3	4.69%	2.86%	6.11%	4.03%
	Case 3	H1	8.05%	3.74%	3.87%	3.16%
		H2	9.67%	2.42%	4.03%	2.26%
		H3	5.16%	2.68%	3.03%	0.89%

Table 4. 13: Summary of Process parameters and coefficients from tuned model

Process Parameter	Power	Speed	Hatch Spacing	Layer height
Coefficient (2dp)	1.36	0.68	0.27	0.1

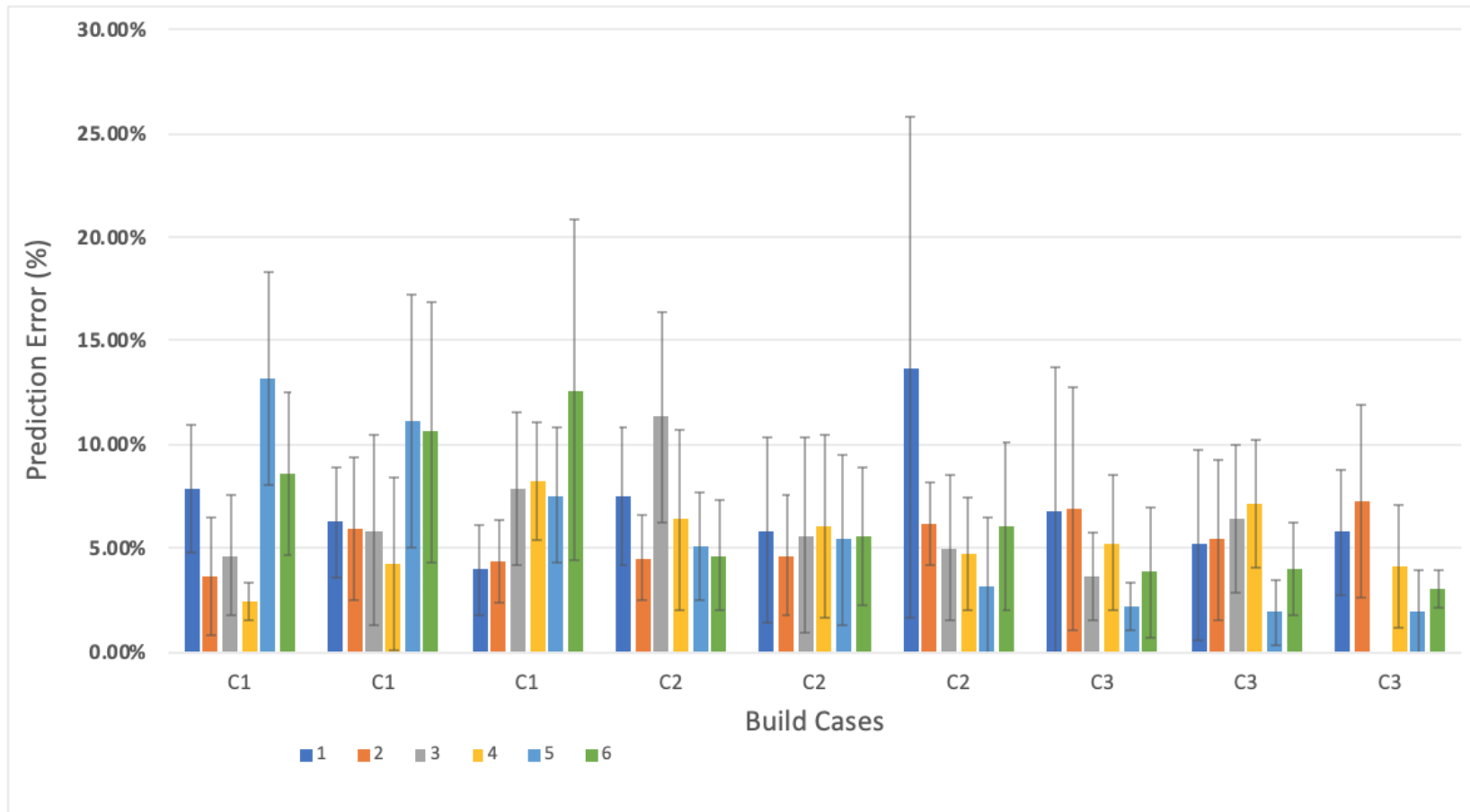


Figure 4. 17: Plot of MPE for Samples 1-6 tuned to all the experimental data. Where C1, C2, C3 represent Case 1, Case2, Case

4.6.3 Model modified using coefficients optimised using one LPBF continuous laser sample.

In this second optimisation, only the data from sample 1 was used to optimise the coefficients of the new model. A comparison of the MPE for the optimisation based on all sample data to sample 1 data is shown in Table 4. 14 and Figure 4. 18.

Table 4. 14: MPE and standard deviation comparisons between “all data” and sample 1 optimisation

Sample Number	CASE	ALL DATA OPTIMISATION		SAMPLE 1 OPTIMISATION	
		MPE	Standard Deviation	MPE	Standard Deviation
1	Case 1	7.85%	3.09%	2.80%	2.05%
		6.27%	2.66%	2.46%	2.20%
		3.96%	2.17%	2.91%	1.80%
	Case 2	7.51%	3.28%	4.08%	3.40%
		5.87%	4.50%	5.49%	3.62%
		13.71%	12.11%	14.08%	10.01%
	Case 3	6.79%	6.94%	7.27%	6.22%
		5.18%	4.58%	6.32%	2.75%
		5.78%	3.03%	8.66%	3.79%
2	Case 1	3.64%	2.82%	6.35%	3.85%
		5.89%	3.44%	3.07%	2.16%
		4.43%	2.00%	2.36%	1.74%
	Case 2	4.51%	2.06%	7.13%	3.78%
		4.67%	2.91%	7.56%	3.39%
		6.14%	1.99%	9.63%	2.06%
	Case 3	6.95%	5.86%	10.58%	6.06%
		5.40%	3.83%	7.41%	5.37%
		7.31%	4.66%	10.63%	4.80%

Sample Number	CASE	ALL DATA OPTIMISATION		SAMPLE 1 OPTIMISATION	
		MPE	Standard Deviation	MPE	Standard Deviation
3	Case 1	4.67%	2.91%	3.67%	2.67%
		5.87%	4.62%	5.32%	2.71%
		7.85%	3.70%	3.66%	3.12%
	Case 2	11.35%	5.06%	15.94%	5.27%
		5.61%	4.71%	8.88%	5.71%
		5.03%	3.49%	7.53%	4.32%
	Case 3	3.66%	2.14%	2.42%	2.48%
		6.41%	3.56%	5.05%	2.63%
		2.11%	0.91%	2.96%	1.84%
4	Case 1	2.47%	0.88%	6.86%	2.77%
		4.25%	4.19%	9.81%	5.73%
		8.28%	2.85%	2.86%	2.44%
	Case 2	6.37%	4.32%	4.73%	3.78%
		6.04%	4.44%	4.99%	2.91%
		4.76%	2.69%	4.85%	3.42%
	Case 3	5.27%	3.26%	3.65%	3.06%
		7.14%	3.05%	5.22%	2.63%
		4.19%	2.96%	2.53%	2.41%
5	Case 1	13.19%	5.16%	21.56%	5.55%
		11.16%	6.08%	18.98%	6.51%
		7.57%	3.28%	13.94%	4.99%
	Case 2	5.08%	2.56%	7.54%	4.26%
		5.40%	4.05%	8.09%	5.44%
		3.22%	3.21%	5.57%	3.94%
	Case 3	2.17%	1.15%	2.27%	2.47%
		1.90%	1.53%	3.32%	1.85%
		1.95%	2.02%	3.37%	2.66%
6	Case 1	8.59%	3.94%	16.62%	4.23%
		10.60%	6.28%	18.38%	6.72%
		12.62%	8.23%	18.66%	10.41%
	Case 2	4.65%	2.68%	7.92%	3.89%
		5.59%	3.37%	7.55%	5.38%
		6.11%	4.03%	9.70%	4.30%
	Case 3	3.87%	3.16%	4.59%	3.04%
		4.03%	2.26%	6.53%	2.35%
		3.03%	0.89%	4.37%	2.13%

In general, the MPE after optimisation with one sample data ranges from approximately 2-20%, which is 7% larger than the MPE after optimisation with all sample data which ranges from about 2-13%, and it is still a significant improvement from the original model whose prediction error ranged from about 14-48%. Also, bearing in mind that the build position variations in MPE was a maximum of 15% (Table 4. 9) and that in the context of a millimetre scale feature designed at 0.4mm, this 20% (from single sample optimisation) translates to a maximum error of $\pm 0.08\text{mm}$, this MPE can be considered acceptable at this scale.

After reviewing the summary in Table 4. 15, the following observations were made:

- The power parameter was optimised by the coefficient 1.383. Hence, an underestimation of the impact of speed by approximately 38.3% in the original model.
- In addition, the coefficient of Speed was optimised by the 0.598, meaning that the effect of power in the original model was 40.2%.
- Also, the hatch spacing parameter was optimised by the coefficient 0.182. This suggests an overestimation of the impact of hatch spacing of approximately 81.8% in the original model.
- The layer height parameter was optimised by the coefficient 0.013. This implies that similar to the initial optimisation to all data, the layer height has little influence on the feature width. The parameter effect was overestimated by 98.7%.

The main difference between the coefficients for power, speed, hatch spacing and layer height when comparing model optimisation with all data verses single sample is the magnitude of the coefficients. This will be discussed in section 4.8.

The results are promising for the AlSi7Mg material and SLM280 machine, hence the next logical step was to validate the methodology with a different combination of material and machine to evaluate if the proposed model could indeed become a generic model.

Table 4. 15: Summary of Process parameters and coefficients from tuned model to data from sample 1

Process Parameter	Power	Speed	Hatch Spacing	Layer height
Coefficient (2dp)	1.383	0.598	0.182	0.013

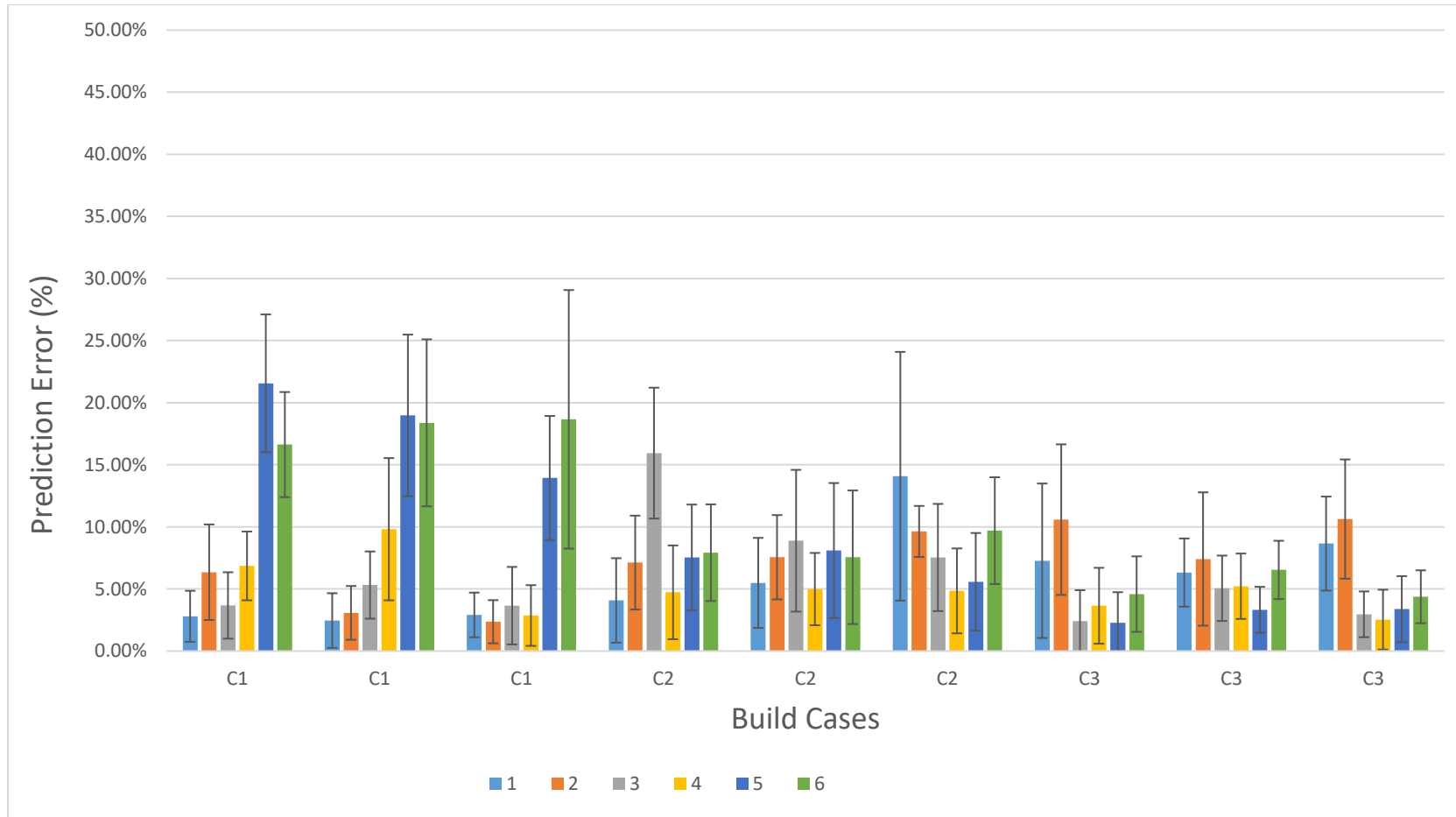


Figure 4. 18: Plot of Prediction Error for Samples 1-6 tuned to sample 1 data. Where C1, C2, C3 represent Case 1, Case2, Case 3.

4.7 New Model Validation using LPBF Pulse Width Modulated Laser (PWM)

4.7.1 Parts produced by LPBF (PWM laser)

To validate the model developed in section 4.6, six samples were produced by the LPBF process using an AM250 machine equipped with a 200W Pulse Width Modulated (PWM) laser and a printing volume of 250 x 250 x 365mm. The material used was Stainless Steel SS316L with chemical composition as shown in Table 4. 16. This was selected to compare the model to a different material and machine combination. Similar to the experiment in section 4.5, the four main parameters which were varied were:

- Laser Power
- Hatch Spacing
- Build Position
- Build height.

Table 4. 16: Chemical composition of SS316L (thyssenkrupp Materials (UK) Ltd, 2022)

Element	%Composition
C	0.03
Si	1
Mn	2
P	0.05
S	0.02
Cr	16.50-18.50
Ni	10.00-13.00
N	0.1
Mo	2.00-2.50
Fe	Bal.

Similar to section 4.5.1, three build strategies (X, Y and Z) were used, keeping the VED in the same range (in this section between 48.48 and 48.89J/mm³) while maintaining a constant scanning speed of 750mm/s⁻¹ and 200mm/s⁻¹ for the hatch and contour scans respectively. The strategy X used the recommended setting provided by the manufacturer (Renishaw for SS316L), with hatch power 200W, contour power 110W and hatch spacing 0.11mm, which lead to a VED of approximately 48.48J/mm³ (Table 4. 17).

This was used as reference for build strategy Y and Z manufacturing settings. For Strategy Y, the hatch spacing was reduced to 0.10mm and to keep the VED within a range of 48J/mm³±1.85% the contour and hatch power and were reduced to 182W and 100W respectively, which lead to a VED of approximately 48.53J/mm³. Likewise, for Strategy Z, the hatch distance was increased to 0.12mm and the hatch and contour power were reduced to 165W and 120W leading to a VED of 48.89J/mm³. The six samples were positioned on the build plate as shown in Figure 4. 19.

Table 4. 17: Input parameters for the manufacture of samples 1-6 in SS316L material.

Sample No.	Strategy	Hatch Power (W)	Contour Power (W)	Hatch Spacing (mm)	Calculated V.E.D (J/mm ³)
1	X	200	110	0.11	48.48
2					
3	Y	182	100	0.10	48.53
4					
5	Z	165	120	0.12	48.89
6					

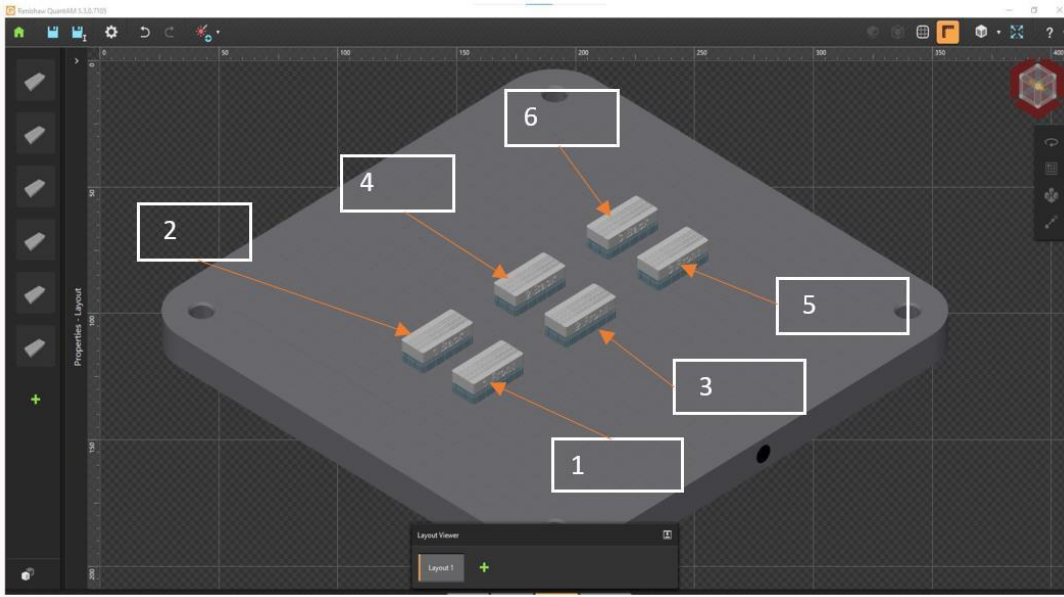


Figure 4. 19: Pre-manufacture simulation of SS316L showing build positions for samples 1-6 on the build platform.

4.7.2 Results Summary for PWM Laser samples

Figure 4. 20 to Figure 4. 25 show the average measured widths and the corresponding standard deviations for Samples 1 to 6. Similar to the AISi7Mg CL experiment, the standard deviations from the mean remain relatively stable across measured positions 1, 2 and 3 on each sample.

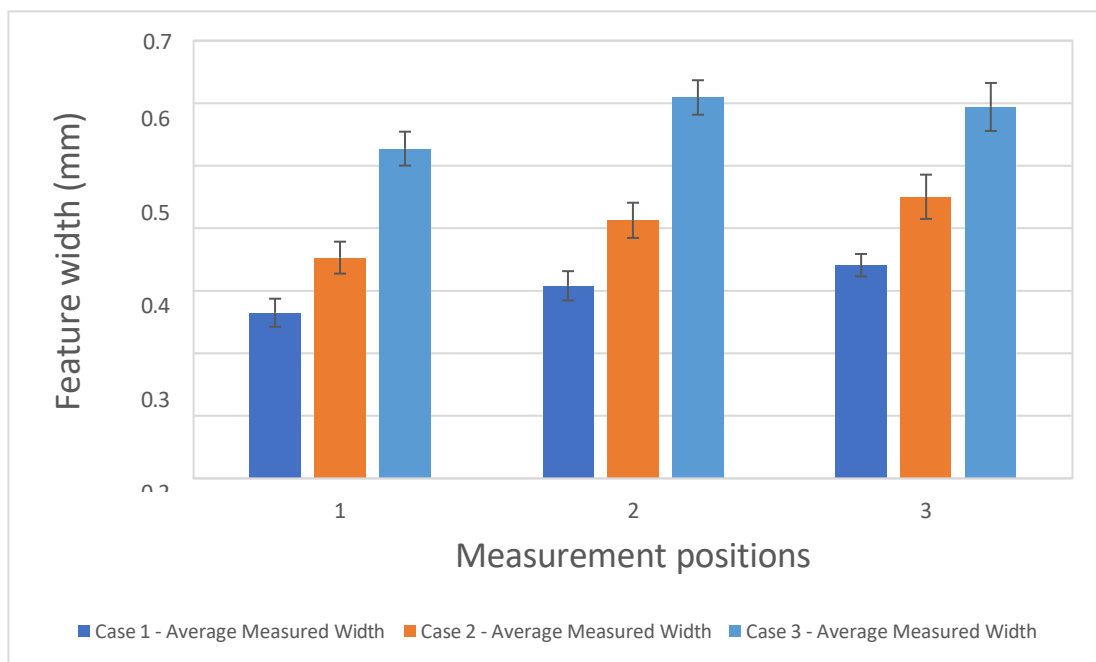


Figure 4. 20: Graphical representation of average measured width and standard deviations for Sample 1 (1 Front).

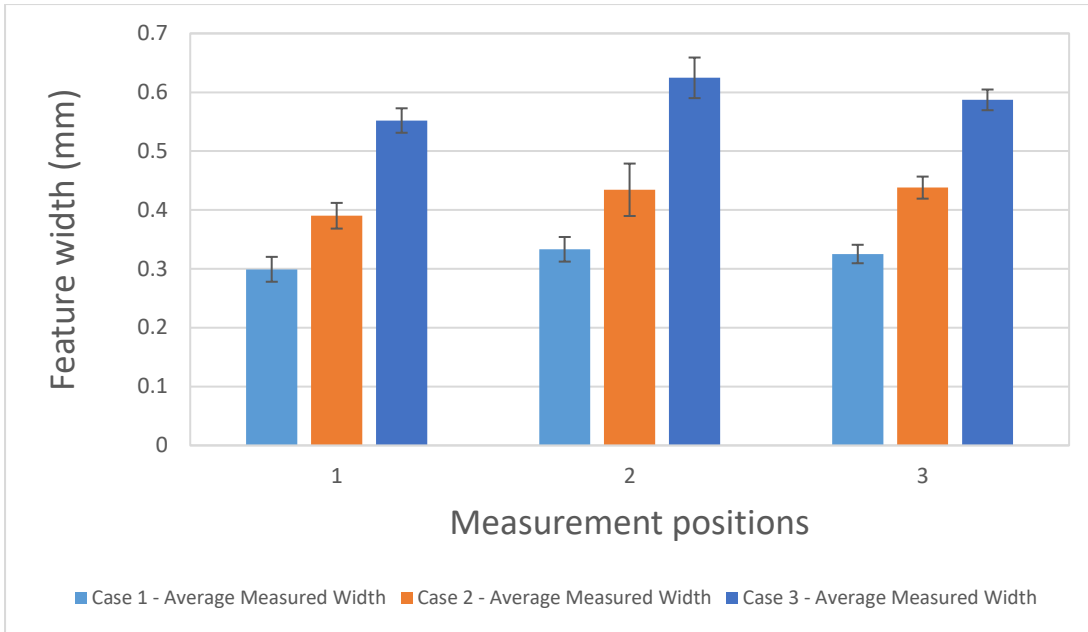


Figure 4. 21: Graphical representation of average measured width and standard deviations for Sample 2

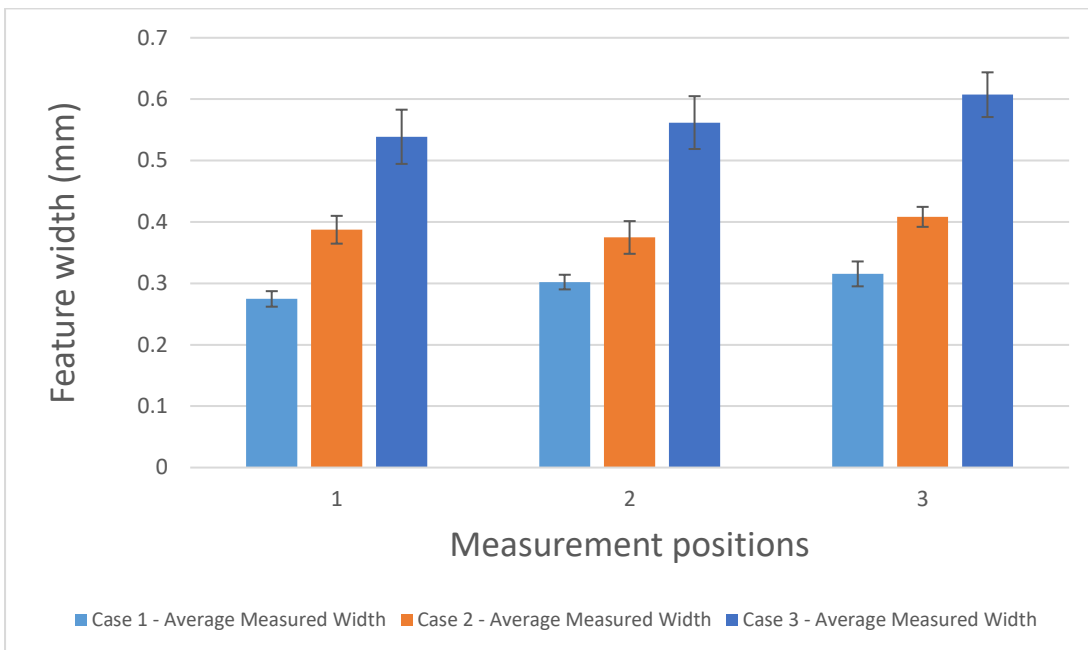


Figure 4. 22: Graphical representation of average measured width and standard deviations for Sample 3.

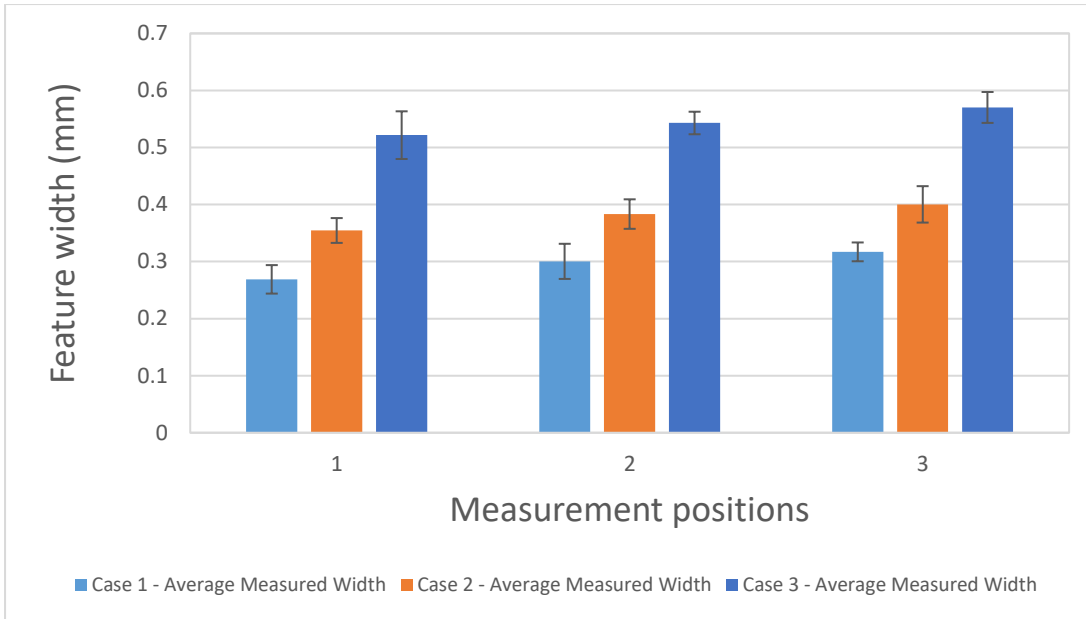


Figure 4. 23: Graphical representation of average measured width and standard deviations for Sample 4.

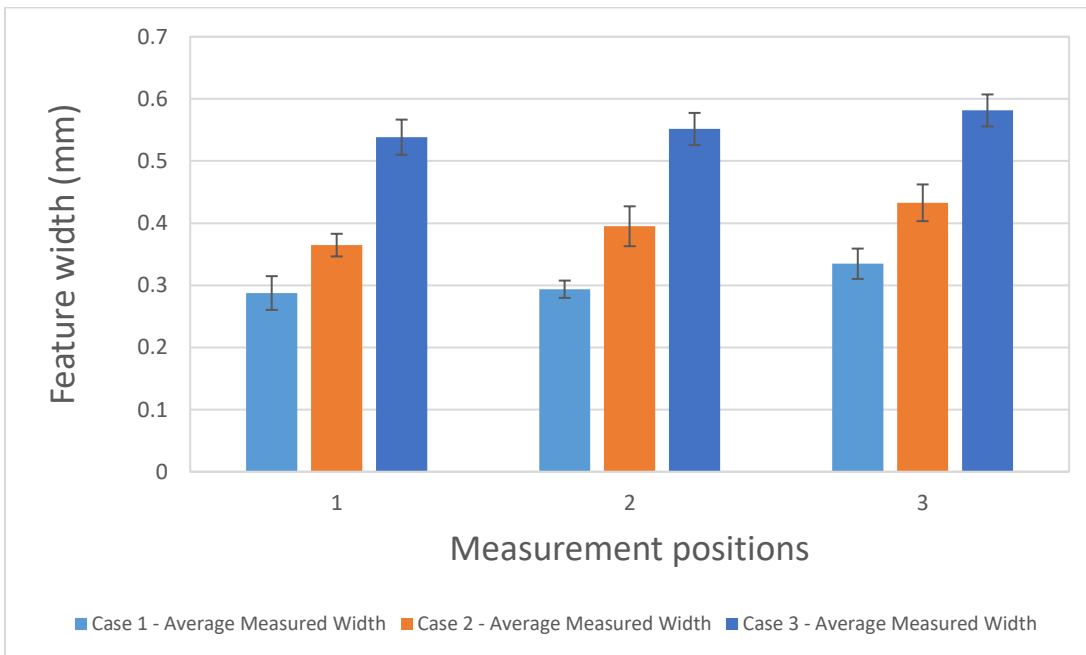


Figure 4. 24: Graphical representation of average measured width and standard deviations for Sample 5.

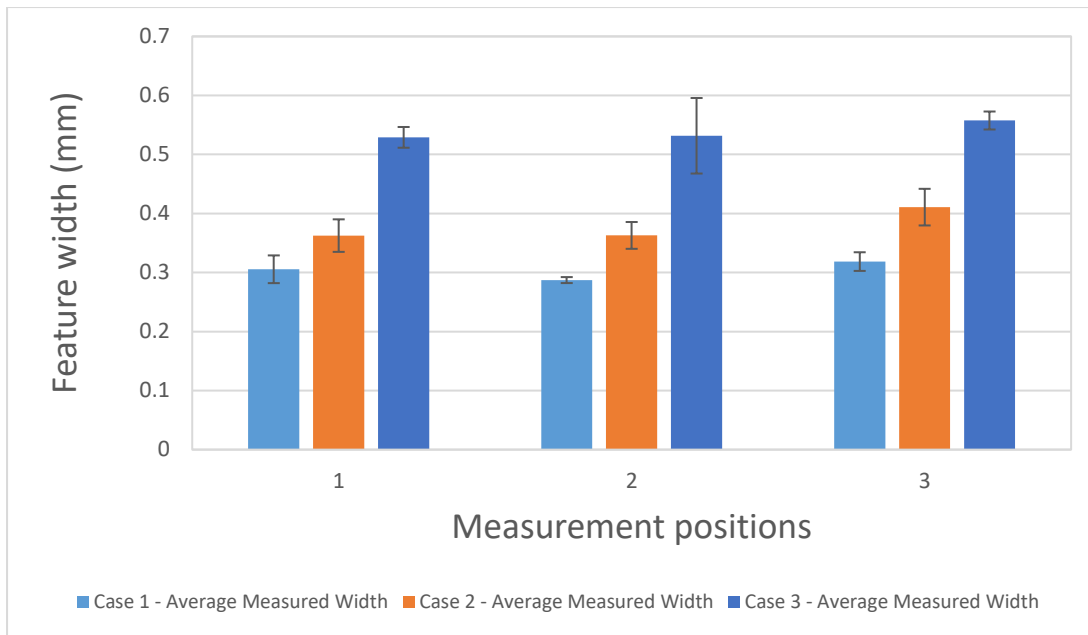


Figure 4. 25: Graphical representation of average measured width and standard deviations for Sample 6.

4.7.2.1 Positional Variation in Feature Width (PWM)

The positional variation of feature width was compared for samples built with the same parameters but at different locations on the build platform. Similar to section 4.5.2.1, this exercise is aimed at analysing the influence of build position on the accuracy of the feature widths. A summary of the percentage differences in measured widths for Case 1, 2 and 3 are shown in Table 4. 18 and Table 4. 20.

Sample 1 and Sample 2 were built with the same build parameters (Strategy X, refer to Table 4. 17) with the main variation being the position on the build plate. The observed difference in measured width ranged from 1.16% (H3, Case 2) to 12.96% (H1 case 1). By percentage, 66% of sample 2 features were bigger than sample 1 features widths. On the other hand, sample 3 features were about 78% larger than sample 4 features (Table 4. 19) with a range of 0.53% (H3 case 1) and 8.46% (H1, case 2).

Table 4. 18: Percentage Difference in Measured width for Case 1, 2 and 3 features with Sample 1 as reference (Sample 1- Sample 2).

Case	Height	Difference in Measured Width (%)
1	H1	-12.96
	H2	-8.19
	H3	4.63
2	H1	-10.54
	H2	-5.25
	H3	2.74
3	H1	-4.68
	H2	-2.54
	H3	1.16

Table 4. 19: Percentage Difference in Measured width for Case 1, 2 and 3 features with Sample 3 as reference (Sample 3- Sample 4).

Case	Height	Difference in Measured Width (%)
1	H1	2.10
	H2	0.55
	H3	-0.53
2	H1	8.46
	H2	-2.28
	H3	1.96
3	H1	3.18
	H2	3.36
	H3	6.11

Table 4. 20: Percentage Difference in Measured width for Case 1, 2 and 3 features with Sample 5 as reference (Sample 5- Sample 6).

Case	Height	Difference in Measured Width (%)
1	H1	-6.26
	H2	2.19
	H3	4.81
2	H1	0.58
	H2	8.13
	H3	5.08

Case	Height	Difference in Measured Width (%)
3	H1	1.73
	H2	3.61
	H3	4.11

For samples 5 and 6, 89% of the features were larger in sample 5 compared to sample 6, ranging from 0.58% (H1, case 2) to 8.13% (H2, Case 2).

Overall, sample 5 and 6 have minimum percentage variation hence highest geometrical precision compared to sample pairs 1-2 and pairs 3-4. Previous experimental results presented in section 4.5 (SLM280 machine) showed that samples 5 and 6, manufactured in the centre of the build platform had the highest geometrical precision. For this experiment with PWM laser and AM250 machine (SS316L material), samples 5 and 6 were positioned at the top right of the build platform (Figure 4. 19). The build position has an influence on the geometrical precision, however, the reason for this variation cannot be deduced from this result since it was not the initial objective of the experiment.

4.7.3 Model Prediction using coefficients optimised to all LPBF continuous laser data.

The original model (without optimised coefficients) was used to predict the feature widths for case 1-3 for PWM laser. From Table 4. 21, the MPE from the original model ranged from 9.20% (Sample 5, Case 2, H2) to 47.30% (Sample 1, Case 1, H3). This was considered as a significantly high range in MPE hence the next step was to apply the optimised coefficients based on the Continuous Laser data to theoretically estimate the feature width.

This was done to determine the transferability of the coefficients derived from the SLM280 machine and AlSi7Mg material would be transferable to PWM AM250 machine and SS216L material. The results show that overall, the optimised model based on continuous laser data did not improve the MPE but rather increased it to a range of 39.54% (Sample 3, Case 2, H1) to 79.90% (Sample 2, Case 2, H1) This demonstrates that the use of coefficients optimised for a particular machine and material combination may not be transferrable to another machine and material combination. In section 4.7.4, machine specific coefficients will be tuned and compared with the original model.

Table 4. 21: Mean percentage errors (MPE) and standard deviations (SD) for the original verses optimised model based on Continuous Laser.

Sample Number	CASE	Height	Original model		Optimised model	
			MPE	SD	MPE	SD
1	Case 1	H1	31.91%	5.27%	77.50%	13.73%
		H2	41.46%	4.76%	60.88%	13.09%
		H3	47.30%	2.83%	52.27%	8.17%
	Case 2	H1	17.64%	6.04%	79.90%	13.19%
		H2	29.59%	4.84%	59.96%	10.99%
		H3	35.42%	4.63%	52.37%	10.92%
	Case 3	H1	20.27%	4.00%	67.97%	8.43%
		H2	31.02%	2.94%	49.49%	6.37%
		H3	29.10%	4.67%	57.94%	10.41%
2	Case 1	H1	39.80%	4.41%	56.92%	11.49%
		H2	46.03%	3.18%	48.33%	8.74%
		H3	44.78%	2.56%	59.57%	7.40%
	Case 2	H1	25.66%	4.23%	62.39%	9.24%
		H2	32.82%	5.96%	52.63%	13.32%
		H3	33.86%	2.79%	56.07%	6.59%
	Case 3	H1	23.92%	2.99%	60.29%	6.30%
		H2	32.65%	3.78%	45.97%	8.19%
		H3	28.51%	2.13%	59.25%	4.74%

Sample Number	CASE	Height	Original model		Optimised model	
			MPE	SD	MPE	SD
3	Case 1	H1	37.63%	2.97%	50.62%	7.18%
		H2	43.33%	2.28%	45.26%	5.83%
		H3	45.59%	3.52%	47.54%	9.53%
	Case 2	H1	29.81%	4.12%	39.54%	8.19%
		H2	31.36%	4.06%	42.89%	8.45%
		H3	33.54%	2.65%	44.55%	5.77%
	Case 3	H1	27.15%	5.60%	51.23%	11.61%
		H2	30.17%	5.44%	49.50%	11.65%
		H3	35.54%	3.99%	42.19%	8.80%
4	Case 1	H1	35.87%	6.13%	54.88%	14.81%
		H2	42.46%	6.30%	47.48%	16.15%
		H3	45.95%	2.81%	46.55%	7.61%
	Case 2	H1	23.31%	4.54%	52.47%	9.02%
		H2	28.99%	4.99%	47.82%	10.39%
		H3	31.88%	5.61%	48.18%	12.19%
	Case 3	H1	24.71%	6.46%	56.28%	13.41%
		H2	28.07%	2.68%	53.99%	5.75%
		H3	31.43%	3.44%	51.24%	7.58%
5	Case 1	H1	42.90%	5.28%	55.28%	14.36%
		H2	44.45%	2.65%	59.72%	7.61%
		H3	51.11%	3.54%	48.19%	10.73%
	Case 2	H1	9.20%	9.15%	61.61%	8.20%
		H2	35.56%	5.58%	56.33%	13.54%
		H3	41.33%	3.91%	48.21%	9.88%
	Case 3	H1	16.52%	4.18%	65.11%	8.26%
		H2	18.56%	3.91%	65.69%	7.95%
		H3	22.75%	3.74%	61.53%	7.82%

Sample Number	CASE	Height	Original model		Optimised model	
			MPE	SD	MPE	SD
6	Case 1	H1	46.41%	4.28%	45.76%	11.63%
		H2	43.32%	1.01%	62.99%	2.91%
		H3	48.78%	2.56%	55.25%	7.77%
	Case 2	H1	29.85%	5.74%	63.15%	13.35%
		H2	30.07%	4.52%	69.66%	10.96%
		H3	38.11%	4.76%	56.35%	12.03%
	Case 3	H1	15.18%	2.82%	67.77%	5.57%
		H2	14.65%	8.82%	73.65%	17.95%
		H3	19.55%	2.21%	68.21%	4.63%

4.7.4 Model prediction with coefficients optimised with all LPBF PWM laser data.

The MPE and standard deviations for both the original and optimised model are recorded in Table 4. 22. For each sample, the values in red and green indicate the maximum and minimum average percentage error(s) respectively. For samples 1-6, the MPE for the original model ranged from 45-51%. This decreased significantly after parametric optimisation to a range of 9-15%, indicating an improvement in prediction accuracy of the optimised model when tuned to the data from all PWM samples.

From Figure 4. 26 and Figure 4. 27, the vertical axis of the graphs shows the average error for each case at a given height H1, H2 and H3. The horizontal axis represents the build cases and build heights for samples 1-6. A total of 54 bars were plotted together with respective standard deviations. The standard deviations for the original model (Figure 4. 26) are relatively smaller compared to the optimised model (Figure 4. 27). However, there are significant improvements in the MPE after model optimisation Table 3-23.

From Table 3-24, the following observations were made:

- The Power parameter was optimised by the coefficient 1.359, implying that the effect of power in the original model was underestimated by approximately 36%.
- The build parameter, Speed was optimised by the coefficient 0.6212. This suggests an overestimation of the impact of speed by 32% in the original model.
- The coefficient of hatch spacing parameter was optimised by the coefficient 0.968. Compared to speed and power with a significant over or underestimation, the impact of hatch spacing is slightly overestimated by 3.2%.
- Finally, the layer height parameter was optimised by the coefficient 0.025. This suggest that the layer height has minimal influence on the feature width estimation.

In summary, in the case of PWM laser experimental results optimisation, power, speed and hatch spacing coefficient were significant (Table 4. 23). However, the height coefficient of 0.025 accounts for only 0.8-1.7% of the predicted width for a design feature height of 0.2mm compared with the continuous laser optimisation, which accounted for 4-10% of the predicted width for a design feature height of 0.3mm. This difference in the significance of layer height may be because the double laser scan on the slicing data was absent for PWM but present for Continuous laser hence needed to be accounted for by the height coefficient in the latter manufacturing technique. This demonstrated the capability of the model tuning approach to adapt to a machine CAM specificity.

As mentioned before these good results could be due to overfitting, so once again it is proposed to perform an optimisation using only one sample.

Table 4. 22: Mean percentage errors (MPE) and standard deviations (SD) for the original verses optimised model.

Sample Number	CASE	Height	Original Model		Optimised Model	
			MPE	SD	MPE	SD
1	Case 1	H1	31.91%	5.27%	12.22%	5.55%
		H2	41.46%	4.76%	6.61%	6.05%
		H3	47.30%	2.83%	4.76%	8.17%
	Case 2	H1	17.64%	6.04%	13.03%	8.29%
		H2	29.59%	4.84%	6.49%	3.95%
		H3	35.42%	4.63%	4.97%	5.16%
	Case 3	H1	20.27%	4.00%	4.42%	2.87%
		H2	31.02%	2.94%	8.13%	3.92%
		H3	29.10%	4.67%	5.64%	3.48%

Sample Number	CASE	Height	Original Model		Optimised Model	
			MPE	SD	MPE	SD
2	Case 1	H1	39.80%	4.41%	6.84%	3.19%
		H2	46.03%	3.18%	5.65%	4.85%
		H3	44.78%	2.56%	6.22%	3.34%
	Case 2	H1	25.66%	4.23%	4.99%	3.60%
		H2	32.82%	5.96%	5.96%	6.44%
		H3	33.86%	2.79%	4.26%	2.48%
	Case 3	H1	23.92%	2.99%	4.65%	1.88%
		H2	32.65%	3.78%	10.30%	5.04%
		H3	28.51%	2.13%	2.45%	1.73%
3	Case 1	H1	37.63%	2.97%	3.75%	3.41%
		H2	43.33%	2.28%	3.26%	2.47%
		H3	45.59%	3.52%	6.59%	4.93%
	Case 2	H1	29.81%	4.12%	4.95%	4.01%
		H2	31.36%	4.06%	5.34%	3.08%
		H3	33.54%	2.65%	4.76%	3.77%
	Case 3	H1	27.15%	5.60%	7.87%	5.75%
		H2	30.17%	5.44%	8.14%	4.76%
		H3	35.54%	3.99%	9.63%	4.42%

Sample Number	CASE	Height	Original Model		Optimised Model	
			MPE	SD	MPE	SD
4	Case 1	H1	35.87%	6.13%	7.68%	7.73%
		H2	42.46%	6.30%	8.76%	7.29%
		H3	45.95%	2.81%	5.72%	3.50%
	Case 2	H1	23.31%	4.54%	7.59%	4.43%
		H2	28.99%	4.99%	6.69%	5.82%
		H3	31.88%	5.61%	8.52%	7.37%
	Case 3	H1	24.71%	6.46%	7.12%	5.48%
		H2	28.07%	2.68%	4.24%	2.18%
		H3	31.43%	3.44%	5.07%	2.83%
5	Case 1	H1	42.90%	5.28%	9.00%	6.15%
		H2	44.45%	2.65%	4.11%	2.43%
		H3	51.11%	3.54%	6.75%	5.04%
	Case 2	H1	9.20%	9.15%	4.67%	3.30%
		H2	35.56%	5.58%	7.91%	4.41%
		H3	41.33%	3.91%	6.73%	5.73%
	Case 3	H1	16.52%	4.18%	7.08%	2.52%
		H2	18.56%	3.91%	7.39%	5.15%
		H3	22.75%	3.74%	6.22%	5.14%

Sample Number	CASE	Height	Original Model		Optimised Model	
			MPE	SD	MPE	SD
6	Case 1	H1	46.41%	4.28%	12.81%	6.16%
		H2	43.32%	1.01%	1.62%	1.71%
		H3	48.78%	2.56%	3.58%	3.49%
	Case 2	H1	29.85%	5.74%	7.44%	3.59%
		H2	30.07%	4.52%	6.57%	5.00%
		H3	38.11%	4.76%	7.43%	2.00%
	Case 3	H1	15.18%	2.82%	7.04%	3.56%
		H2	14.65%	8.82%	15.79%	6.59%
		H3	19.55%	2.21%	10.62%	3.05%

Table 4. 23: Summary of Process parameters and coefficients from tuned model to all data from samples 1-6

Process Parameter	Power	Speed	Hatch Spacing	Layer height
Coefficient (3dp)	1.359	0.6212	0.968	0.025

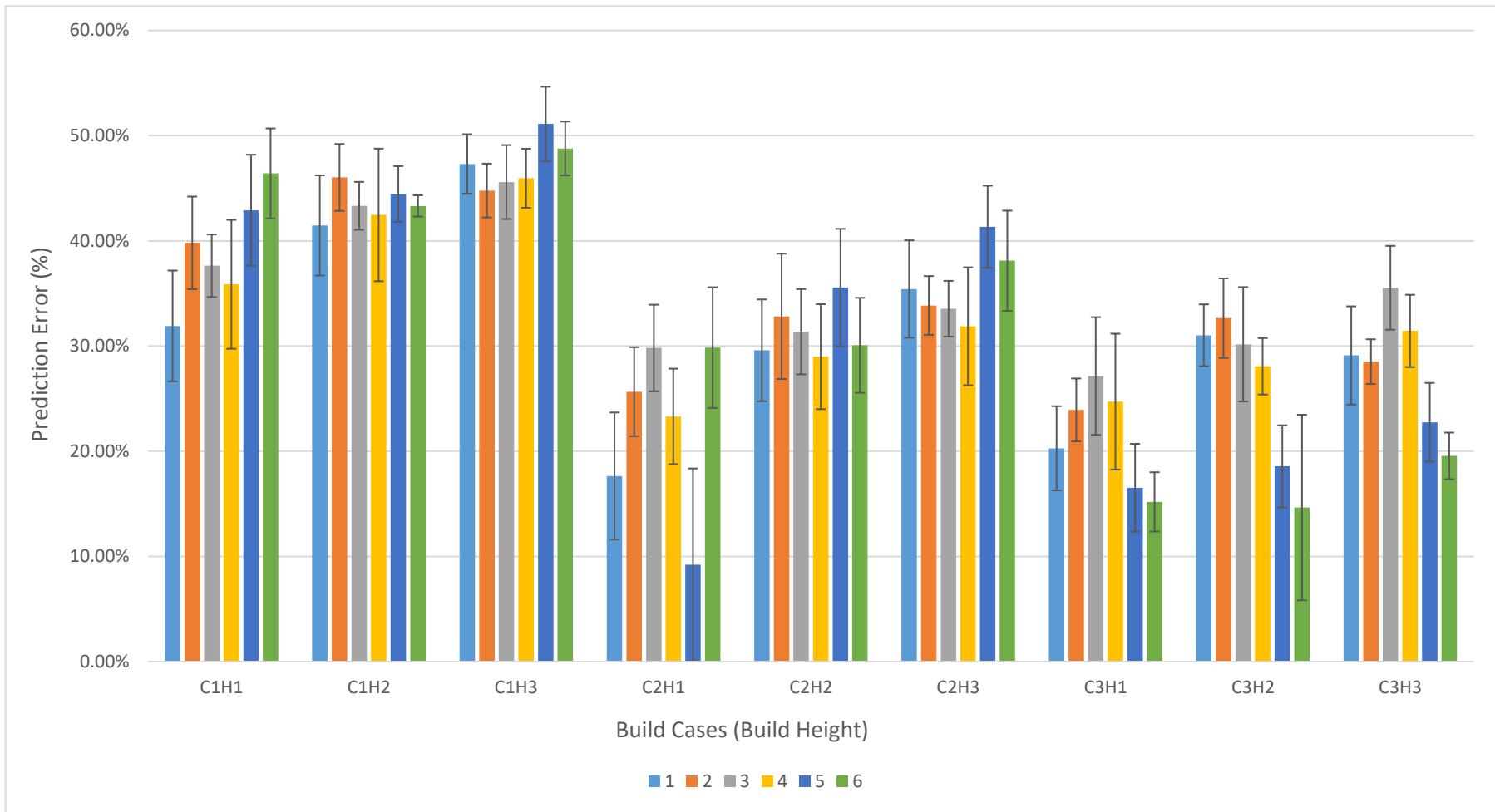


Figure 4. 26: Plot of MPE for original model of Samples 1-6. Where C1, C2, C3 represent Case 1, Case2, Case 3.

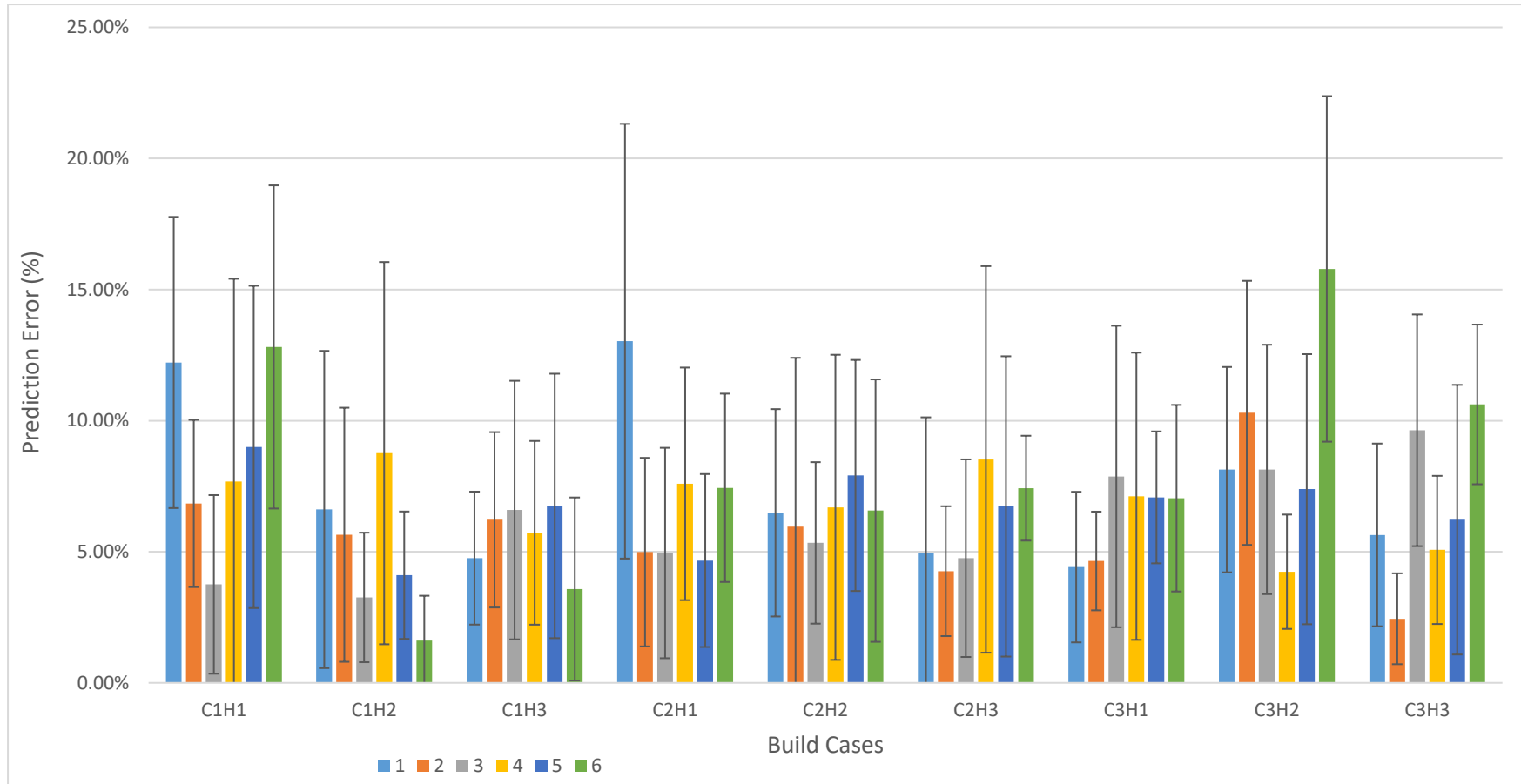


Figure 4. 27: Plot of MPE for optimised model of Samples 1-6 (PWM laser). Where C1, C2, C3 represent Case 1, Case2, Case 3.

4.7.5 Model coefficients optimised with data from one LPBF pulse laser sample.

Similar to section 4.6.3, the data from sample 1 was used to optimise all the theoretically predicted widths. The results show good MPE for single sample optimisation (1.9-13.7%) compared to optimisation to all six-sample data (1.6-13.03%). This indicates that the updated model can be used for either a continuous or PWM laser however, the coefficients of the process parameters power, speed, hatch spacing, and layer height will be machine specific. A comparison of the MPE for the optimisation based on all sample data to sample 1 data is shown in Table 4. 25.

The following observations were made from the results in Table 4. 24.

- The Power parameter was optimised by the coefficient 1.195. This suggests an underestimation of the impact of speed by approximately 19.5% in the original model.
- The coefficient of the Speed parameter was optimised by the 0.797, meaning that the effect of speed in the original model was overestimated by approximately 21%.
- Also, the hatch spacing parameter was optimised by the coefficient by 1.121. This suggests an underestimation of the impact of hatch spacing of approximately 12.1% in the original model.
- The layer height parameter was optimised by the coefficient 0.039. This suggest that the layer height has minimal influence on the feature width. The parameter effect was overestimated by 96.1%.

The general trend for the coefficients of power, speed, hatch spacing, and layer height are in the same direction for optimisation with a single sample data compared to all sample data however the magnitudes of the coefficients differ.

Table 4. 24: Summary of Process parameters and coefficients from tuned model to sample 1 data

Process Parameter	Power	Speed	Hatch Spacing	Layer height
Coefficient (2dp)	1.195	0.797	1.121	0.039

Table 4. 25: Comparison between average percentage error using all sample data to sample 1 data.

Sample Number	CASE	ALL DATA OPTIMISATION		SAMPLE 1 OPTIMISATION	
		Mean Percentage Error (MPE)	Standard Deviation	Mean Percentage Error (MPE)	Standard Deviation
1	Case 1	12.22%	5.55%	7.85%	3.09%
		6.61%	6.05%	6.27%	2.66%
		4.76%	8.17%	3.96%	2.17%
	Case 2	13.03%	8.29%	7.51%	3.28%
		6.49%	3.95%	5.87%	4.50%
		4.97%	5.16%	13.71%	12.11%
	Case 3	4.42%	2.87%	6.79%	6.94%
		8.13%	3.92%	5.18%	4.58%
		5.64%	3.48%	5.78%	3.03%

Sample Number	CASE	ALL DATA OPTIMISATION		SAMPLE 1 OPTIMISATION	
		Mean Percentage Error (MPE)	Standard Deviation	Mean Percentage Error (MPE)	Standard Deviation
2	Case 1	6.84%	3.19%	3.64%	2.82%
		5.65%	4.85%	5.89%	3.44%
		6.22%	3.34%	4.43%	2.00%
	Case 2	4.99%	3.60%	4.51%	2.06%
		5.96%	6.44%	4.67%	2.91%
		4.26%	2.48%	6.14%	1.99%
	Case 3	4.65%	1.88%	6.95%	5.86%
		10.30%	5.04%	5.40%	3.83%
		2.45%	1.73%	7.31%	4.66%
3	Case 1	3.75%	3.41%	4.67%	2.91%
		3.26%	2.47%	5.87%	4.62%
		6.59%	4.93%	7.85%	3.70%
	Case 2	4.95%	4.01%	11.35%	5.06%
		5.34%	3.08%	5.61%	4.71%
		4.76%	3.77%	5.03%	3.49%
	Case 3	7.87%	5.75%	3.66%	2.14%
		8.14%	4.76%	6.41%	3.56%
		9.63%	4.42%	2.11%	0.91%

Sample Number	CASE	ALL DATA OPTIMISATION		SAMPLE 1 OPTIMISATION	
		Mean Percentage Error(MPE)	Standard Deviation	Mean Percentage Error (MPE)	Standard Deviation
4	Case 1	7.68%	7.73%	2.47%	0.88%
		8.76%	7.29%	4.25%	4.19%
		5.72%	3.50%	8.28%	2.85%
	Case 2	7.59%	4.43%	6.37%	4.32%
		6.69%	5.82%	6.04%	4.44%
		8.52%	7.37%	4.76%	2.69%
	Case 3	7.12%	5.48%	5.27%	3.26%
		4.24%	2.18%	7.14%	3.05%
		5.07%	2.83%	4.19%	2.96%
5	Case 1	9.00%	6.15%	13.19%	5.16%
		4.11%	2.43%	11.16%	6.08%
		6.75%	5.04%	7.57%	3.28%
	Case 2	4.67%	3.30%	5.08%	2.56%
		7.91%	4.41%	5.40%	4.05%
		6.73%	5.73%	3.22%	3.21%
	Case 3	7.08%	2.52%	2.17%	1.15%
		7.39%	5.15%	1.90%	1.53%
		6.22%	5.14%	1.95%	2.02%

Sample Number	CASE	ALL DATA OPTIMISATION		SAMPLE 1 OPTIMISATION	
		Mean Percentage Error(MPE)	Standard Deviation	Mean Percentage Error(MPE)	Standard Deviation
6	Case 1	12.81%	6.16%	8.59%	3.94%
		1.62%	1.71%	10.60%	6.28%
		3.58%	3.49%	12.62%	8.23%
	Case 2	7.44%	3.59%	4.65%	2.68%
		6.57%	5.00%	5.59%	3.37%
		7.43%	2.00%	6.11%	4.03%
	Case 3	7.04%	3.56%	3.87%	3.16%
		15.79%	6.59%	4.03%	2.26%
		10.62%	3.05%	3.03%	0.89%

4.8 Discussion

In this Chapter, it was assumed that the Rosenthal equation can be used to accurately predict the melt-pool width in the forming direction hence sufficiently determine the minimum feature width for Case 1 (single scan), Case 2 (double scan) and Case 3 (contouring with infill) scenarios. To test this theory, six samples were manufactured in AlSi7Mg on the SLM280 machine. The experimental data from the test pieces were compared with the theoretical calculated width, however, in the first instance the results suggested that the original model underpredicted the feature width considerably particularly for Case 1 scenario.

A comparison between theoretical predicted width (based on Rosenthal equation) and manufactured single bead width was compiled by Tang, et al., (2017). Compared to experimental results, they reported that the Rosenthal equation predicts the experimental single bead width by within 5-10% prediction error. This result differed from the original experimentation conducted in the chapter. It was suspected that the effect of the process parameters Power, Speed, Hatch spacing, and perhaps Layer height were not being fully considered by the original model hence the next logical step was to attempt to optimise the process parameters using L-BFGS optimisation algorithm.

After L-BFGS optimisation of Power, Speed, Hatch Spacing and Layer height, first by tuning to all data from samples 1-6 and then tuning to data from sample 1 only. The L-BFGS Algorithm reduced the maximum prediction error by 20-28% for continuous laser and 35-37% for PWM laser, significant improvements in the prediction accuracy.

The new coefficients obtained as summarised in Table 4. 26. From the table, the general trend was as follows:

The optimised coefficient of power was always greater than one regardless of the laser type or material used. This suggests that the effect of power was always underestimated in the case of AlSi7Mg material and SS316L. A possible explanation for the increase in the influence of power could be the laser absorptivity parameter. The absorptivity is a material thermo-physical property which was experimentally derived from published literature by Tang, et al., (2017). In the published literature, the

absorptivity for AlSi10Mg ranged from 0.32 to 0.39 therefore an average of 0.33 was used for calculating the melt-pool width. Since the laser power used for the experimentation in AlSi7Mg was higher than 360W (from published literature), this implies that the absorptivity will increase. The extra average of 30% power compensation seems logical.

For speed, the optimised coefficient was always less than one for both AlSi7Mg and SS316L. This means that the effect of speed was overestimated for both machine and material combinations. Since the analytical calculation of the melt-pool width is inversely proportional to the square root of the speed, a reduction in the influence of speed results in larger melt-pool widths than previously predicted.

Also, the optimised coefficient of hatch spacing was higher for PWM laser compared to Continuous Laser. Difference in hatch spacing will impact the melt-pool size. All things being equal, an increase in the hatch spacing will increase the melt-pool width for case 2 and case 3 scenario. For continuous laser, the low influence of hatch spacing may be because the laser provides continuous power and speed along each scan hence only the hatch spacing between adjacent melt-pools needs to be compensated for. On the other hand, PWM laser has the pulse overlap factor in addition to hatch spacing. The pulse overlap defines the relationship between adjacent pulses along the same scanning direction while the hatch spacing relates to adjacent scan tracks. This additional pulse overlap parameter for PWM could be a possible explanation for the higher coefficient of hatch spacing required for PWM laser compared to Continuous laser.

Finally, the coefficient of layer height is always less than 0.1 for both PWM and Continuous Laser. Therefore, the height parameter has no significant effect on the melt-pool width and does not need to be considered in theoretical width predictions.

Table 4. 26: Summary of coefficients from L-BFGS optimisation algorithm

Laser Type	Tuning Data	Coefficients			
		Power	Speed	Hatch Spacing	Layer Height
C.L (AISI7Mg)	Samples 1-6	1.360	0.683	0.266	0.10
PWM (SS316L)		1.359	0.6212	0.968	0.03
C.L (AISI7Mg)	Sample 1	1.383	0.598	0.182	0.01
PWM (SS316L)		1.195	0.797	1.121	0.04

4.9 Conclusion

This chapter has presented the development, optimisation, and validation of an analytical model to determine the minimum feature width of machine/material combination.

In summary,

- It was decided that the Rosenthal equation was suitable for estimating the melt-pool width since the intention was to manufacture samples within the range of ideal energy input.
- The input data required by the model are the power, speed, hatch spacing, layer height and material properties such as laser absorptivity, specific heat capacity, density, melting and ambient temperature. These parameters are specific for a given material and machine combination.
- After initial experimentation on AlSi7Mg and SLM280 machine, the original theoretical model under predicts the feature widths particularly for Case 1 scenario. The generally high trend in prediction error suggested the need to tune the model for higher accuracy.
- The L-BFGS optimisation algorithm was used to tune the original model, initially with all the data from six samples and subsequently from only one sample. The improvement in percentage prediction accuracy after the optimisation process was promising.
- The parametric based model has been optimised and a single sample can be used to predict the minimum feature width for AlSi7Mg (SLM280) material (machine) combination.
- The optimisation technique was validated with SS316L material and AM250 machine. Again, the optimisation algorithm successfully improved the prediction accuracy significantly.
- The overall results indicates that the new model is applicable for either a continuous or PWM laser hence can be generalised for any LPBF machine and material combination however, the coefficients of the process parameters power, speed, hatch spacing, and layer height will be specific to a given machine and material combination.

- With an MPE of up to 15% based on variations in build position, future work could be towards the design of a model, which can be tuned to consider the position on the build platform.
- In future work, investigation on impact of build position on geometric precision and accuracy will be useful for understanding the causes variations based on build position and find ways to account for them in the prediction model.

5 Assessment of Minimum Spacing between Features produced by LPBF.

5.1 Geometric Characteristics of Textures

Typically, textures consist of regularly or irregularly feature pattern, with each feature located at a specific distance from an adjacent one (Armillotta, 2006). Figure 5. 1 shows examples of typical textures, which are applicable for visible aircraft interiors. From Figure 5. 1, the textures consist of features of defined widths and spacing. In Chapter 4, an analytical method was developed for predicting the minimum feature size which can realistically be used to create a texture manufactured using LPBF, for a given machine and material combination. To create textures, therefore, it is also necessary to evaluate the spacing between these features, and again produce a method for predicting the textures, which can be manufactured without the features merging. At present, there is a research gap for addressing how the minimum measurable spacing between two surface features can be assessed.

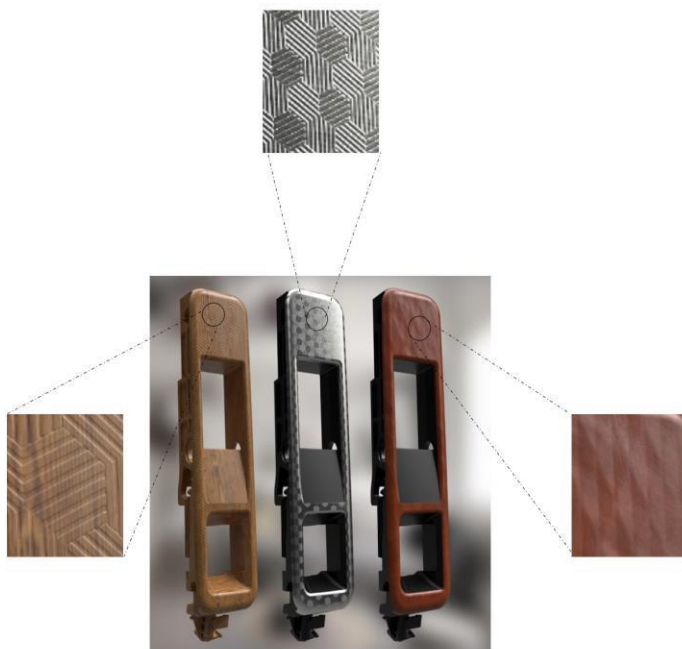


Figure 5. 1: Examples of textures which are applicable for aircraft interiors (Adobe, 2020)

5.2 Chapter's Objectives

Previously, Chapter 4 presented a theoretical parametric model for evaluating the minimum width of features produced by the LPBF process. The Rosenthal equation (Promoppatum *et al.*, 2017) was optimised for higher prediction accuracy between the experimental and theoretical feature width for a specific machine or material combination. For the creation of a texture, the design feature spacing, and design depth need to be suitable enough to resolve the manufactured spacing.

Since the visibility of a feature spacing is highly subjective (dependent on the observer's eyesight and observation position), this chapter will focus on the measurability of the texture using high resolution surface measurement techniques (objective approach) based on the assumption that the feature measurability is linked to its visibility and subsequently impacts aesthetics of the texture. Therefore, this chapter proposes an approach for determining the minimum measurable spacing between two adjacent features for a specified design feature depth.

5.3 Process Conditions for Minimum Spacing between Features

5.3.1 Sum of Squared Ratios

Most of the research in this field focuses on producing fully dense components. This theory enables engineers to determine the hatch spacing at which adjacent melt tracks merge together to create a single feature. The intention of this work is to adapt the theory to determine the point at which a measurable spacing between adjacent features can be determined. According to Tang et al (2017), full density can be achieved between two adjacent melt-pool tracks under the following condition.

$$\left(\frac{H}{W_{mp}}\right)^2 + \left(\frac{L}{D_{mp}}\right)^2 \leq 1 \quad (5.1)$$

Where H is the hatch spacing, W_{mp} is the melt-pool width, L is the layer height and D_{mp} is the melt -pool depth.

From equation 5.1, to satisfy the requirement for full melting conditions hence prevent porosity in the bulk part, the sum of squares of the ratios $\frac{H}{W_{mp}}$ and $\frac{L}{D_{mp}}$ must be less than one. A large hatch spacing will increase the sum of squares to be greater than one, which will result in a lack of fusion between the adjacent tracks. The objective of texturing is to achieve the opposite effect of equation 5.1; spacing between surface features is desirable when creating a texture to distinguish between the individual features. Equation 5.1 can be modified to predict the conditions under which a minimum spacing will be observed for a particular machine and material combination. For the remaining of this chapter, the sum of $\left(\frac{H}{W_{mp}}\right)^2$ and $\left(\frac{L}{D_{mp}}\right)^2$ will be referred to as the sum of squared ratios.

The next section of this chapter will describe the proposed analytical method for estimating minimum spacing. This is followed by an experiment to evaluate the sum of squared ratios predictions. The results from the experimentation are presented and discussed.

5.3.1.1 Predicting feature spacing limitations

For a measurable spacing, there must be a distinct separation between the adjacent melt tracks on the surface of the part. According to equation 5.1, this separation can be influenced by the following:

- Melt pool size, determined by material thermo-physical properties such as laser absorptivity, melting temperature, density, and specific heat capacity.
- Build layer height.
- Feature spacing.

From equation 5.1, complete fusion between two adjacent tracks will occur if the sum of squares is less than or equal to one, hence in theory, when the sum of squares is greater than one, spacing between two tracks should occur.

Equation 5.1 can be modified by maintaining the sum of squared ratios and changing the sign from \leq to \geq . The hatch spacing term, H, can be considered as the spacing between features (H_f), and the layer height L, can be considered as the feature height (L_f). This is illustrated in Figure 5. 2. In the figure, the features are surface peaks hence the height (L_f) is shown as the peak height. However, the feature depth is the same as the feature height for troughs.

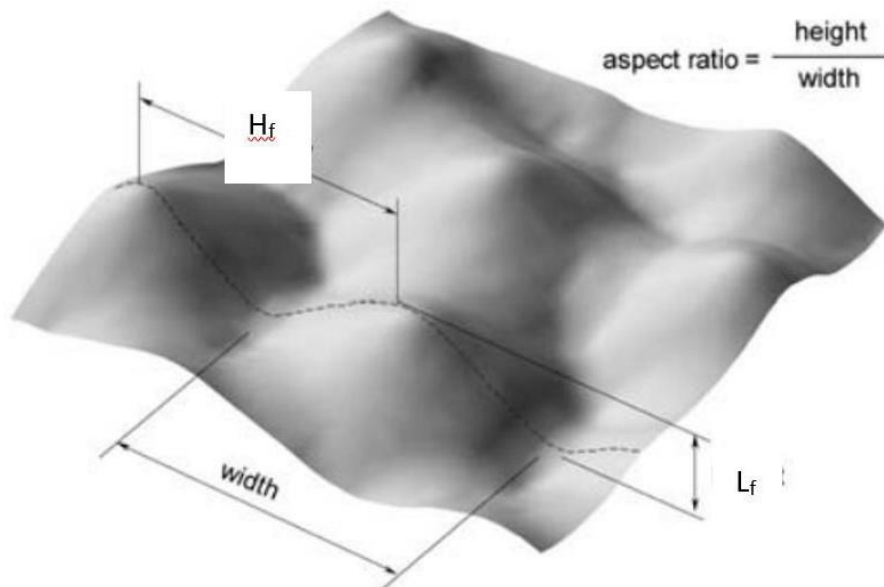


Figure 5. 2: Image showing H_f and L_f parameters (adapted from (Armillotta, 2006))

Also, the modified equation is shown in Equation 5.2.

$$\left(\frac{H_f}{W_{mp}}\right)^2 + \left(\frac{L_f}{D_{mp}}\right)^2 \geq 1 \quad (5.2)$$

Based on the assumption that W_{mp} , D_{mp} and L_f remain constant, the differences in the feature spacing, H_f , will impact the measurability of the feature spacing. It is expected that larger feature spacing will result in a more distinct gap between surface features. Likewise, larger feature height is expected to allow sufficient depth to resolve the design feature spacing compared with smaller design feature heights.

The next section of this chapter will recap on the analytical calculation and contribution of the melt-pool width and depth to the sum of squares for a specified design feature spacing.

5.3.1.2 Analytical Estimation of Melt-pool Width

The first step for determining the value of the sum of squared ratios is to calculate the melt-pool width. As described in Chapter 4, the Rosenthal equation must be modified to compensate for the effect of power and speed. For a recap, the modified Rosenthal equation for theoretical estimation of melt-pool width is shown in equation 4.13 in Chapter 4.

$$w_{theo_p} = \left(\sqrt{\frac{8}{\pi e} \cdot \frac{\lambda \cdot C_{f_p} \cdot P}{C_{f_s} \cdot \rho \cdot C_p \cdot v (T_m - T_o)}} \right) + C_{f_h} \cdot 2h_{c,i} + C_{f_{Lh}} \cdot L_h \quad (4.13)$$

5.3.1.3 Analytical Estimation of Melt-pool Depth

The melt-pool depth can be estimated when the melt-pool width is known. Figure 5. 3 (Tang et al., 2017) indicates that the melt-pool width is twice the size of the melt-pool depth. This ties with the predictions by Mirkoohi et al., (2019), where the average width/depth ratio from predicted melt pool geometries of five different samples is approximately 2 (to the nearest whole number). This is shown in Table 5. 1.

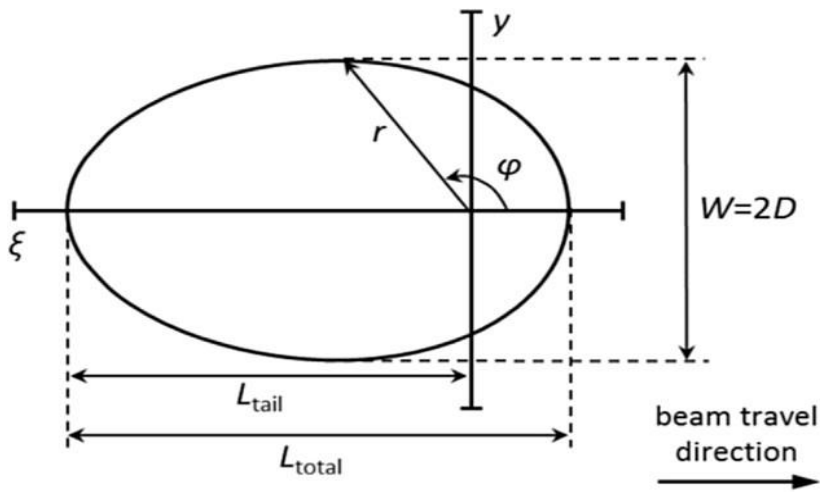


Figure 5. 3: Melt-pool schematic showing relationship between melt pool width (W) and Melt-pool Depth (D) (Tang et al., 2017)

Table 5. 1: Predicted melt-pool width to depth ratio for steady state moving point heat source for five samples (Adapted from Mirkoohi et al, 2019).

Sample	Width (μm)	Depth (μm)	Width/Depth	Average
1	44	19	2.3	2.2
2	90	33	2.7	
3	105	71	1.5	
4	145	72	2.0	
5	162	67	2.4	

Therefore, the melt-pool depth can be calculated using equation 5.4.

$$D_{mp} = \frac{W_{mp}}{2} \quad (5.4)$$

5.4 Experimentation for Feature Spacing Evaluation (PWM Laser)

Since the melt-pool width (W_{mp}) and melt-pool depth (D_{mp}) are constant for a specific material and machine parameter combination, the main variables in the sum of squares equation 5.2 are feature spacing H_f and feature height L_f .

The next stage in the development of the approach for determining the minimum measurable feature spacing is to experimentally evaluate the predictions based on the sum of squared ratios for variations in H_f and L_f .

5.4.1 Sample Design

The sample design is based on the Siemens star which is typically used to check the resolution of optical devices, printers and displays (Galovskyi *et al.*, 2013). The original Siemens star design has several spokes which meet at the centre. For a particular instrument or device, there is a certain radial distance from the centre for which the spokes of the Siemens star become illegible. This defines the lateral resolution limit (Townsend, 2018).

The centre of the Siemens star was modified with an internal circle of diameter 2.7mm (Figure 5. 4) to ensure that the smallest spoke width will be equal to the minimum feature size as determined in Chapter 3. A total of 12 spokes (Figure 5. 5) and spacing were designed with each triangular design spacing at an angle of 15 degrees at the centre (Figure 5. 7). The general dimensions are shown in Figure 5. 6. A summary of the overall geometry design parameters is shown in Table 5. 2.

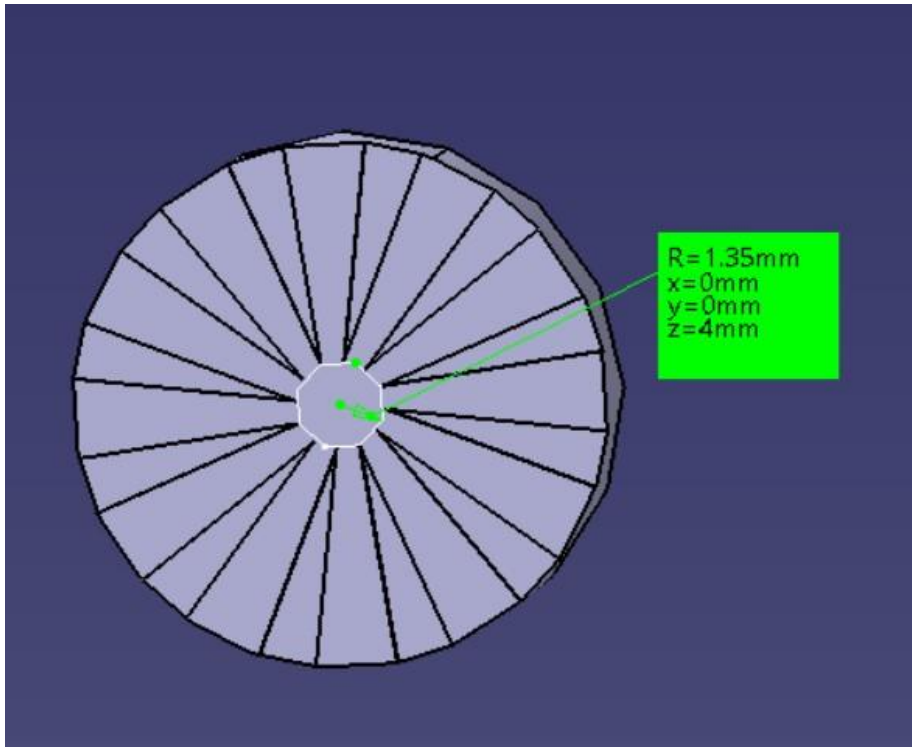


Figure 5. 4: CAD Front view showing inner circle with radius 1.35mm (2.7mm diameter)

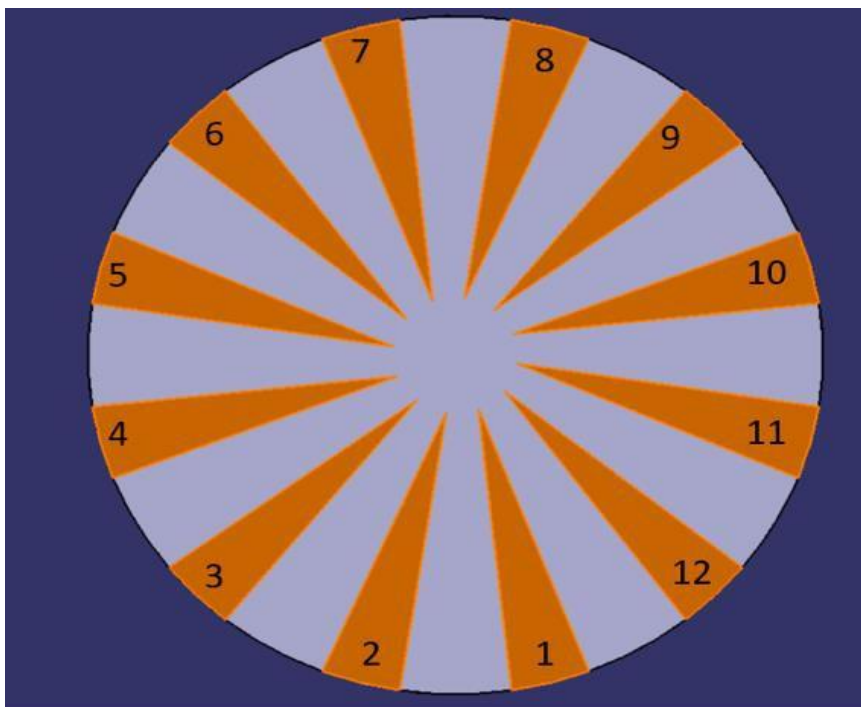


Figure 5. 5: Modified Siemens star with a total of 12 spacing (orange) and 12 spokes (grey)

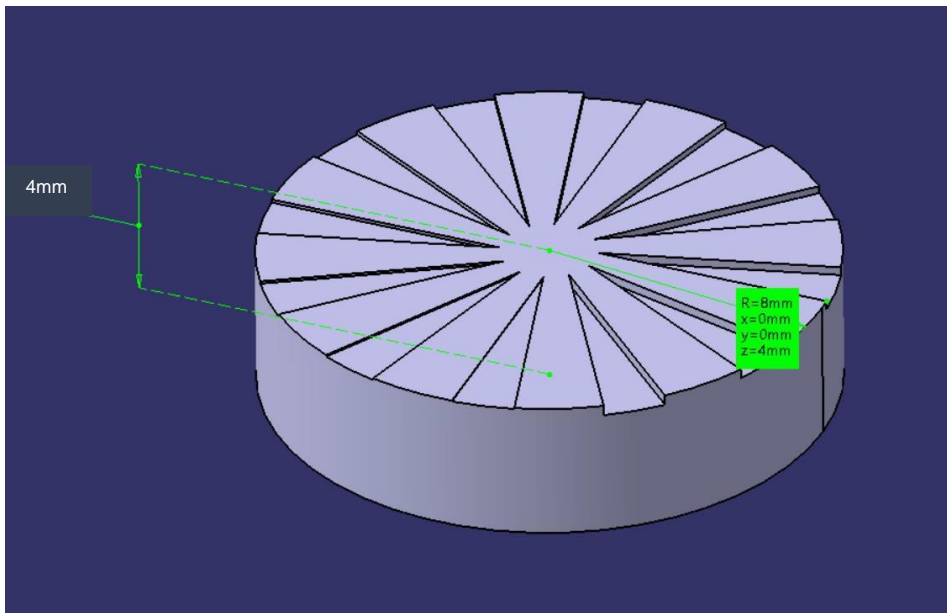


Figure 5. 6: CAD Isometric view of modified Siemens Star with thickness of 4mm and external radius of 8mm.

Table 5. 2: Parameters of Siemens star

Diameter	8mm
Number of Segments	24
Depth of Segments	25 μ m- 300 μ m
Overall Depth	4mm

In addition, the design feature height, L_f , was varied from 25 μ m to 300 μ m in increments of 25 μ m.

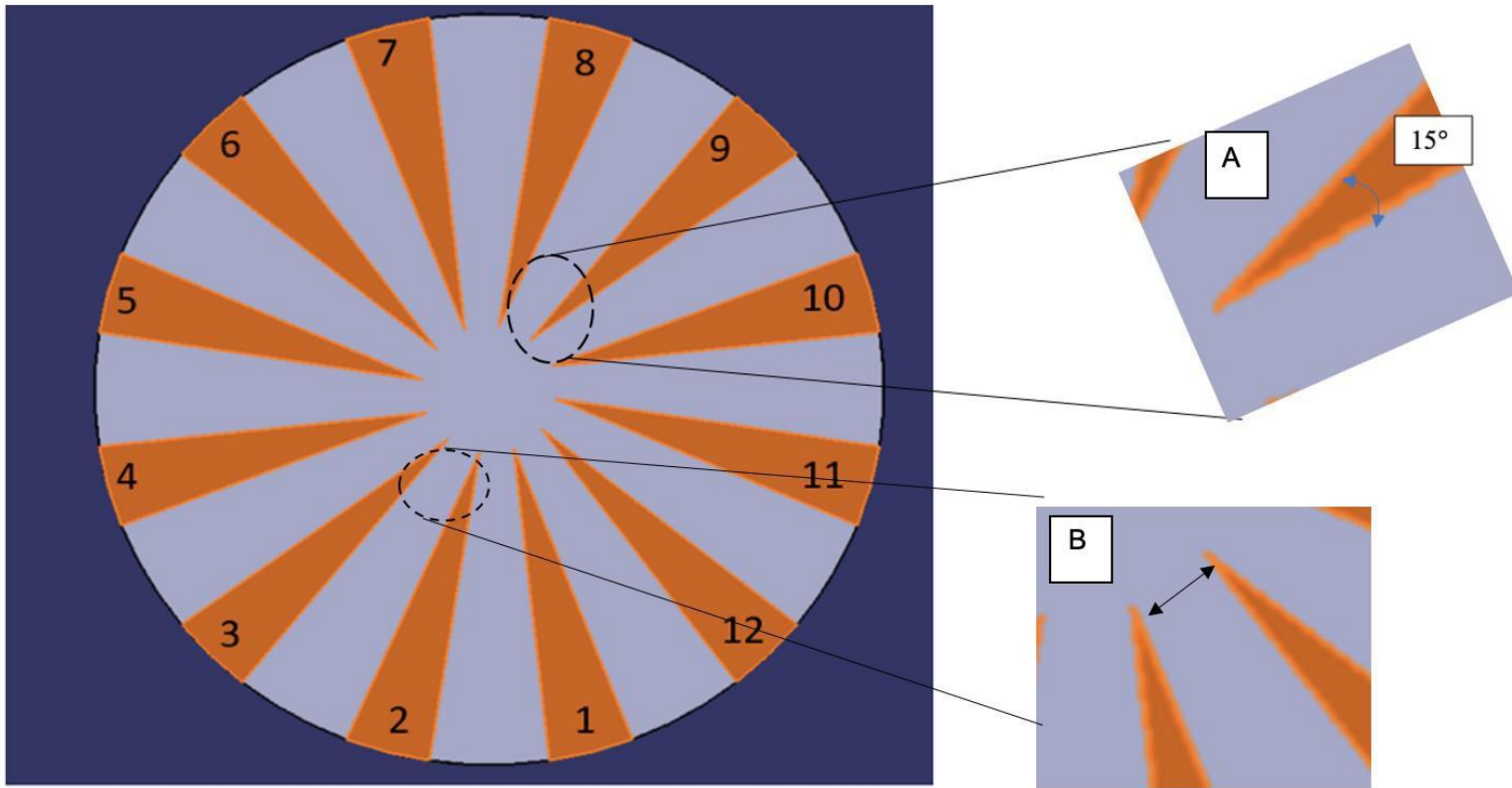


Figure 5. 7: Modified Siemens' star showing gap angle of 15 degrees (A) and minimum width section (B)

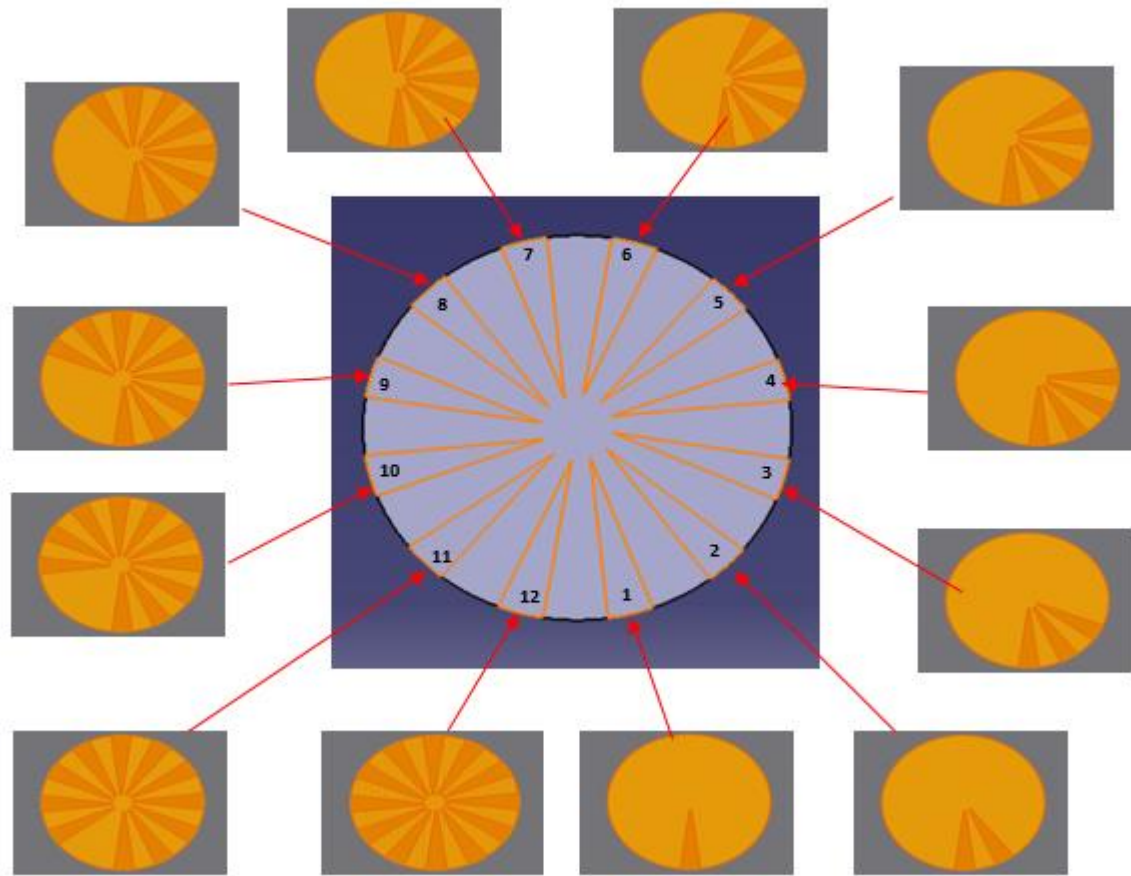


Figure 5. 8: Modified Siemens' star showing variation in build layer height from 25 μ m (1) to 300 μ m (12)

5.4.2 Experimental Setup

A Renishaw AM250 machine with a reduced build volume with length, breadth, and height of 80mm, was used to manufacture the experimental sample. The material used was AlSi10Mg with a chemical composition as shown in Table 5. 3. The main build parameters and thermo- physical properties of the material used are listed in Table 5. 4.

Table 5. 3: Chemical composition of AlSi10Mg powder (Renishaw)

Element	Mass (%)
Aluminium	Balance
Silicon	9.00 to 11.00
Magnesium	0.25 to 0.45
Iron	< 0.25
Nitrogen	< 0.20
Oxygen	< 0.20
Titanium	< 0.15
Zinc	< 0.10
Manganese	< 0.10
Nickel	< 0.05
Copper	< 0.05
Lead	< 0.02
Tin	< 0.02

Table 5. 4: Machine Build Parameters and Thermo physical properties of AlSi10Mg

Parameter	Value	Unit
Laser Power, P	100	W
Laser Point Distance, P_d	60	μm
Laser Exposure time, E_t	90	μs
Laser Speed $\left(\frac{P_d}{E_t}\right)$	0.67	m/s
Hatch spacing, H	110	mm
VED (Calculated)	54.3	Jmm^{-3}
Laser Absorptivity	0.32	-
Melting Temperature, T_m	849	K

Parameter	Value	Unit
Ambient Temperature, T_o	443	K
Density, ρ	2670	Kgm ⁻³
Specific heat capacity, C_p	915	JKg ⁻¹ K ⁻¹
Pi, π	3.14	-
Natural exponent, e	2.71	-

5.4.3 Sample Measurement Process

The samples were measured with a Talysurf Series 2 contact profiler with a gauge resolution of 12.8nm (Taylor Hobson, 2022). This is a surface metrology device which works by tracing the surface profile using a stylus (Zmarzły et al., 2023) as shown in Figure 5. 9. The variations in surface feature depths and heights were recorded for characterisation using Talymap® software.

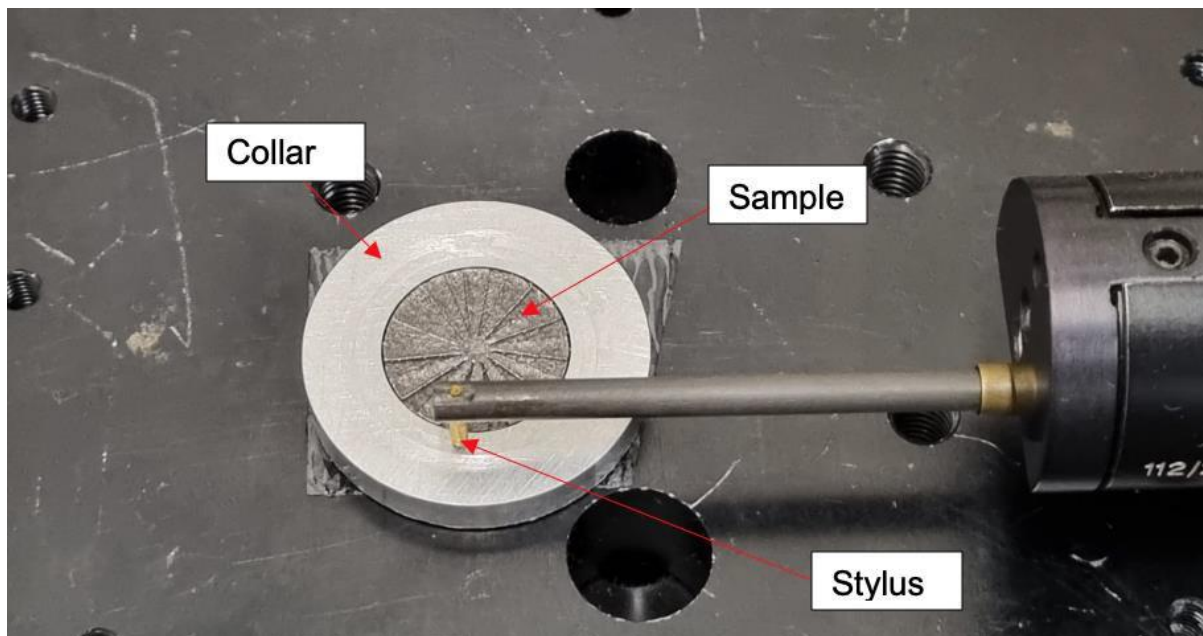


Figure 5. 9: Set up for sample measurement with Talysurf contact profiler.

5.4.4 Sample Data Characterisation

After the surface measurement on Talysurf®, the 3000 measured datapoints (source surface) were exported into Talymap® for characterisation. Firstly, the least squared plane method was used to level the source surface to generate the levelled surface. Next, the non-measured data points were filled in. The neighbouring points were used to calculate a smooth shape in regions with missing data points. Finally, the extract profile operator was used to extract the feature profiles using the circular extraction type with radius defined by the parameter table in appendix 2 (section 9.1). Details of the characterisation operations are in appendix 2 (section 9.1).

5.5 Results

For the results, feature design spacing ranging from 0.2-1.4mm were used to calculate the sum of squared ratios for feature height ranging from 25-300 μ m. A summary of the sum of squares is shown in Table 4-5.

5.5.1 Grading Analysis

The grading analysis for the extracted profile datasets is based on the value of the sum of squared ratios summarised in Table 4-5. This was calculated using equation 5.2. The inputs for the sum of squared ratios equation, W_{mp} , was calculated from equation 5.2 and table 5.4, D_{mp} from equation 5.4 and L_f from the design spacing. From the theory, sum of squared ratios less than one implies full melting conditions or merging of tracks. Therefore, any combination of feature height and feature spacing which results in a sum of squared ratio of less than 1 is expected to result in a non-measurable spacing. This region is graded as the red and is represented by the top left corner of Table 4-5. On the other hand, sum of squares greater than 1 is expected to show a measurable spacing. Figure 5. 11 to Figure 5. 16 show extracted profiles in the red region and green region respectively.

As mentioned earlier, the expectation for the red region is a non-measurable spacing. The extracted profiles corresponding to the red region from Table 4-5, are shown from Figure 5. 11. For each extracted profile, the feature depth is less than 100 μ m. The depth of the extracted profiles for features within the red region was about 20% shallower than the general plain surface texture depth which ranged from 100-120 μ m (appendix 2, section 9.1). Hence, for the red region, the sum of squared ratios could adequately predict the measurability of the spacing.

5.5.1.1 Build Surface Quality

On close examination of the measured surface, several splash and balling effect was noticed within the feature spacings (Figure 5. 10). These may be caused by process uncertainties or process conditions such as low VED.

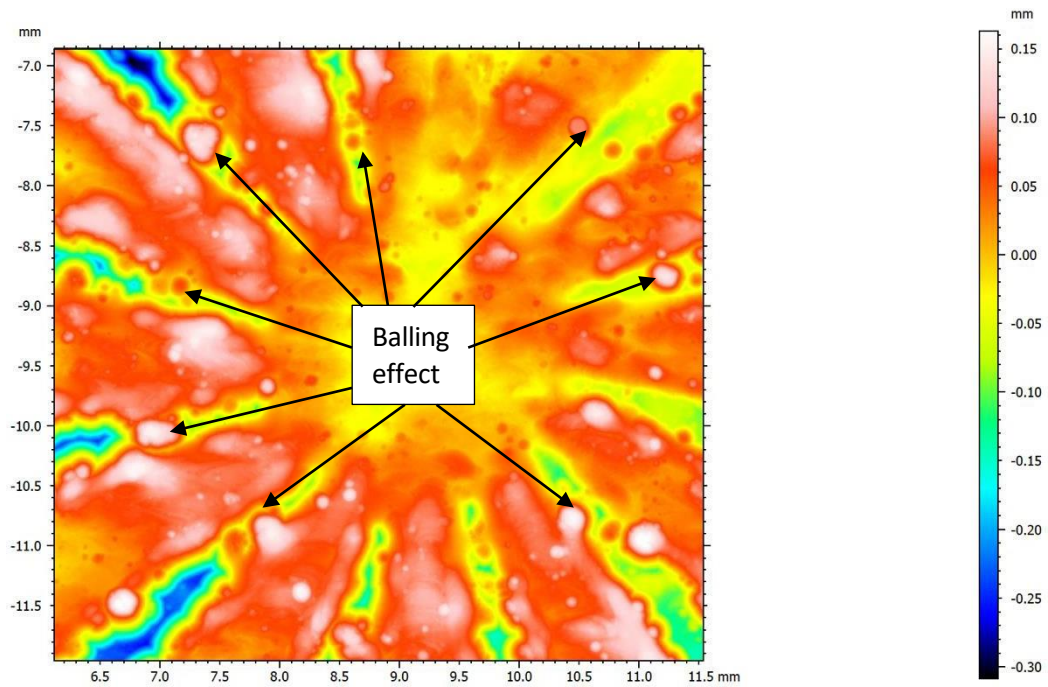


Figure 5. 10: Balling effect in feature spacings.

Table 5. 5: Sum of squares for combination of layer height ranging from 25-300 μ m and design spacing ranging from 0.2 to 1.4mm

FEATURE HEIGHT (μ m)	SPACING (mm)									
	0.2	0.3	0.4	0.5	0.6	0.7	0.8	1	1.2	1.4
25	0.43 ^R	0.94	1.65	2.57 ^G	3.69	5.01	6.54	10.21	14.69	19.98
50	0.51 ^R	1.02	1.73	2.65 ^G	3.77	5.09	6.62	10.28	14.76	20.06
75	0.64 ^R	1.15	1.86	2.77 ^G	3.89	5.22	6.75	10.41	14.89	20.19
100	0.81 ^R	1.32	2.04	2.95 ^G	4.07	5.40	6.92	10.59	15.07	20.36
125	1.04	1.55	2.27	3.18 ^G	4.30	5.63	7.15	10.82	15.30	20.59
150	1.32	1.83	2.55 ^G	3.46 ^G	4.58	5.91	7.43	11.10	15.58	20.87
175	1.65	2.16	2.88 ^G	3.79 ^G	4.91	6.24	7.76	11.43	15.91	21.20
200	2.04	2.55	3.26	4.17	5.29	6.62	8.15	11.81	16.29	21.59
225	2.47	2.99	3.69	4.61	5.73	7.05	8.58	12.24	16.72	22.02
250	2.95	2.95	4.17	5.09	6.21	7.53	9.06	12.73	17.21	22.50
275	3.49	4.00	4.71	5.63	6.75	8.07	9.60	13.26	17.74	23.04
300	4.07	4.58	5.29	6.21	7.33	8.66	10.18	13.85	18.33	23.62

^R: Red region; ^G: Green region.

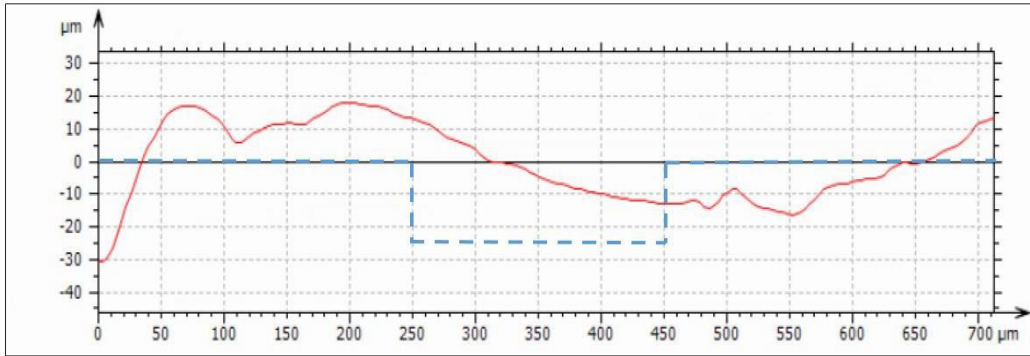


Figure 5. 11: Comparison between measured (red) and design feature (dotted blue) for 0.2mm spacing and 25µm feature height.

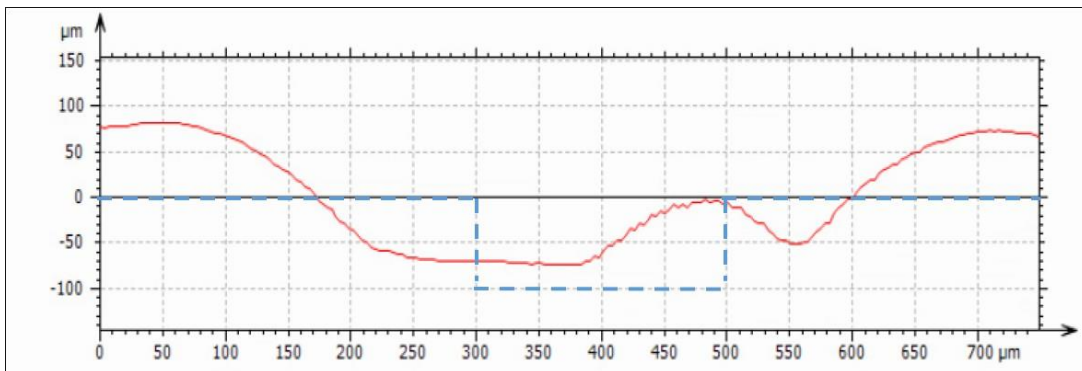


Figure 5. 12: Comparison between measured (red) and design feature (dotted blue) for 0.2mm spacing and 100µm feature height.

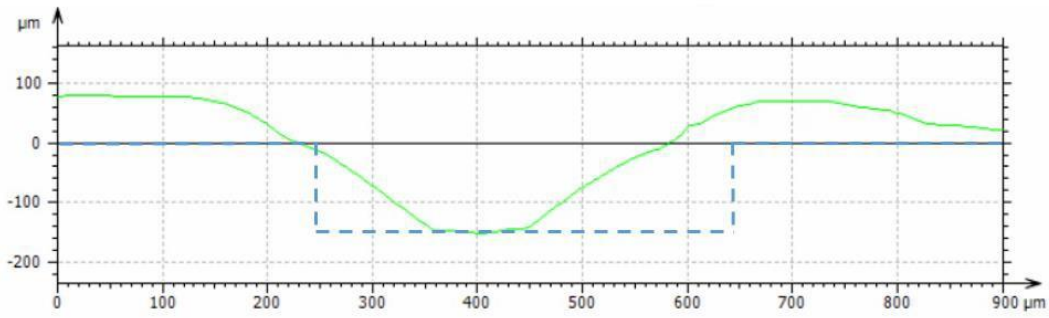


Figure 5. 13: Comparison between measured (green) and design feature (dotted blue) for 0.4mm spacing and 150µm feature height.

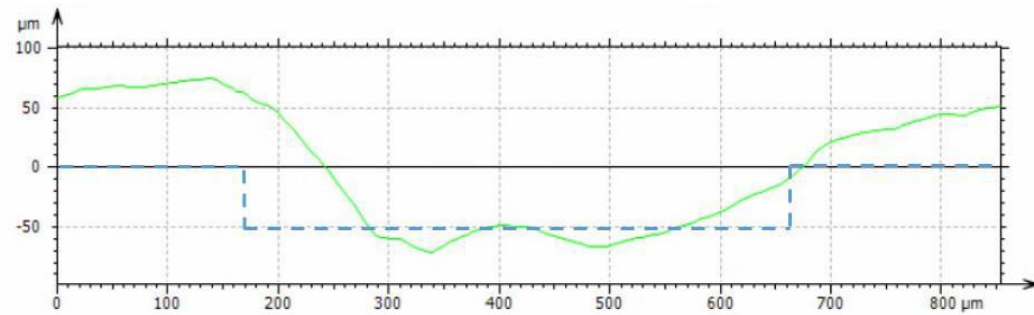


Figure 5. 14: Comparison between measured (green) and design feature (dotted blue) for 0.5mm spacing and 50µm feature height.

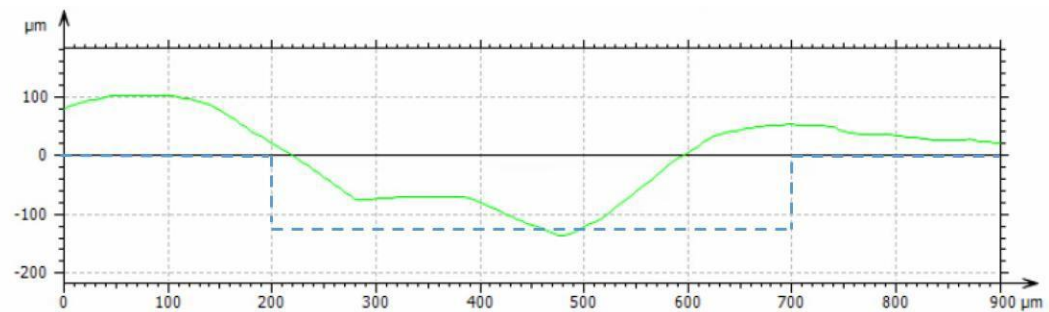


Figure 5. 15: Comparison between measured (red) and design feature (dotted blue) for 0.5mm spacing and 125µm feature height.

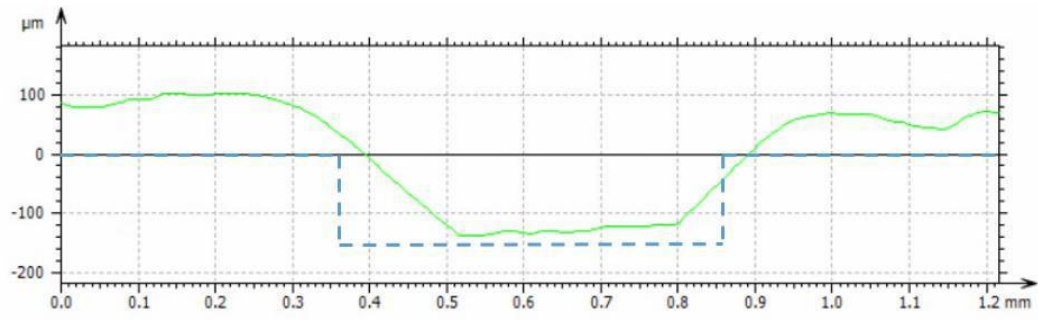


Figure 5. 16: Comparison between measured (green) and design feature (dotted blue) for 0.5mm spacing and 150µm feature height.

5.5.2 Further Analysis: Red Region

Table 5. 5 above is an initial scan of the application of the sum of squared ratios for a combination of feature height and spacing. From the table, the feature spacing limit is at the top left region where the sum of squares is less than 1. Therefore, it was logical to focus on the limiting region to analyse the point at which the feature transitions from a green region (sum of squares greater than 1) to a red region (sum of squares less than 1). To achieve this, a spacing range of 0.25-0.35mm, with increments of 0.05mm, was used to calculate the sum of squared ratios for feature spacing 25-125 μ m, with increments of 25 μ m.

Table 5. 6: Sum of squares for combination of layer height ranging from 25- 125 μ m and design spacing ranging from 0.25 -0.35mm

FEATURE HEIGHT (μ m)	SPACING (mm)		
	0.25	0.30	0.35
25	0.66	0.94	1.27
50	0.74	1.02	1.35
75	0.87	1.15	1.48
100	1.04	1.32	1.65

From Table 5. 6, the largest value of sum of squared ratio is 1.65 which corresponds to a spacing of 0.35mm and feature height of 100 μ m. This corresponds to a feature radius of 2.7mm

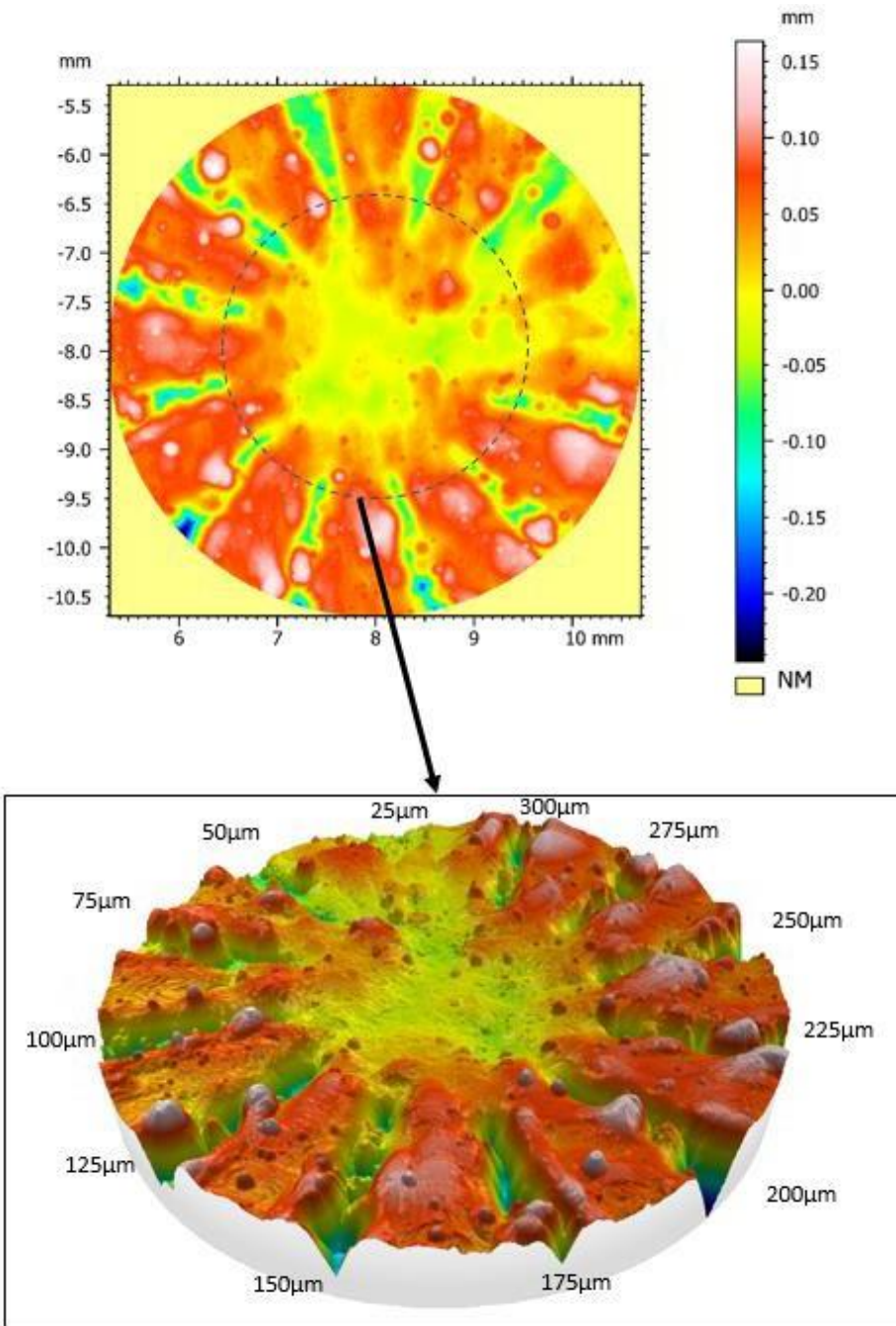


Figure 5. 17: Circular extracted profile for 0.35mm spacing and 25-300µm feature height, 3D view for 0.35mm spacing.

From Figure 5. 17, which corresponds to a spacing of 0.35mm, it is clear that there is no obvious spacing for 25µm (sum of squared ratio of 1.27). This shows that indeed, the spacing limit to resolve the gap between adjacent features for this experiment is at a feature width of 0.35mm or less.

5.6 Discussion

The sum of squared ratios was used to predict which combination of feature height and design spacing will yield a measurable spacing, based on the assumption that a measurable spacing will be visible.

The results from the table of sum of squared ratios show that, out of 108 calculated sums of squared ratios, about 4% of the ratios were graded as red. Also, the red region was located at the top right corner of the table. This is where the feature height (H_f) were the smallest. From Figure 5. 17, it was clear that indeed, there was no obvious spacing for 25 μ m (sum of squared ratio of 1.27). This result indicates that the sum of squared ratios provides a viable method to quickly assess which design feature spacing will yield a measurable, hence visible gap after LPBF fabrication.

Also, a limit for sum of squared ratios of one should be used as a target value to obtain a clear measurable spacing.

5.7 Conclusion

Surface texturing involves the formation of different patterns on the surface of a material and can be used to improve the aesthetic characteristics of LPBF parts. The texture pattern depends on factors such as the feature size and the spacing between features.

This chapter proposed an approach for determining the minimum measurable spacing between two adjacent features for a specified design feature depth. To achieve this, a method for analysing the process conditions for achieving minimum measurable spacing has been developed. The methodology accounts for the theoretical melt-pool width, build layer height, melt-pool depth and feature spacing.

In summary, the proposed guidelines in Chapters 4 and 5 may assist to predict the minimum feature size for a machine/material combination.

Therefore, this information can provide production engineers and designers with a method of accurately predicting the size and spacing of textures which can be manufactured on horizontal LPBF surfaces. It should be noted that since the data was

collected from a small sample with unique physical characteristics and material with unique thermophysical characteristics, these results cannot be generalised for a broad range of machine/materials or designs.

For future work, it will be interesting to investigate the impact of the variation in melt-pool width and depth on measurable spacing. Also, how to account for and minimise the impact of balling effect on the measurability of the feature spacing.

6 Aesthetic Evaluation of Textured LPBF Surfaces

6.1 Aesthetic considerations in LPBF

The subjective estimation of surface quality by customers is an important aspect of visible part acceptance within the aircraft interior industry.

Chapters 4 and 5 have defined analytical approaches for determining the feature width and spacing respectively. These insights can assist designers to create CAD textures which can be manufacturable by LPBF for a machine and material combination. But in addition to an aesthetic texture design process focusing purely on textures geometries, the influence of the manufacturing process used to produce the selected geometries, is also critical to human aesthetic surface perception.

Currently, the design of aesthetic textures with submillimetre geometries is possible on digital platforms but their actual aesthetic properties after production by LPBF process is difficult to assess due to the process uncertainties. Design rules on how to adapt textures for a particular machine and material combination are required to provide designers with a better control over printed texture outcome. The demand for Novel DFAM approaches have been recognised in literature by various authors such as (AMFG, 2019; Bahnini et al., 2018; Blakey-Milner et al., 2021; Maidin, Campbell and Pei, 2012; Pradel et al., 2018; Thomas & Gilbert, 2014). However, most of these approaches relate to optimising functional and mechanical properties of the surface rather than improving its aesthetic qualities. There have been some studies which have looked into surface appearance such as Galimberti et al (2016), who assessed the correlation between surface aesthetic perception of LPBF parts and post processing, geometry and build strategy parameters.

Texture perception evaluations have also been performed on other manufacturing processes. Ramanakoto *et al* (2019) on investigating planed and sanded surfaces of beach and oak, found that the tactile sensation can be correlated with Ssk, Vmc and Sk. The authors also noted that material type and subsequently, the material texture has an impact on the perceived appearance of the part. Also, Bhatta *et al.*, (2017) while investigating the factors that affect the tactile evaluation of wooden surface, found that compared to coated surface, the tactile perception of natural and smooth surfaces were ranked more positively. Fu et al., (2019) when quantifying the relationship between hard metrological data from surface materials and soft metrology

(human perception), found that the density of the metal used affects the perception of humans.

Despite such studies, the aesthetic quality of custom design textures verses plain or untextured samples, have not yet been evaluated. Likewise, in terms of macro surface textures produced by LPBF, it was identified that there currently are no methods to help assess the influence of parameters such as surface texture size, post processing and absence/presence of texture on the perceived appearance of parts.

6.2 Chapter's Objectives

As highlighted in the previous section, more research needs to be conducted to gain a deeper understanding on the influence of surface textures directly produced by LPBF on aesthetic perception and ultimately to better support the design of surfaces textured by LPBF from an aesthetic perspective, from concept stages, through manufacturing to post processing.

As a further step in pursuit of this objective, the primary goal of this chapter is to assess whether an aesthetically pleasing texture can be created by combining the smallest feasible feature sizes (width and spacing) that a machine can produce to generate a texture. These sizes will be determined using the methods established in the preceding chapters and the outcome of this assessment will be compared to a conventional plain surface texture.

A secondary goal of this chapter is to validate the methodology introduced in the previous chapters. This will be achieved by comparing the texture designed in this chapter, using the minimum feature sizes feasible for the machine, to two other textures. One of the two textures will be designed using feature sizes theoretically lower than the machine's capability, while the other texture will be designed using feature sizes theoretically higher than the machine's capability.

In the first section, the designed samples are described together with the manufacturing process and the post processing technique used. The following section describes an aesthetic assessment methodology specifically designed to capture emotional feedback from a group of individuals when evaluating the tactile and visual

aesthetic qualities of the designed samples. Finally, the individual assessments are analysed in detail to achieve the primary and secondary goals mentioned previously.

6.3 Textured Samples used for Aesthetic Evaluation

6.3.1 Samples Design

The design of the textures is based on a plane surface of 54 square shapes arranged in an eight by seven matrix with dimensions of 50x45x5mm (LxWxD) by the CATIA V5 software. This is shown in Figure 6. 1.

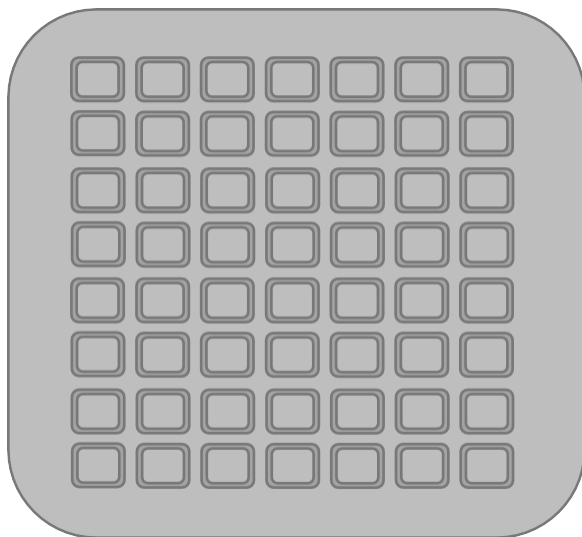


Figure 6. 1: 50x45x5mm (LxWxD) sample with designed texture

Three combinations of square shape types and spacing (Figure 6. 2 and Figure 6. 3) were used to create three texture types ($T_{=min}$, $T_{<min}$ and $T_{>min}$), designed to help evaluate the influence of the minimal features sizes calculate in the previous chapter on the aesthetic perception.

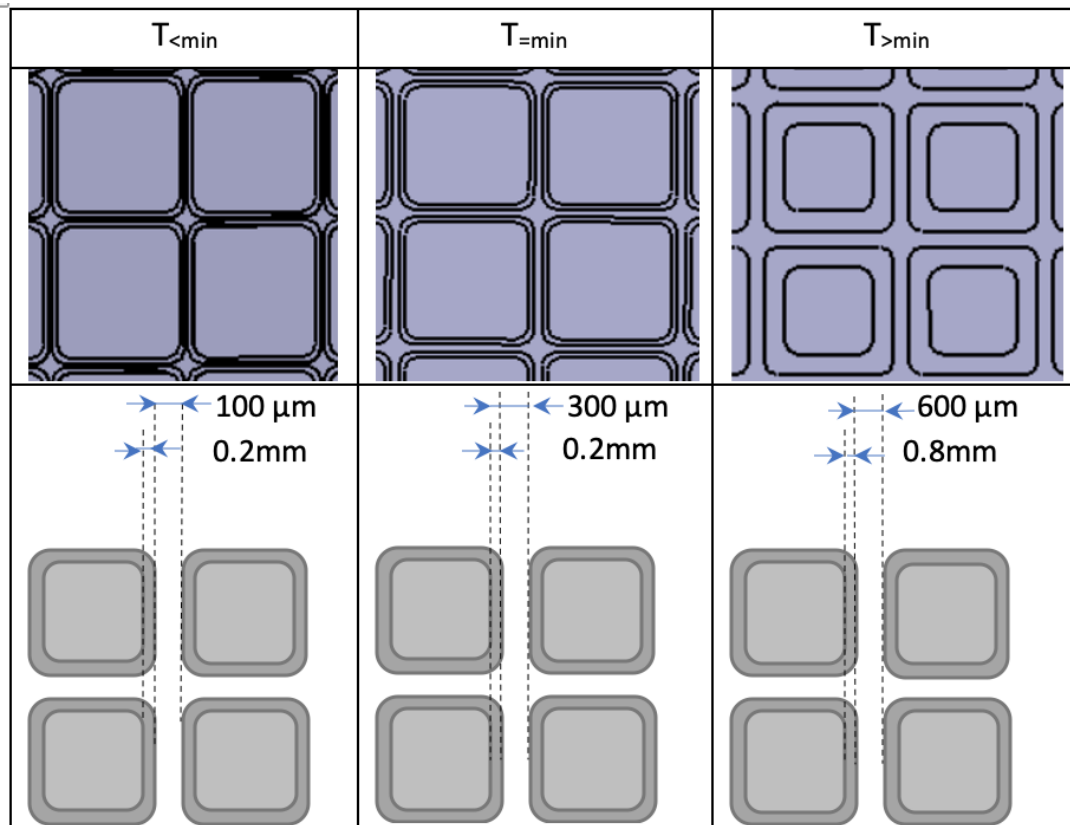


Figure 6. 2: Three texture sizes $T_{<min}$, $T_{=min}$ $T_{>min}$

In the previous chapter, the analytical minimum feature width was calculated as $300\mu\text{m}$ (0.3mm). Therefore, it was used to set the dimensions of the first texture type $T_{=min}$, which aimed at matching the machine/material capability. For the second texture type $T_{<min}$, $T_{=min}$ dimensions were scaled down by 30% to produce a texture below the theoretical machine/material capability. Similarly, the third texture type $T_{>min}$ was achieved by scaling up $T_{=min}$ by a factor of two to generate a texture type significantly above the theoretical machine/material capability. In addition, the sum of squared ratios (from Chapter 4) was used to determine which combination of feature spacing H_f and feature height, L_f would yield a measurable spacing. Therefore $T_{<min}$ was designed with sum of squared ratio of 0.56 (red region) while $T_{=min}$ and $T_{>min}$ was designed with sum of squared ratios of 3.22 and 28.88 respectively (green).

The parameters for the three texture types are summarised in Table 6. 1.

Table 6. 1: Summary of Baseline Design Parameters where H_f refers to the feature spacing and L_f refers to the feature height.

Texture Type	Feature Width (mm)	H_f (mm)	L_f (μm)	Sum of Squared Ratios	Aspect Ratio (L_f/H_f)
$T_{<min}$	0.1	0.2	50	0.56	0.25
$T_{=min}$	0.3	0.2	200	3.22	1
$T_{>min}$	0.6	0.8	800	28.88	1

In addition to the three textured samples, an untextured sample with a plain surface P of the same external dimensions was also designed to compare aesthetic perceptions of the textured samples with an as-built surface.

6.3.2 Samples Manufacturing (LPBF)

The AM250 machine was used to manufacture all samples. Two pairs of each texture types ($T_{=min}$, $T_{<min}$, $T_{>min}$ and P) were produced leading to a total of eight samples (Figure 6. 3). This machine is equipped with a 200W PWM laser and a build volume of 250x250x300mm. Stainless steel SS316L powder was used with a particle size ranging between $45\pm 15\mu\text{m}$ (Pagáč et al., 2017). The build parameters and chemical composition of SS316L are summarised in Table 6. 2 and Table 6. 3 respectively.

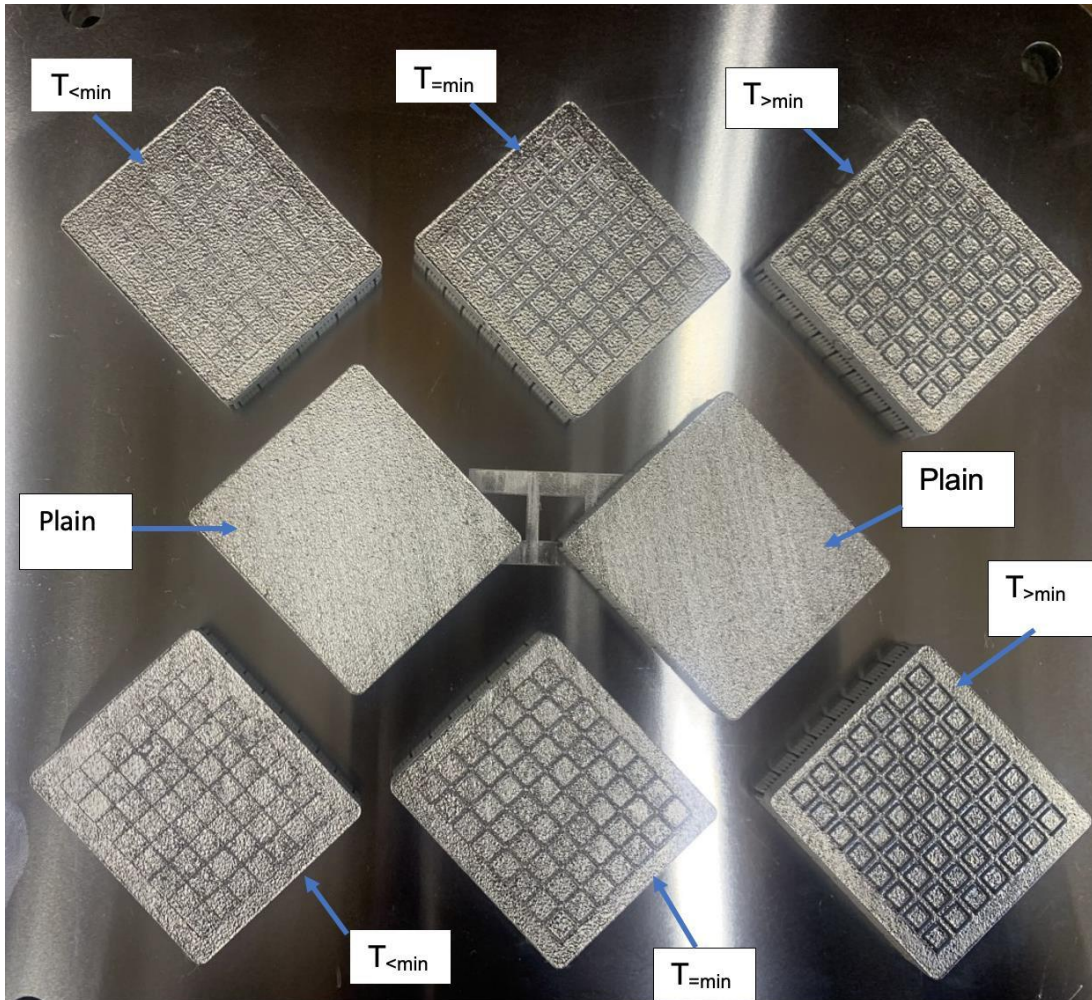


Figure 6. 3: Build Tray showing sample pairs with variation in texture size.

The values selected in Table 6. 2 were recommended by the manufacturer to manufacturer to produce parts in SS316L of good mechanical and surface quality.

Table 6. 2: Build power and speed for AM250 for Stainless Steel SS316L processing.

Power (Hatch)	200W
Power (Border)	110W
Point Distance(μm)	60
Exposure time (μs)	80

Table 6. 3: Chemical Composition of SS316L. (Renishaw, 2001)

Element	Mass (%)
Iron	Balance
Chromium	16.00-18.00
Nickel	10.00-14.00
Molybdenum	2.00-3.00
Manganese	≤ 2.00
Silicon	≤ 1.00
Nitrogen	≤ 0.10
Phosphorus	≤ 0.045
Carbon	≤ 0.03
Sulphur	≤ 0.015

6.3.3 Post Processing of Samples

For aesthetic surfaces, post processing techniques are often applied to improve the surface characteristics of parts such as jewellery (Ghazy, 2012) and wearable AM clothes (Lestrangle, 2016). There are also a variety of post processing techniques which are used for improving LPBF surfaces ranging from mechanical, thermal, electro chemical and chemical processes (Sibanda et al., 2019). Therefore, to better evaluate the aesthetic perception of the textured surfaces, it was decided to also assess the influence of a standard surface improvement technique on aesthetic perception by post processing one sample of each texture type pair. Among the variety of post processing techniques, bead blasting was selected because it visibly smoothens the surface without interfering with the surface chemical properties of the surface. Furthermore, bead blasting was used for a previous LPBF aesthetic surface research and was selected by the authors who cited choosing the technique because it was ideal for metal LPBF surfaces.

The Guyson Formula 1600 was used to bead blast selected samples for a duration of two minutes. The Formula 1600 is ideal for industrial applications and has an internal blast chamber with dimensions of 770x1070x760mm (H x W x D) (Guyson, 2023). It is equipped with a foot operated blast gun. The blast media used was soda-lime glass beads (Guyson honite grade 10). The grain size ranged from 180 - 300 μ m (Guyson, 2020). Thus, out of the eight geometries which were printed by LPBF, four were left in the as-built state and four were bead blasted. The samples which were not subjected to post processing after the LPBF process will be referred to as “as built” whereas the samples which were post processed were referred to as “bead blasted”.

6.4 Aesthetic assessment

To generate an unbiased assessment, the produced sample were aesthetically assessed separately by a group of volunteers. The following sections describe the select assessment method used and the assessment setup.

6.4.1 Method for capturing individual assessors' feedback.

According to Violante et al (2019), there are three main methods of capturing emotional feedback from assessors. These methods are summarised below:

- The physiological method

This method is based on the gathering of two main types of information. The first is central information by electro encephalography and the second is the peripheral information which is a combination of electromyography, electro dermal activities, blood volume pulse, among others to ascertain the emotional feedback of an individual (Violante *et al.*, 2019).

- The observation method or behavioural method

This technique involves the careful observation of individuals, in the process of a product experience, and relying on the insights gained from the observation as emotional feedback. This can be subjective or objective insights gained from observing behaviour of individuals such as the movement of the body, posture, facial expressions, and gestures (Violante *et al.*, 2019).

- The questioning method

This method can either take the form of group, individual or focus group interviews. Affective engineering techniques such as the Kansei affective engineering approach are ideal for the questioning method (Violante *et al.*, 2019). The choice of questioning depends on the overall project objectives. The main difference between the questioning methods is that focus groups are more structured group interviews involving more than one individual and a facilitator whereas the individual questioning method involves one person at a time and can either be structure or non-structured (Lestrangle, 2016).

The method selected for this thesis was the individual questioning method. It is similar to that used by other authors such as Galimberti et al., (2015), for assessing the aesthetic characteristics of LPBF products, Li *et al.*, (2017) for the visuo-tactile perception of polymer 3D printed parts, Ramanakoto et al., (2019) to define the acceptable surface quality for raised grain wood surfaces and Ramananantoandro et al., (2014), to find a suitable objective roughness parameter linked to human perception of wood surfaces.

A critical step in the questioning method is to decide on the approach for structuring the questions for the individual assessments. The Two Alternative Forced Choice (2AFC) approach was selected because it forces the assessors to make a choice rather than being indecisive for fear of making mistakes (Lestrange, 2016). This approach is ideal for naïve assessors. Since about 62.5% of the assessment participants had minimal knowledge of Additive Manufacturing, as shown in Figure 6.4.

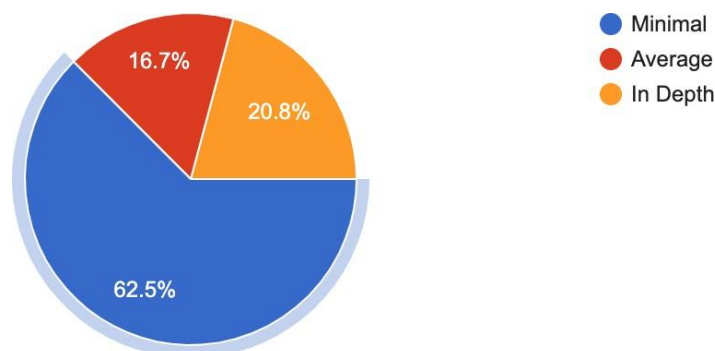


Figure 6. 4: Level of understanding of LPBF from 24 individual assessors.

Experimentally, the 2AFC approach involves presenting assessors with two products and asking them to select one out of the two which meet a set criteria (Lestrange, 2016). In the case of this experiment, participants were presented with two samples at a time and asked to choose which of the samples they perceived as most attractive (for instance), where visual surface perception was the focus of the test.

6.4.2 Capturing Individual Surface Perception

From past publications, other authors have used different approaches to describe the appearance of objects or surfaces for assessments (Bhatta et al., 2017; Eriksson, Rosen and Bergman, 2018; Fujisaki, Tokita and Kariya., 2015; Galimberti et al., 2016; Liem, Abidin and Warell., 2009; Nakamura et al., 2018; Schütte, 2005; Zeithaml, 1988; Zuo, 2010). From previous approaches, list of adjectives was developed and used to describe the appearance of a surface. For the individual questioning, three main adjectives were selected: attractive, pleasant and preference. This was because, for visible aircraft interior products, the main human senses for interacting with products are vision, touch or a combination of both vision and touch (visuo-tactile).

The attractive, pleasant or preference adjectives were based on visual, tactile, and visuo-tactile perceptions respectively hence appropriate for this assessment. At the start of the assessment, the participants were provided with a briefing on the overall goal of the experiment and asked to scan a QR code which contained all the assessment questions linked to a google forms document. The participants were requested to evaluate the appearance of the surface of a pair of samples by following the prompts shown on their respective screens. Each sample set was placed directly in front of the individual assessor, with all samples engraved for easy differentiation and identification (Figure 6. 5). For each question under attractive, pleasant or preference adjective(s), each assessor was asked to choose a sample per set by selecting the sample letter on their screen. For example, if the assessor found sample E more pleasant compared to sample F, he selects "SAMPLE E" on his screen (Figure 6. 5C).

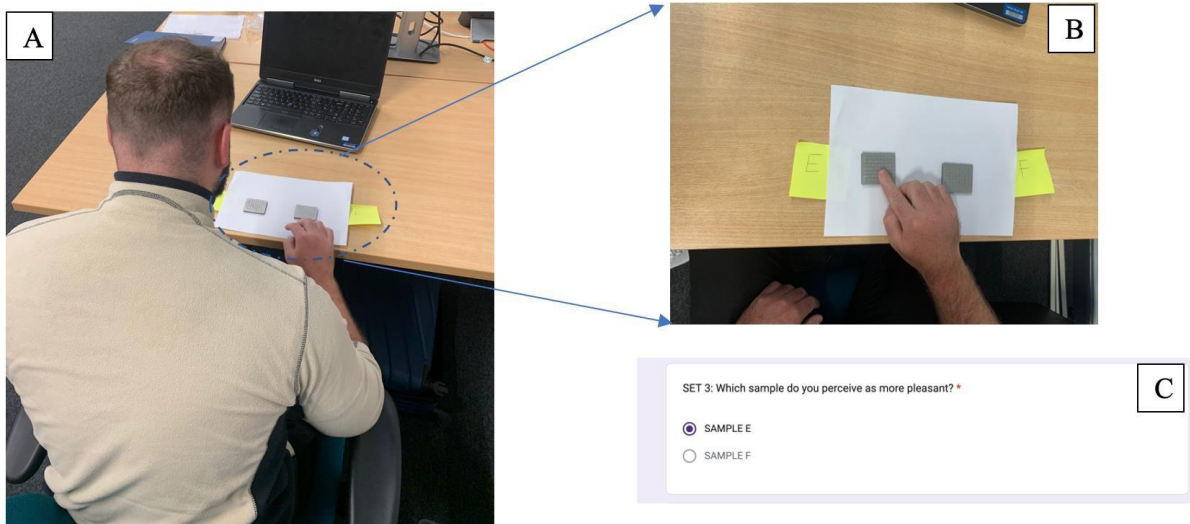


Figure 6. 5: Experimental set up impression (A); Pleasant adjective / Tactile assessment (B); Tactile Assessment Question (C).

The questions were structure to assess attractiveness (visual) followed by pleasantness (tactile) and finally preference (visuo-tactile). The assessment on the screen began with a statement as follows: “This assessment is a visual/tactile/visuo-tactile test and you will be presented with one sample pair at a time”. A pair of samples will be presented to the assessor with the first set labelled A-B, second set labelled C-D and so on (Figure 6. 5B). After the statement, the following question was presented to the assessor.

“For each sample pair, select the sample you perceive as more (adjective)?” Where adjective can be attractive, pleasant, or preferable.

For the “attractive” adjective, the main parameters which were varied were post processing and presence/absence of texture. However, for the “pleasant” adjective, only one parameter was varied being post processing keeping surface texture the same. Likewise, for “preference” adjective, texture size was varied keeping post processing the same.

6.5 Individual assessment setup

The experiment took place in a well-lit room to ensure homogenous illumination of the sample surface. In addition, participants were requested to remain seated at all times of the assessment to enable consistent assessment position for all individuals. It took approximately 25 minutes for each complete assessment and a total of 14 days to complete the full study. Participants were not compensated monetarily for taking part in the exercise. A total of 24 participants (66.7% male and 29.2% female) were chosen to individually assess the sample sets. From previous published literature, a minimum of 20 participants are required for the assessment to be significant hence 24 participants can be deemed adequate (Ramananantoandro et al. 2014).

Participants were presented separately with 5 batches of samples organised in sets of two samples (as described in the previous section) to evaluate the influence of As Built (AB) surfaces, Bead Blasted surfaces (BB), textured surfaces and texture sizes. For each batch, the samples were randomly labelled with a letter (A to H), thus hiding the exact specifications of the samples. The Kansei affective engineering technique was used whereby individuals were asked to assess the surfaces based on the adjective's attractiveness (visual assessment), pleasantness (tactile assessment) and preference (visuo-tactile assessment).

6.5.1 Visual Assessments: "Attractive" Adjective

6.5.1.1 Batch 1 - As-built vs Polished: "Attractive"

A total of four sets of samples were used for the first batch of attractive adjective assessment with variation in post processing. The sample set number and labels are shown in Table 6. 4.

Table 6. 4: Sample set for "attractive" adjective with variation in post processing

Set Number	Sample 1	Sample 2
Set 1	A ($T_{>min}$ - AB)	B ($T_{>min}$ - BB)
Set 2	C ($T_{=min}$ - AB)	D ($T_{=min}$ - BB)
Set 3	E ($T_{<min}$ - AB)	F ($T_{<min}$ - BB)
Set 4	G ($T_{<min}$ - AB)	H ($T_{<min}$ - BB)

6.5.1.2 Batch 2 - Textured vs Plain: "Attractive"

A total of three sets of samples were used for the second batch which aimed assessing attractiveness of surfaces with presence or absence of textures on as-built surfaces. For each set presented to the assessor, a textured sample A (for example $T_{>min}$) was paired with the as-built plain sample (Table 6. 5).

Table 6. 5: Sample set for "attractive" adjective with presence/absence of texture (As Built)

Set Number	Sample 1	Sample 2
Set 1	A ($T_{>min}$ - AB)	B (Plain - AB)
Set 2	C ($T_{=min}$ - AB)	D (Plain - AB)
Set 3	E ($T_{<min}$ - AB)	F (Plain - AB)

6.5.1.3 *Batch 3 - Textured vs Plain: Attractive*

Similar to the previous batch, a total of three sets of samples were used for the third batch which aimed assessing attractiveness of surfaces with presence or absence of textures on polished surfaces. For the visual test, three sets of sample pairs were presented to the assessors because there were only three texture types which the author aimed to assess for the perceived attractiveness. For each set presented to the assessor, a textured sample A (for example $T_{>min}$) was paired with the bead blasted plain sample (Table 6. 6)

Table 6. 6: : Sample set for "attractive" adjective with presence/absence of texture (bead blasted).

Set Number	Sample 1	Sample 2
Set 1	A ($T_{>min}$ - BB)	B (Plain - BB)
Set 2	C ($T_{=min}$ - BB)	D (Plain - BB)
Set 3	E ($T_{<min}$ - BB)	F (Plain - BB)

6.5.2 Tactile Assessment - "Pleasant" Adjective

6.5.2.1 *Batch 4 - As-built vs Polished*

Similar to the first batch of "attractive" adjective assessment (Table 6. 4), the "pleasant" adjective assessment was carried out with four sets of samples. Each sample set had the same texture design but different surface finish to compare the effect of bead blasting on the tactile perception of the surfaces (Table 6. 7).

Table 6. 7: Sample set for "pleasant" adjective with variation in postprocessing

Set Number	Sample 1	Sample 2
Set 1	A ($T_{>min}$ - BB)	B ($T_{>min}$ - AB)
Set 2	C ($T_{=min}$ - BB)	D ($T_{=min}$ - AB)
Set 3	E ($T_{<min}$ - BB)	F ($T_{<min}$ - AB)
Set 4	G (Plain - BB)	H (Plain - AB)

6.5.3 Visuo-tactile Assessment – “Preference Adjective”

6.5.3.1 Batch 5 – Texture type comparison

Finally, the assessment on the “preference” adjective was carried out with three sets of samples, aiming at comparing the three types of textures ($T_{<min}$, $T_{=min}$, and $T_{>min}$). Each sample being post processed using bead blasting. (Table 6. 8).

With the preference adjective, we only wanted to assess the textured samples only. To see if the texture size makes a difference to what is preferred. Only the bead blasted surfaces were selected for the assessment considering that for production parts, only post processed surfaces will be assessable to the customer.

Table 6. 8: Sample set for "preference" adjective with variation in Texture Size.

Set Number	Sample 1	Sample 2
Set 1	A ($T_{>min}$ - BB)	B ($T_{=min}$ - BB)
Set 2	C ($T_{>min}$ - BB)	D ($T_{<min}$ - BB)
Set 3	E ($T_{=min}$ - BB)	F ($T_{<min}$ - BB)

6.6 Initial Surface Qualitative Assessment

Photographs of the as-built and bead blasted surfaces were taken to compare the visual differences between as-built and bead blasted surfaces. In addition, Sensofar 3D profiler was used to extract the surface optical profiles. From the photographs (Figure 6. 6 - Figure 6. 9 A and C), the as-built surface has a shiny finish whereas the bead blasted surface has a matt appearance. Also, the optical surface profiles for the as-built samples (Figure 6. 6 - Figure 6. 9A) show visible laser scan tracks on the surface. The bead blasted samples, in comparison are characterised by a more homogenous surface with the absence of scan tracks (Figure 6. 6- Figure 6. 9C). This is because the bead blasting process smoothens the surface hence getting rid of the laser tracks.

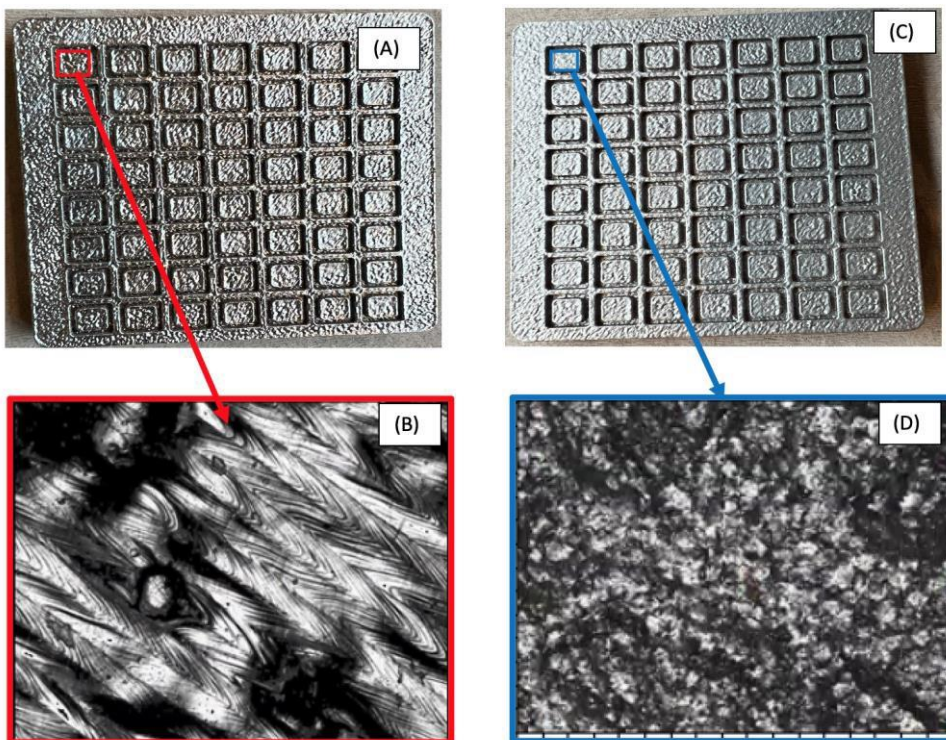


Figure 6. 6: LPBF textured surfaces ($T > \min$). As Built: (A) Photograph, (B) Optical Surface Profile (Sensomap).

Bead Blasted: (C) Photograph, (D) Optical Surface profile (Sensomap)

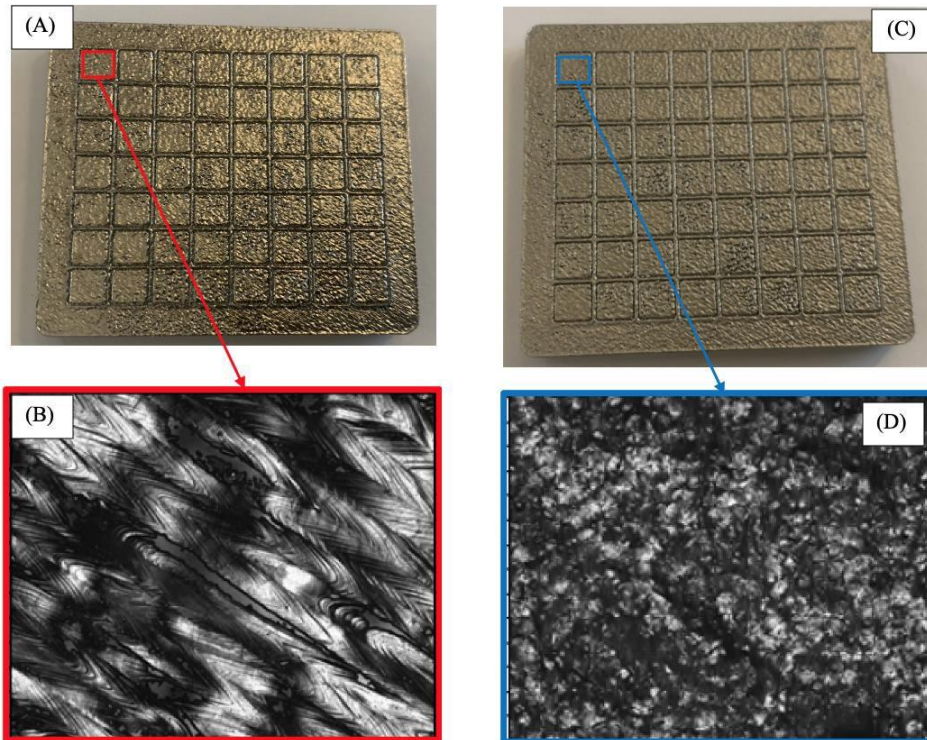


Figure 6. 7: LPBF textured surfaces ($T=\min$). As Built: (A) Photograph, (B) Optical Surface Profile (Sensomap). Bead Blasted: (C) Photograph, (D) Optical Surface profile (Sensomap)

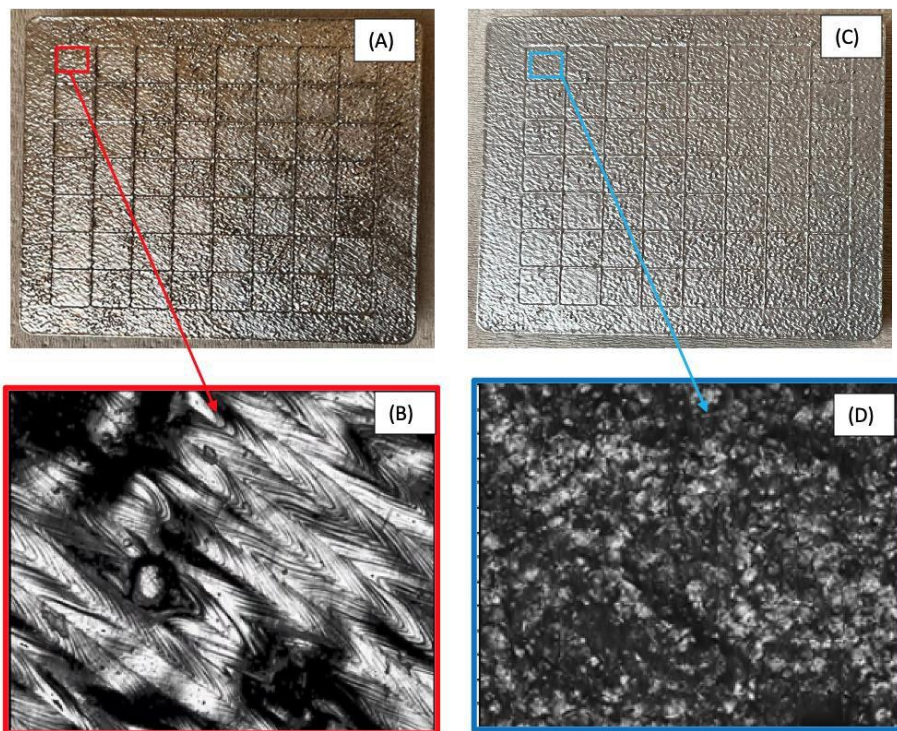


Figure 6. 8: LPBF textured surfaces ($T<\min$). As Built: (A) Photograph, (B) Optical Surface Profile (Sensomap).

Bead Blasted: (C) Photograph, (D) Optical Surface profile (Sensomap)

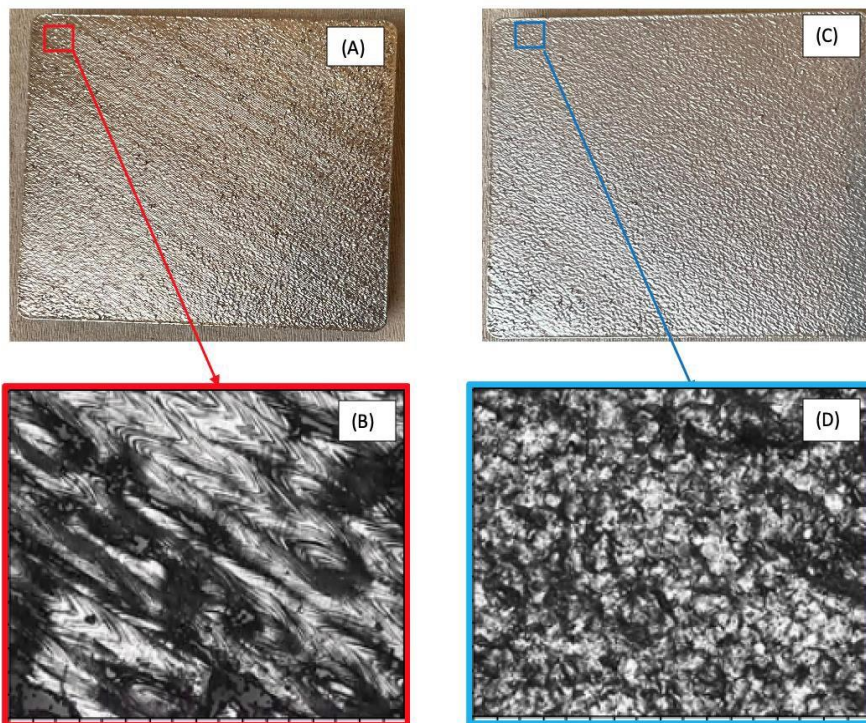


Figure 6. 9: LPBF surfaces (Plain). As Built: (A) Photograph, (B) Optical Surface Profile (Sensomap). Bead Blasted: (C) Photograph, (D) Optical Surface profile (Sensomap).

6.7 Aesthetic Assessment Results

The quantitative results were analysed by calculating the number of times a sample was chosen as a percentage of the total number of responses for a specific experimental set. The results for the attractive attribute were presented first analysing the effect of post processing on visual adjective followed by the effect of design variation for as built and bead blasted surfaces. The second section presents the results from the pleasant adjective assessment and finally the results from the preference adjective are discussed.

6.7.1 Visual Assessment (Attractive Adjective)

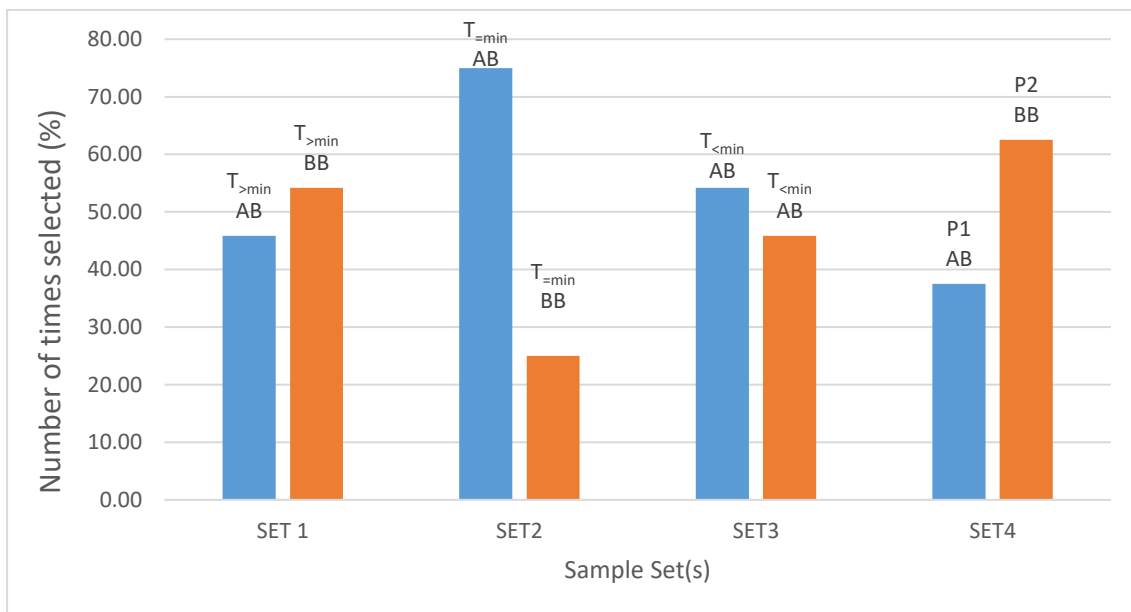


Figure 6. 10: Variation in post-processing (same design per set).

In order to examine the data, the number of times a sample was chosen (n_c) was divided by the total number of participants (n_{tp}) and multiplied by 100 to give the percentage score for that sample. This can be calculated using equation 6.1.

This formula was applied to Figure 5.10-Figure 5.14.

$$\text{Percentage Score} = \frac{n_c}{n_{tp}} \times 100 \quad (6.1)$$

Figure 6. 10 shows the results for visual perception of surfaces comparing as built (AB) to bead blasted (BB) surfaces (Batch 1). The results show that there is minimal (<10%) difference in the perceived attractive of T>min – AB compared to T>min - BB and for T<min - AB compared to T<min - BB. For the T>min set, assessors commented about their personal preference for shiny/matt surfaces rather than surface quality. For example, an individual who selected the shiny surface (T>min - AB) commented that the choice for Sample A was because they were visually drawn to shiny surfaces. Another individual mentioned that in the context of decorative surfaces, they found matt surfaces more visually attractive than shiny surfaces. This might explain why both T>min as built, and post processed surfaces did not have a significant difference in visual perception. It was also observed that both surfaces were free of defects. Essentially, the bead blasting process did not add significant value to the surface.

The assessors' comments for T<min set suggest that both as built, and bead blasted surfaces were of poor quality hence a choice was made by selecting the slightly better-looking surface. This supports the assumption that by designing and printing textures below theoretical machine/material capability, the texture does not improve the surface aesthetic quality. On the other hand, the results for T=min show a significant difference in perceived visual attractiveness (>50%) after post processing. The T=min - BB sample had the lowest preference in the overall assessment for the attractive adjective exercise. It seems that the post processing exercise produced the opposite effect of T>min by reducing the level of aesthetic attractiveness. Comments from assessors were about the more obvious visible defect on the surface of T=min – BB. Both T=min- AB and T=min- BB had some build defects which may have resulted from uneven powder distribution on the surface of the powder bed. However, the defects were more obvious on T=min – BB.

Similarly, the Plain – AB surface had the lower score compared to the Plain –BB. The comments were identical to that of T=min, however in this case, it was the as-built surface which appeared non-homogeneous. Textured vs Plain surfaces (As Built).

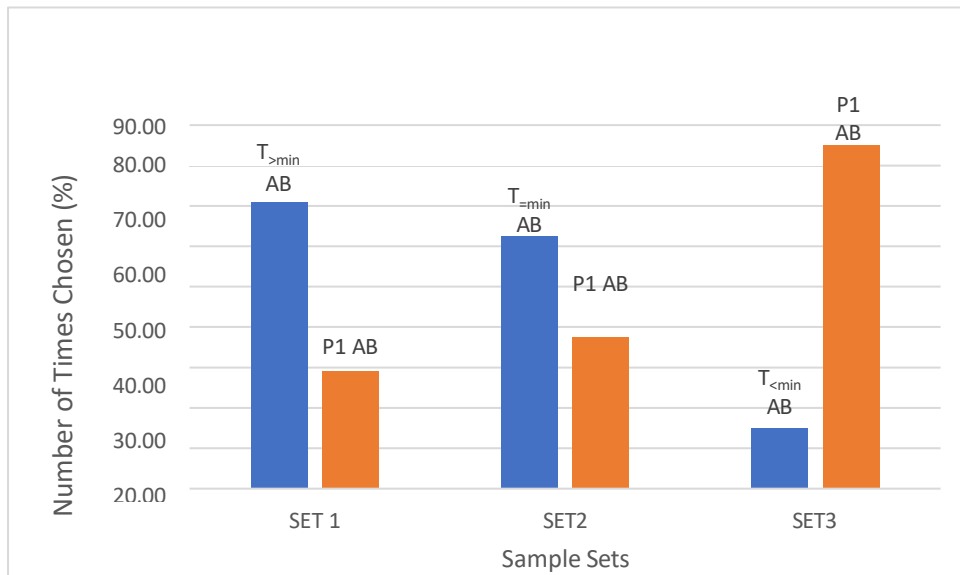


Figure 6. 11: Variation in presence/absence of texture, textured versus plain (as-built, different design).

The next set of attractiveness assessment (Batch 2) compared textured surfaces to as-built plain surfaces to assess the effect of presence or absence of texture on the perceived surface attractiveness. Figure 6. 11 illustrates the results, and it is noticeable that the textured samples T_{>min} - AB and T_{=min} - AB score significantly higher (60-70%) in attractiveness compared with plain surface AB. This may be due to associating attractiveness to the presence of texture. Individual assessors commented on the textured surface using adjectives such as interesting and stimulating, while the plain surfaces were described as rough, inconsistent, and boring. Interestingly, for the texture T_{<min}, the plain surface was selected 70% of the time. This suggest again that this was due to the texture dimensions being below the machine/material capability, which would result in build defects. The textured surface T_{<min} was described as non-uniform and rough compared to the plain surface

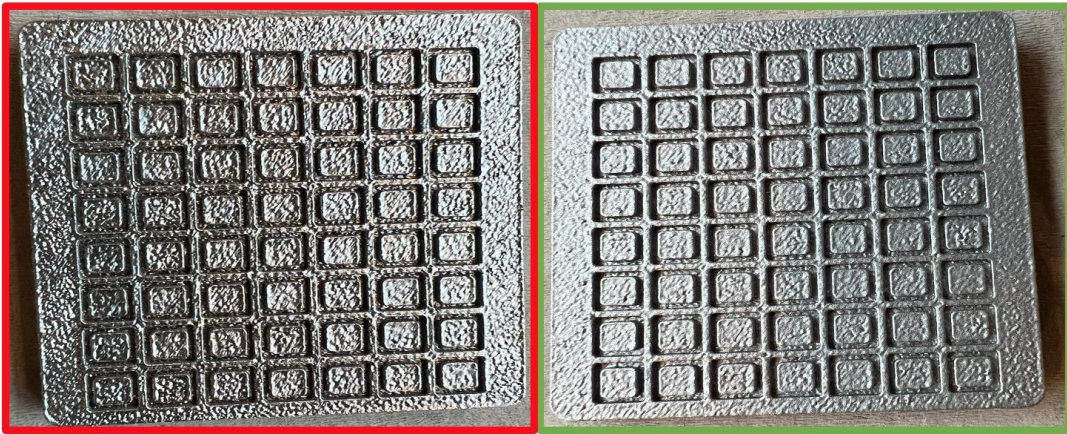


Figure 6. 12: Photographs of As Built (red) and Bead blasted Sample (green) illustrating the difference surface homogeneity and lightness.

6.7.1.1 Textured vs Plain surfaces (polished)

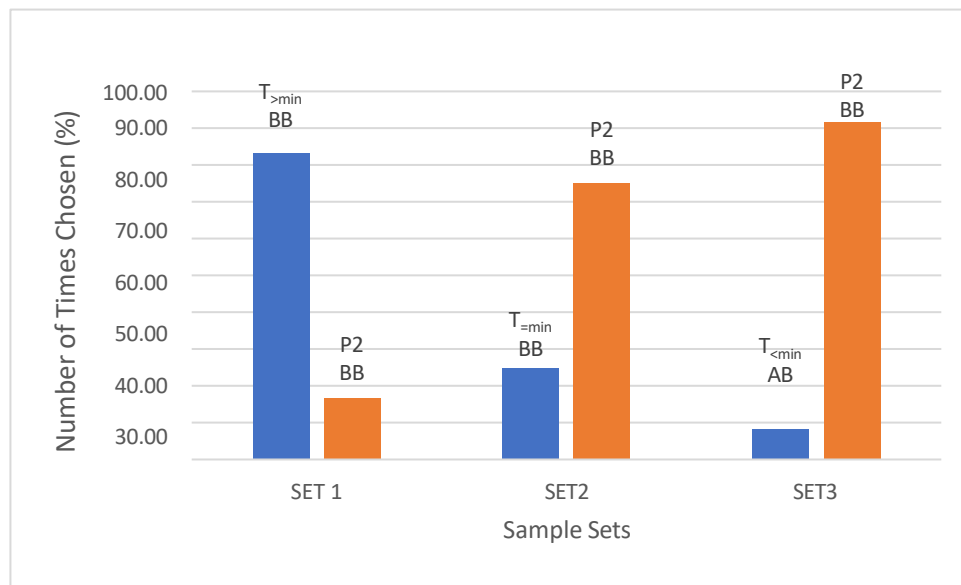


Figure 6. 13: Variation in presence/absence of texture, textured verses plain (bead blasted, different design).

Similar to section 6.4.3.1, three sets of samples (Batch 3) were assessed to compare the effect of presence/absence of texture on the attractiveness perception of bead blasted surfaces. illustrates the results from this assessment. It is noticeable that the textured samples T_{>min} - BB score significantly higher (over 83%) in attractiveness compared with the polished plain surface. This is like the score for T_{>min} - AB sample vs Plain – AB as shown in Figure 5.11. This shows that a texture designed with features significantly above the machine capability can safely be polished as the texture remain, bringing its aesthetic improvement characteristics.

For the T_{=min} - BB vs Plain – BB set, the polished plain surface scored significantly higher in attractiveness compared with T_{=min} – BB. Thus, while the T_{=min} - AB appeared more attractive than a Plain – BB, this new result suggests that as the texture

was built on the edge of the machine/material capabilities (creating the smallest feature that would be visible,) using a polishing process result in damaging the texture and makes it less attractive. Similarly, for $T_{<min}$ – BB vs Plain – BB sample set, the plain surface scored significantly higher (91%) compared to the surface textured. The texture being below machine/material capability and the polishing step is not able to improve the surface keeping it less attractive than a plain polished surface.

6.7.2 Tactile assessment (Pleasant Attribute)

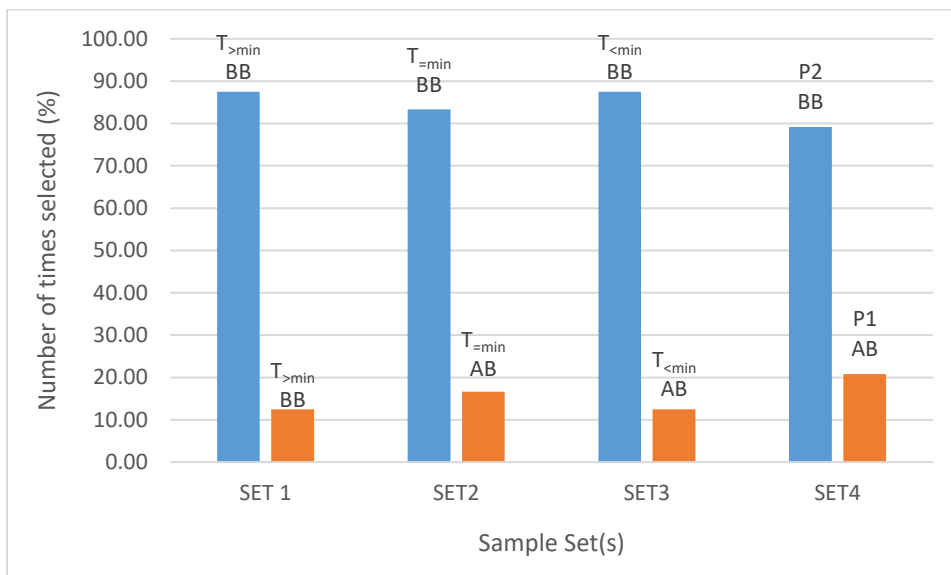


Figure 6. 14: Variation in pleasantness attribute, as-built verses bead blasted.

The aim of the pleasant attribute assessment was to determine whether post processing significantly influences the tactile perception of the surface compared to as-built surface. It is expected that the bead blasting process will improve the tactile perception of the surface due to the smoothening effect of the blasting process. As illustrated in Figure 5-9, it can be noticed that bead blasted samples were often selected as being pleasant to touch. Sample $T_{>min}$ - BB is selected 87.5% of the time while the as-built surface, $T_{>min}$ – AB is selected 12.5% of the time. Sample $T_{=min}$ follows a similar trend where $T_{=min}$ - BB is selected 83.3% of the time while $T_{=min}$ - AB is selected 16.7% of the time. In addition, bead blasted sample $T_{<min}$ - BB is chosen 87.5% compared to the as-built counterpart $T_{<min}$ – AB, which is selected 12.5% of the time. Similarly, the bead blasted plain surface is selected 79.2% of the time and the plain as-built surface

is selected 20.8% of the time. As expected, the bead blasted samples score higher in tactile perception compared to as-built surfaces.

6.7.3 Visio-Tactile assessment: Preference Attribute

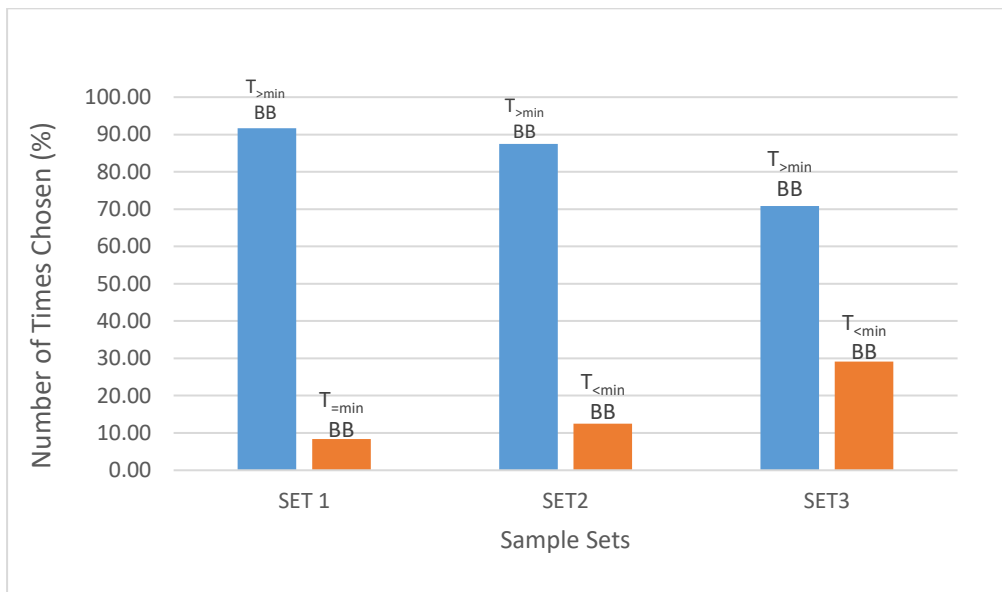


Figure 6. 15: Assessment of preference attribute (bead blasted, different design)

The aim of the assessment was to determine the influence of texture size on the perceived preference ranking of textured surfaces. The preference attribute was assessed by both by vision and touch perception. The results in Figure 6. 15 show that when compared to $T_{=min}$ - BB and $T_{<min}$ - BB, $T_{>min}$ - BB was always preferred by assessors 85-90% of the time (Set 1 and Set 2). In Set 3 assessment, $T_{=min}$ - BB was preferred 70% of the time compared to $T_{<min}$ - BB which was preferred 30% of the time.

This is accordance to previous findings. The $T_{<min}$ - BB texture being built below the machine capabilities; it does not bring adequate aesthetic properties. Regarding the $T_{=min}$ - BB texture, as suggested previously it appears that the texture aesthetic characteristic was damaged by the polishing process, as the $T_{=min}$ - AB texture generally performed well in other assessments. This finding was not available when this experiment was setup. Future assessments would be required to compare in more details the as built textures $T_{=min}$ - AB with $T_{<min}$ - AB and $T_{<min}$ - BB. However, the findings were still enabling the completion of the goals chapter.

6.8 Discussion

A total of 100 pairwise comparisons were made from 25 selected individual participants.

For the perceived ranking by vision (attractive attribute), the results suggest that post processing did not have a significant impact on the assessment of $T > \text{min}$ and $T < \text{min}$. However, $T = \text{min}$ the as-built surface was preferred and for plain samples, the bead blasted surface was preferred. This may be because of the following reasons.

During the visual assessment for set 1 and set 3 some assessors gave the reason for selecting the as-built surface as that they find shiny surfaces more attractive than matt, whereas those who selected the matt surfaces stated personal preference for matt surfaces over shiny ones. $T = \text{min} - \text{BB}$ sample shows a groove on the top right corner of the surface. This defect was also present on $T = \text{min} - \text{AB}$ but was disguised by the texture hence less visible on the as-built surface $T = \text{min} - \text{AB}$. This result supports the theory that indeed, $T = \text{min}$ texture as manufactured at the minimum machine and material capability hence any post processing technique such as bead blasting (which removes additional material) can reduce the feature sizes below the limit of the machine essentially minimising the aesthetic characteristics of the texture. This reduces the surface texture's capability to disguise any surface irregularities which may be present on the LPBF surface.

Also, the results on attractiveness perception (with variation in design) indicates that textured surfaces are always preferred to as-built plain surfaces except for $T < \text{min}$. As seen in Figure 5-11, the plain surface is preferred 70% more than $T < \text{min}$. This suggests that texture definitions (feature spacing and width) were indeed below machine capability and are likely to result in surface irregularities which defeats the purpose of texturing for aesthetics. These results seem to validate the tool developed in previous chapters as it provides an estimation of feature sizes that should ensure that a texturing size is at or above machine or material capability for a desired visual surface perception.

Furthermore, the bead blasted samples scored higher in tactile perception compared to as-built surfaces. This was expected because the bead blasting process reduces

the surface peaks and visibly smoothens the surface as shown in Figure 6. 6D- Figure 6. 9D. This is similar to results by (Galimberti *et al.*, 2016), where bead blasted surfaces scored highest in tactile perception.

These results should be considered when designing textured aircraft interior surfaces for which tactile customer interaction is of paramount importance for example tablet bezels or tray tables.

Finally, the perceived ranking by preference attribute (visuo-tactile) further supports the theory that surface texturing at, or above machine/material capability improves the visuo-tactile perception of LPBF components.

6.9 Conclusion

This chapter has presented the aesthetic evaluation of textured LPBF surfaces to assess whether an aesthetically pleasing texture can be made with feature sizes manufactured at the minimum machine and material capability. The samples were designed based on the analytical approaches developed in the previous chapters, with the aim of validating the methods introduced in Chapter 4 and Chapter 5. From the evaluation, surfaces which were textured with the minimum feature width were found to be more attractive compared to textures below minimum and plain surfaces. Hence, the texture geometry has an impact on the aesthetic evaluation of the surface.

In summary, small textures below machine capability, $T < \text{min}$, have been proven to generally perform poorly since the features are designed below the machine material capability. For textures designed to the machine and material limit, $T = \text{min}$, any reductive or subtractive post processing technique reduces the texture size below the machine and material limit, hence minimizing the aesthetic effect. On the other hand, feature sizes built above the machine and material limit can benefit aesthetically from a variety of post processing techniques. This is new knowledge which can be beneficial for overall texturing design guidelines.

The results from this experiment provide useful information about how the perceived appearance is influenced by the surface texture. The main limitation of this experiment is that it applies mainly to the texture geometry explored and to the machine, material and build strategy used as well as post processing. Hence, the results from this experiment cannot be generalised for different texturing and post processing combinations.. For future work, other texture types can be explored, with different post processing techniques, such as chemical polishing, to develop a texturing database.

Nonetheless, the results can provide valuable information for exploring the aesthetic properties of new metal LPBF textures. The 2AFC test may not be ideal for experienced assessors in instances where they think two samples are very similar. Hence, including a no preference option in future experiments may provide information

on which products the assessors have no preference for, particularly with more experienced individual assessors.

Future work can also focus on engineering feeling into texture for example by varying feature width and spacing to provide similar tactile feeling to common textures such as leather or marble surfaces. Also, extending the experimental analysis to find the correlation between the assessment scores and surface objective parameters will be an interesting way forward.

7 Conclusion and Future Work

7.1 Thesis Summary

The aim of the thesis was to develop method(s) to assist with the prediction of the feasibility and aesthetic characterisation of direct textures manufactured by Laser Powder Bed Fusion (LPBF). To achieve this aim, the objectives of the thesis were as follows:

- The development of a quick assessment approach for determining which surface features can be manufactured, based on the technology capability (e.g., the machine and material combination).
- Proposal of an approach for determining the minimum measurable spacing between two adjacent features for a specified design feature depth.
- Assessment of whether an aesthetically pleasing texture can be created by combining the smallest feasible feature sizes (width and spacing) that a machine can produce to generate a texture.

As highlighted in the literature review, there is a gap in the understanding of how directly produced surface textures influence the aesthetic perception of an LPBF surface. Also, the availability of support tools to better inform and assist designers in the production of aesthetic textured surfaces was lacking in the current state of the art.

From Chapter 4, the Rosenthal equation was initially used to analytically predict the melt-pool width for a given machine and material combination. From the initial experiments, it was found that the original Rosenthal equation under predicts the experimental feature width hence the need for tuning to reduce the generally high prediction error. The results after tuning showed that the L-BFGS optimisation algorithm can indeed improve the prediction accuracy of the Rosenthal equation by modifying the machine parameters with certain coefficients. These coefficients were

unique to a particular machine or material combination; however, the overall approach and analytical model is transferrable for either PWM laser or Continuous laser.

From Chapter 5, the sum of squared ratios was modified to predict which combination of feature height and design spacing will yield a measurable spacing, assuming that a measurable spacing will ultimately be visible to the observer of the surface macro texture. For the range of experimental feature height (25-300 μm), 4% of the sum of squared ratios were less than 1 hence implying that for such combinations of feature height, a design spacing of greater than 0.4mm will result in a measurable hence visible spacing. The extracted profiles confirmed that the green region (sum of squared ratios greater than 1) showed measurable spacing whereas the red region (sum of squared ratios less than 1) showed indistinguishable spacing from the plain surface texture.

From Chapter 6, LPBF surface textures were aesthetically evaluated by 25 individuals with the objective of assessing whether an aesthetically pleasing texture can be fabricated using feature sizes manufactured at the minimum machine and material capability. The contributions from Chapter 4 and Chapter 5 were used as the basis of the sample designs. The results from the individual surface evaluation showed that surfaces which were textured with the minimum feature width were more attractive in comparison with textures below minimum and plain surfaces. Therefore, this validates the impact of texture geometry on the overall aesthetic evaluation of the direct textured surface. It was also found that aesthetic surfaces can be produced with at the machine and material limit, however, the use of post processing techniques (subtractive) can impact the aesthetic texturing effect by reducing the texture sizes to below the minimum machine and material capability.

7.2 Contributions to the field

This section summarises the key contributions to knowledge of each chapter within this thesis.

7.2.1 Literature review contributions

The following findings were made based on the literature review (Chapter 2) which are in line with the overall aim and objectives of this thesis.

- Compared to other metal AM techniques, LPBF offers better surface quality, dimensional accuracy, and part complexity.
- The plain surface textured of LPBF parts are often characterised by surface irregularities and partially bonded particles.
- There are various techniques for measuring and characterising the plain surface texture, however this required validation from an aesthetic perspective.
- By understanding and improving the aesthetic quality of textured surfaces made by LPBF, it is possible that the adoption of the technology in aircraft interiors can be accelerated.

7.2.2 Chapter 4's contribution

For Chapter 4, the main contribution is a quick analytical model developed, optimised, and validated to determine, for a particular machine and material combination, the minimum feature width. This meets the first objective which is to develop a quick assessment approach for determining which surface features can be manufactured, based on the technology capability (e.g., the machine and material combination).

7.2.3 Chapter 5's contribution

The main contribution from this Chapter is the analytical approach using the sum of squared ratios which can be applied by designers to determine whether a combination of feature depth and design spacing will yield a measurable, hence visible spacing. This Chapter meets the second objective which is the proposal of an approach for determining the minimum measurable spacing between two adjacent features for a specified design feature depth.

7.2.4 Chapter 6's contribution

For Chapter 6, the main contribution is the validation of the analytical approaches presented in Chapters 3 and 4 by assessing custom designed textures in the context of aesthetics.

This meets the third objective of the thesis, which is the assessment of whether an aesthetically pleasing texture can be created by combining the smallest feasible feature sizes (width and spacing) that a machine can produce to generate a texture.

7.2.5 Final concluding remarks

In conclusion, this thesis has demonstrated the following:

- Textures can improve the aesthetic perception of a surface.
- Textures can be directly fabricated within machine and material limits.
- Development of methods for determining practical limits of a given machine and material combination.

7.3 Recommendation for future work

The following recommendations for future work have been outlined by chapter to build on the aims and objectives of this thesis.

- For future work relating to Chapter 4, it will be worthwhile to investigate the impact of build position on geometric precision and accuracy of small features produced by LPBF. This will be an important step for moving towards serial production of parts.
- For Chapter 5, a recommendation for future work will be to analyse the impact of variation in melt pool width and depth on the measurable feature spacing. In addition, it will be beneficial to investigate how the impact of balling effect can be accounted for within the sum of squared ratios and on the measurability of the feature spacing
- The recommendation for Chapter 6 is to include more response options for example the no preference option in the aesthetic characterisation process as this may highlight further aspects of the texture prediction approach which may improve the design of aesthetic textures. In addition, it will be interesting to analyse the correlation between the assessment scores and surface objective parameters in the future.
- Relating to Chapters 4-6, future work on direct texturing can also focus on engineering feeling into texture for example by varying feature width and spacing to provide similar tactile feeling or visual perception to common textures such as leather or marble surfaces.
- In the future, it will be beneficial to develop a user interface where the user requirements are fed in as inputs and the tuned or optimised coefficients are produced as outputs.

8 References

Abele, E. and Kniepkamp, M. (2015) 'Analysis and optimisation of vertical surface roughness in micro selective laser melting', *Surface Topography: Metrology and Properties*. IOP Publishing Ltd, 3(3). doi: 10.1088/2051- 672X/3/3/034007.

Adobe (2020) *Substance & 4D_Additive Texture 3D Prints for Industry*. Available at: https://substance3d.adobe.com/magazine/substance-4d_additive-texture-3d-prints-for-industry/.

Ahluwalia, K., Mediratta, R. and Yeo, S. H. (2017) 'A novel approach to vibratory finishing: Double vibro-polishing', *Materials and Manufacturing Processes*. doi: 10.1080/10426914.2016.1232812.

Ahmed, N., Abdo, B.M., Darwish, S., Moiduddin, K., Pervaiz, S., Alahmari, A.M. and Naveed, M. (2017). Electron beam melting of titanium alloy and surface finish improvement through rotary ultrasonic machining. *The International Journal of Advanced Manufacturing Technology*, 92(9-12), pp.3349–3361. doi:<https://doi.org/10.1007/s00170-017-0365-3>.

AMFG (2019) 'The Additive Manufacturing Landscape 2019 Key Trends and Analyses'.

Armillotta, A. (2006) *Assessment of surface quality on textured FDM prototypes*, *Rapid Prototyping Journal*.

Armillotta, A. (2019) 'Direct texturing for additive manufacturing: software support and build tests', *Rapid Prototyping Journal*, 26(5), pp. 881–894. doi: 10.1108/RPJ-03-2019-0070.

Atzeni, E. and Salmi, A. (2012) 'Economics of additive manufacturing for end-useable metal parts', *International Journal of Advanced Manufacturing Technology*, 62(9–12), pp. 1147–1155. doi: 10.1007/s00170-011-3878-1.

Bagehorn, S., Wehr, J. and Maier, H. J. (2017) 'Application of mechanical surface finishing processes for roughness reduction and fatigue improvement of additively manufactured Ti-6Al-4V parts', *International Journal of Fatigue*. doi: 10.1016/j.ijfatigue.2017.05.008.

Bahnini, I., Rivette, M., Rechia, A., Siadat, A. and Elmesbahi, A. (2018). Additive manufacturing technology: the status, applications, and prospects. *The International Journal of Advanced Manufacturing Technology*, 97(1-4), pp.147–161. doi:<https://doi.org/10.1007/s00170-018-1932-y>.

Baker, R. (1925) 'Method of making decorative article', *United States Patent Office*, 28(2), pp. 131–134.

Bhaduri, D., Penchev, P., Batal, A., Simeonov Dimov, S., Leung Soo, S., Sten, S., Harrysson, U., Zhang, Z. and Dong, H. (2017). Laser polishing of 3D printed mesoscale components. *Applied Surface Science*, 405, pp.29–46. doi:<https://doi.org/10.1016/j.apsusc.2017.01.211>.

Bhatta, S.R., Tiippana, K., Vahtikari, K., Hughes, M. and Kyttä, M. (2017). Sensory and Emotional Perception of Wooden Surfaces through Fingertip Touch. *Frontiers in Psychology*, 8. doi:<https://doi.org/10.3389/fpsyg.2017.00367>.

Blakey-Milner, B., Gradl, P., Snedden, G., Brooks, M., Pitot, J., Lopez, E., Leary, M., Berto, F. and du Plessis, A. (2021). Metal additive manufacturing in aerospace: A review. *Materials & Design*, [online] 209, p.110008. doi:<https://doi.org/10.1016/j.matdes.2021.110008>.

Blanther, J. E. (1892) 'Manufacture of contour relief maps', *United States Patent*, (473), pp. 2–4.

Boban, J., Ahmed, A., Rahman, M.A. and Rahman, M. (2020). Wire electrical discharge polishing of additive manufactured metallic components. *Procedia CIRP*, 87, pp.321–326. doi:<https://doi.org/10.1016/j.procir.2020.02.023>.

Bordatchev, E. V, Hafiz, A. M. K. and Remus Tutunea-Fatan, O. (no date) 'Performance of laser polishing in finishing of metallic surfaces'. doi: 10.1007/s00170-014-5761-3.

Boschetto, A., Bottini, L., Macera, L. and Veniali, F. (2020). Post-Processing of Complex SLM Parts by Barrel Finishing. *Applied Sciences*, 10(4), p.1382. doi:<https://doi.org/10.3390/app10041382>.

Boucher, C. (2019) *Thermal Diffusivity-An overview*. Available at: <https://thermtest.com/thermal-diffusivity-overview> (Accessed: 18 August 2021).

Brown, C. U., Jacob, G., Possolo, A., Beauchamp, C., Peltz, M., Stoudt, M., and Donmez, A. (2018) 'The Effects of Laser Powder Bed Fusion Process Parameters on Material Hardness and Density for Nickel Alloy 625', *NIST Advanced Manufacturing Series*, pp. 100–119. doi: 10.6028/NIST.AMS.100-19.

BS 1134 (2010) 'Assessment of Surface Texture - Guidance and General Information', *BSI Standards Publication*, BS, p. 1134:2010.

Buchanan, C. and Gardner, L. (2019) 'Metal 3D printing in construction: A review of methods, research, applications, opportunities and challenges', *Engineering Structures*. doi: 10.1016/j.engstruct.2018.11.045.

Byrd, R. H. *et al.* (1995) 'A Limited Memory Algorithm for Bound Constrained Optimization', *SIAM Journal on Scientific Computing*, 16(5), pp. 1190–1208. doi: 10.1137/0916069.

Chatterjee, B. (2015) 'Science and industry of electropolishing', *Galvanotechnik*, 71(1), pp. 71–93.

Chen, Z., Wu, X., Tomus, D. and Davies, C.H.J. (2018). Surface roughness of Selective Laser Melted Ti-6Al-4V alloy components. *Additive Manufacturing*, 21, pp.91–103. doi:<https://doi.org/10.1016/j.addma.2018.02.009>.

Chi Ma, Mohsen Taheri Andani, Haifeng Qin, N. S. M. *et al.* (2017) 'Improving surface finish and wear resistance of additive manufactured nickel-titanium by ultrasonic nano-crystal surface modification', *Journal of Materials Processing Tech*, pp. 433–440. doi: 10.1016/j.jmatprotec.2017.06.038.

Das, S., Bourell, D. L. and Babu, S. S. (2016) 'Metallic materials for 3D printing', *MRS Bulletin*, 41(10), pp. 729–741. doi: 10.1557/mrs.2016.217.

Diaz, A. (2019) 'Surface texture characterization and optimization of metal additive manufacturing-produced components for aerospace applications', in *Additive Manufacturing for the Aerospace Industry*. Elsevier, pp. 341–374. doi: 10.1016/b978-0-12-814062-8.00018-2.

DiMatteo, P. (1974) 'Method of generating and constructing three- dimensional bodies', *Google Patents*, (19), p. 3. Available at: <https://patents.google.com/patent/US3932923A/en>.

Doubenskaia, M., Grigoriev, S.N., Zhirnov, I. and Smurov, I (2016). Parametric analysis of SLM using comprehensive optical monitoring. *Rapid Prototyping Journal*, 22(1), pp.40–50. doi:<https://doi.org/10.1108/rpj-04-2014-0046>.

Eres, M. H. *et al.* (2014) 'Mapping customer needs to engineering characteristics: an aerospace perspective for conceptual design', *Journal of Engineering Design*, 25(1–3), pp. 64–87. doi: 10.1080/09544828.2014.903387.

Eriksson, L., Rosen, B. G. and Bergman, M. (2018) 'Affective surface engineering- using soft and hard metrology to measure the Sensation and perception in surface properties', *Proceedings of NordDesign: Design in the Era of Digitalization, NordDesign 2018*.

Fu, W., Zhou, X. and Xue, C. (2019) *Analysis of Correlation Between Surface Roughness of Aluminum Alloy and Human Psychological Perception, Advances in Intelligent Systems and Computing*. Springer International Publishing. doi: 10.1007/978-3-030-27928-8_20.

Fujisaki, W., Tokita, M. and Kariya, K. (2015) 'Perception of the material properties of wood based on vision, audition, and touch', *Vision Research*. Elsevier Ltd, 109(PB), pp. 185–200. doi: 10.1016/j.visres.2014.11.020.

Galimberti, G., Guagliano, M., Previtali, B., and Rampino, L. (2015) 'Digital aesthetic of new products obtained by selective laser melting process', *Proceedings of the International Conference on Engineering Design, ICED*, 4(DS 80-04), pp. 193–202.

Galimberti, G., Doubrovski, Z., Guagliano, M., Previtali, B., and Verlinden, J. (2016). 'Investigating the Links between Process Parameters and Their Influence on the Aesthetic Evaluation of Selective Laser Melted Parts 1', *Proceedings of the 27th Annual International Solid Freeform Fabrication Symposium*, (November), pp. 2367–2386. Available at: <https://www.researchgate.net/publication/310152515>.

Galovskyi, B. *et al.* (2013) 'Systematic form deviations of additive manufactured parts- methods of their identification and correction', pp. 1–5.

Ghazy, M. M. (2012) 'Development of an Additive Manufacturing Decision Support System (AMDSS) A thesis submitted to the Faculty of Science , Agriculture and Engineering for the Degree of Doctor of Philosophy By School of Mechanical and Systems Engineering', (October), pp. 1–17. Available at: <https://theses.ncl.ac.uk/dspace/handle/10443/1692>.

Gillespie, L. (2007) *Mass Finishing Handbook*. First Edit. New York: Industrial Press Inc.

Gnanavel, C., Saravanan, R., Chandrasekaran, M. and Pugazhenthii, R. (2017). Restructured review on Electrical Discharge Machining - A state of the art. *IOP Conference Series: Materials Science and Engineering*, 183, p.012015. doi:<https://doi.org/10.1088/1757-899x/183/1/012015>.

Guo, D., Zhang, P., Jiang, Y., Song, C., Tan, D. and Yu, D. (2022). Effects of surface texturing and laminar plasma jet surface hardening on the tribological behaviors of GCr15 bearing steel. *Tribology International*, 169, p.107465. doi:<https://doi.org/10.1016/j.triboint.2022.107465>.

Guyson (2020) *Blast Media Data Sheet*. Available at: [Guyson Abrasive Blast Media](#). (Accessed: 14th December 2023)

Guyson (2023) *Formula 1600 - Bead Blast Machine*. Available at: <https://www.guyson.co.uk/finishing-equipment/manual-blast-machines/light-industrial-blast-machines-formula/formula-1600-bead-blast-machine> (Accessed: 26 January 2023).

Hackel, L., Rankin, J.R., Rubenchik, A., King, W.E. and Matthews, M. (2018). Laser peening: A tool for additive manufacturing post-processing. *Additive Manufacturing*, 24, pp.67–75. doi:<https://doi.org/10.1016/j.addma.2018.09.013>.

Han, W. and Fang, F. (2019) 'Fundamental aspects and recent developments in electropolishing', *International Journal of Machine Tools and Manufacture*. doi: 10.1016/j.ijmachtools.2019.01.001.

Hong, Y., Zhang, P., Lee, K.-H. and Lee, C.-H. (2017). Friction and wear of textured surfaces produced by 3D printing. *Science China Technological Sciences*, 60(9), pp.1400–1406. doi:<https://doi.org/10.1007/s11431-016-9066-0>.

ISO-4288 (1998) *Geometric Product Specification (GPS) — Surface texture— Profile method : Rules and procedures for the assessment of surface texture*.

ISO25178-3 (2012) '25178-3: Geometrical product specifications (GPS) — Surface texture : Areal Part 3 : Specification operators'.

Jain, V. K. (2008) 'Abrasive-based nano-finishing techniques: An overview', *Machining Science and Technology*, 12(3), pp. 257–294. doi: 10.1080/10910340802278133.

Jamal, M. and Morgan, M. (2017) 'Design Process Control for Improved Surface Finish of Metal Additive Manufactured Parts of Complex Build Geometry', *Inventions*. doi: 10.3390/inventions2040036.

Jaya Prasad, V., Sam Joshi, K., Venkata Ramana, V.S.N. and Chiranjeevi, R. (2018). Effect of Roller Burnishing on Surface Properties of Wrought AA6063 Aluminium Alloys. *Materials Today: Proceedings*, 5(2), pp.8033–8040. doi:<https://doi.org/10.1016/j.matpr.2017.11.488>.

Kattoura, M., Abhishek Telang, Mannava, S.R. and Qian, D. (2018). Effect of Ultrasonic Nanocrystal Surface Modification on residual stress, microstructure and fatigue behavior of ATI 718Plus alloy. *Materials Science and Engineering: A*, 711, pp.364–377. doi:<https://doi.org/10.1016/j.msea.2017.11.043>.

Kaynak, Y. and Kitay, O. (2019) 'The effect of post-processing operations on surface characteristics of 316L stainless steel produced by selective laser melting', *Additive Manufacturing*, 26, pp. 84–93. doi: 10.1016/j.addma.2018.12.021.

Kempen, K., Thijs, L., Van Humbeeck, J. and Kruth, J.-P. . (2014). Processing AlSi10Mg by selective laser melting: parameter optimisation and material characterisation. *Materials Science and Technology*, 31(8), pp.917–923. doi:<https://doi.org/10.1179/1743284714y.0000000702>.

Kim, J., Ji, S., Yun, Y. and Yeo, J. (2018). A Review: Melt Pool Analysis for Selective Laser Melting with Continuous Wave and Pulse Width Modulated Lasers. *Applied Science and Convergence Technology*, 27(6), pp.113–119. doi:<https://doi.org/10.5757/asct.2018.27.6.113>.

Kim, J. Du and Kim, K. D. (2004) 'Deburring of burrs in spring collets by abrasive flow machining', *International Journal of Advanced Manufacturing Technology*, 24(7–8), pp. 469–473. doi: 10.1007/s00170-002-1536-3.

Kovacı, H. and Seçer, Y. (2020) 'Improved tribological performance of AISI 316L stainless steel by a combined surface treatment: Surface texturing by selective laser melting and plasma nitriding', *Surface and Coatings Technology*. Elsevier, 400(June), p. 126178. doi: 10.1016/j.surfcoat.2020.126178.

Leach, R.K., Bourell, D., Carmignato, S., Donmez, A., Senin, N. and Dewulf, W. (2019). Geometrical metrology for metal additive manufacturing. *CIRP Annals*, 68(2), pp.677–700. doi:<https://doi.org/10.1016/j.cirp.2019.05.004>.

Lee, J. Y., Nagalingam, A. P. and Yeo, S. H. (2020) 'A review on the state-of- the-art of surface finishing processes and related ISO/ASTM standards for metal additive manufactured components', *Virtual and Physical Prototyping*. Taylor & Francis, 0(0), pp. 1–29. doi: 10.1080/17452759.2020.1830346.

Lestrangle, C. (2016) 'Effect of surface roughness on quality perception of Laser Sintered (LS) parts', (October 2016).

Li, Y., Linke, B.S., Voet, H., Falk, B., Schmitt, R. and Lam, M. (2017). Cost, sustainability and surface roughness quality – A comprehensive analysis of products made with personal 3D printers. *CIRP Journal of Manufacturing Science and Technology*, 16, pp.1–11. doi:<https://doi.org/10.1016/j.cirpj.2016.10.001>.

Li, Y.-H., Wang, B., Ma, C.-P., Fang, Z.-H., Chen, L.-F., Guan, Y.-C. and Yang, S.-F. (2019). Material Characterization, Thermal Analysis, and Mechanical Performance of a Laser-Polished Ti Alloy Prepared by Selective Laser Melting. *Metals*, 9(2), p.112. doi:<https://doi.org/10.3390/met9020112>.

Liem, A., Abidin, S. and Warell, A. (2009) 'Designers' perceptions of typical characteristics of form treatment in automobile styling', *Design & Semantics of Form and Movement*, (January 2016), pp. 144–155. Available at: [http://nuweb.northumbria.ac.uk/desform/2009/downloads/_PDFs/16_Andre Liem.pdf](http://nuweb.northumbria.ac.uk/desform/2009/downloads/_PDFs/16_Andre%20Liem.pdf).

Liu, Y., Yang, Y. and Wang, D. (2017) 'Investigation into the shrinkage in Z- direction of components manufactured by selective laser melting (SLM)', *International Journal of Advanced Manufacturing Technology*. The International Journal of Advanced Manufacturing Technology, 90(9–12), pp. 2913–2923. doi: 10.1007/s00170-016-9596-y.

Lou, S., Jiang, X., Sun, W., Zeng, W., Pagani, L. and Scott, P.J. (2019). Characterisation methods for powder bed fusion processed surface topography. *Precision Engineering*, [online] 57, pp.1–15. doi:<https://doi.org/10.1016/j.precisioneng.2018.09.007>.

Luo, S., Zhou, L., Nie, X., Li, Y. and He, W. (2019). *The compound process of laser shock peening and vibratory finishing and its effect on fatigue strength of Ti-3.5Mo-6.5Al-1.5Zr-0.25Si titanium alloy*. *Journal of Alloys and Compounds*, 783, pp.828–835. doi:<https://doi.org/10.1016/j.jallcom.2018.12.294>.

Maidin, S. Bin, Campbell, I. and Pei, E. (2012) 'Development of a design feature database to support design for additive manufacturing', *Assembly Automation*, 32(3), pp. 235–244. doi: 10.1108/01445151211244375.

Mediratta, R., Ahluwalia, K. and Yeo, S. H. (2016) 'State-of-the-art on vibratory finishing in the aviation industry: an industrial and academic perspective', *International Journal of Advanced Manufacturing Technology*. doi: 10.1007/s00170-015-7942-0.

Mekhiel, S., Koshy, P. and Elbestawi, M. A. (2021) 'Additive texturing of metallic surfaces for wetting control', *Additive Manufacturing*. Elsevier B.V., 37(August 2020), p. 101631. doi: 10.1016/j.addma.2020.101631.

Metelkova, J., Kinds, Y., Kempen, K., de Formanoir, C., Witvrouw, A. and Van Hooreweder, B. (2018). *On the influence of laser defocusing in Selective Laser Melting of 316L*. *Additive Manufacturing*, 23, pp.161–169. doi:<https://doi.org/10.1016/j.addma.2018.08.006>.

Mirkoohi, E., Seivers, D.E., Garmestani, H. and Liang, S.Y. (2019). *Heat Source Modeling in Selective Laser Melting. Materials*, 12(13), p.2052.
doi:<https://doi.org/10.3390/ma12132052>.

Mohammadi, M. and Asgari, H. (2018) 'Achieving low surface roughness AISi10Mg_200C parts using direct metal laser sintering', *Additive Manufacturing*. Elsevier B.V., 20, pp. 23–32. doi: 10.1016/j.addma.2017.12.012.

Mohammadian, N., Turenne, S. and Brailovski, V. (2018) 'Surface finish control of additively-manufactured Inconel 625 components using combined chemical-abrasive flow polishing', *Journal of Materials Processing Technology*. doi: 10.1016/j.jmatprotec.2017.10.020.

Morton, W., Green, S., Rennie, A., and Abram, Tn. (2011) 'Surface finishing techniques for SLM manufactured stainless steel 316L components', in *Innovative Developments in Virtual and Physical Prototyping*. doi: 10.1201/b11341-82.

Nakamura, M., Kikuchi, Y., Hotta, S., Fujiwara, Y. and Konoike, T. (2018). *Evaluation of the sensory roughness of some coated wood surfaces by image analysis. European Journal of Wood and Wood Products*, 76(6), pp.1571–1580.
doi:<https://doi.org/10.1007/s00107-018-1342-8>.

Newton, L., Senin, N., Smith B., and Leach, R. (2018) 'Feature-based characterisation of evolving surface topographies in finishing operations for additive manufacturing', *European Society for Precision Engineering and Nanotechnology, Conference Proceedings - 18th International Conference and Exhibition, EUSPEN 2018*, (June), pp. 489–490.

Newton, Lewis (2020) *Development of methods for measuring and characterising the surface topography of additively manufactured parts*. PhD thesis, University of Nottingham.

Newton, L., Senin, N. and Leach, R. (2018) 'Focus variation measurement of metal additively manufactured surfaces', *Proceedings - 2018 ASPE and euspen Summer Topical Meeting: Advancing Precision in Additive Manufacturing*, (July), pp. 232–237.

Ngo, T.D., Kashani, A., Imbalzano, G., Nguyen, K.T.Q. and Hui, D. (2018). Additive manufacturing (3D printing): A review of materials, methods, applications and challenges. *Composites Part B: Engineering*, [online] 143, pp.172–196. doi:<https://doi.org/10.1016/j.compositesb.2018.02.012>.

Niknam, S.A., Davoodi, B., Davim, J.P. and Songmene, V. (2017). Mechanical deburring and edge-finishing processes for aluminum parts—a review. *The International Journal of Advanced Manufacturing Technology*, 95(1-4), pp.1101–1125. doi:<https://doi.org/10.1007/s00170-017-1288-8>.

Nguyen, Q.B., Luu, D.N., Nai, S.M.L., Zhu, Z., Chen, Z. and Wei, J. (2018). The role of powder layer thickness on the quality of SLM printed parts. *Archives of Civil and Mechanical Engineering*, 18(3), pp.948–955. doi:<https://doi.org/10.1016/j.acme.2018.01.015>.

O'Regan, P. 2019. *Process capability management for selective laser melting*. PhD Thesis, Cardiff University.

Pagáč, M., Jiri, H., Jana, P., Tomas, Z., and Michal, S.. (2017) 'The study of mechanical properties stainless steel 316L after production from metal powder with using additive technology and by method selective laser melting', *METAL 2017 - 26th International Conference on Metallurgy and Materials, Conference Proceedings*, 2017- Janua, pp. 962–967.

Pradel, P., Zhu, Z., Bibb, R. and Moultrie, J. (2018). Investigation of design for additive manufacturing in professional design practice. *Journal of Engineering Design*, 29(4-5), pp.165–200. doi:<https://doi.org/10.1080/09544828.2018.1454589>.

Promoppatum, P., Yao, S.-C., Pistorius, P.C. and Rollett, A.D. (2017). A Comprehensive Comparison of the Analytical and Numerical Prediction of the Thermal History and Solidification Microstructure of Inconel 718 Products Made by Laser Powder-Bed Fusion. *Engineering*, [online] 3(5), pp.685–694. doi:<https://doi.org/10.1016/J.ENG.2017.05.023>.

Ramanakoto, M.F., Tahiana Ramanantoandro, Florent Eyma and Castanié, B. (2019). Visuo-tactile and topographic characterizations of finished wood surface quality by French consumers and industrials: acceptability thresholds for raised grain. *Annals of forest science*, 76(1). doi:<https://doi.org/10.1007/s13595-019-0807-1>.

Ramanantoandro, T., Larricq, P. and Eterradosi, O. (2014) 'Relationships between 3D roughness parameters and visuotactile perception of surfaces of maritime pinewood and MDF', *Holzforschung*, 68(1), pp. 93–101. doi: 10.1515/hf-2012-0208.

Renishaw (2001) *SS 316L-0407 powder for additive manufacturing * H-5800- 3001-03-A **.

Renishaw PLC (2015) *AlSi10Mg-0403 powder for additive manufacturing * H-5800-1061-01-B **.

Rhoades, L. (1991) 'Abrasive flow machining: a case study', *Journal of Materials Processing Tech.*, 28(1–2), pp. 107–116. doi: 10.1016/0924- 0136(91)90210-6.

Rokosz, K. and Hryniewicz, T. (2012) 'XPS MEASUREMENTS OF PASSIVE FILM FORMED ON AISI 316L SS AFTER ELECTROPOLISHING IN A MAGNETIC FIELD (MEP)'. doi: 10.2478/v10077-012-0012-5.

van Rompay, T.J.L., Finger, F., Saakes, D. and Fenko, A. (2017). 'See me, feel me': Effects of 3D-printed surface patterns on beverage evaluation. *Food Quality and Preference*, 62, pp.332–339. doi:<https://doi.org/10.1016/j.foodqual.2016.12.002>.

Rosa, B., Mognol, P. and Hascoët, J. (2015) 'Laser polishing of additive laser manufacturing surfaces', *Journal of Laser Applications*. doi: 10.2351/1.4906385.

Rotty, C., Mandroyan, A., Doche, M.-L. . and Hihn, J.Y. (2016). Electropolishing of CuZn brasses and 316L stainless steels: Influence of alloy composition or preparation process (ALM vs. standard method). *Surface and Coatings Technology*, 307, pp.125–135. doi:<https://doi.org/10.1016/j.surfcoat.2016.08.076>.

Sahay, C. and Ghosh, S. (2018) 'Understanding surface quality: Beyond average roughness (Ra)', *ASEE Annual Conference and Exposition, Conference Proceedings*, 2018-June.

Schütte, S. (2005) *Engineering Emotional Values in Product Design -Kansei Engineering in Development, Engineering*. Available at: <http://liu.diva-portal.org/smash/record.jsf?searchId=1&pid=diva2:20839>.

Senin, N., Thompson, A. and Leach, R. K. (2017) 'Characterisation of the topography of metal additive surface features with different measurement technologies', *Measurement Science and Technology*. IOP Publishing, 28(9). doi: 10.1088/1361-6501/aa7ce2.

Sensofar (2019) *Smart & SoixIn-line 3D Surface Sensors*. Available at: <https://www.sensofar.com/metrology/products/sensors/specifications/> (Accessed: 6 August 2020).

Sibanda, P., Carr, P.E., Ryan, M.J. and Bigot, S. (2019). State of the art in surface finish of metal additive manufactured parts. doi:<https://doi.org/10.3233/atde190039>.

Slant 3D (2019) *Eliminating the Layer Lines on Production 3D Printed Parts?*
Available at: <https://www.slant3d.com/slant3d-blog/eliminating-the-layer-lines-on-production-3d-printed-parts> (Accessed: 19 August 2021).

Strano, G., Hao, L., Everson, R.M. and Evans, K.E. (2013). Surface roughness analysis, modelling and prediction in selective laser melting. *Journal of Materials Processing Technology*, 213(4), pp.589–597.
doi:<https://doi.org/10.1016/j.jmatprotec.2012.11.011>.

Tan, K. L., Yeo, S. H. and Ong, C. H. (2017) 'Nontraditional finishing processes for internal surfaces and passages: A review', *Proceedings of the Institution of Mechanical Engineers, Part B: Journal of Engineering Manufacture*, 231(13), pp. 2302–2316. doi: 10.1177/0954405415626087.

Tang, M., Pistorius, P. C. and Beuth, J. L. (2017) 'Prediction of lack-of-fusion porosity for powder bed fusion', *Additive Manufacturing*. Elsevier B.V., 14, pp. 39–48. doi: 10.1016/j.addma.2016.12.001.

Tato, W., Blunt, L., Llavori, I., Aginagalde, A., Townsend, A. and Zabala, A. (2020). Surface integrity of additive manufacturing parts: a comparison between optical topography measuring techniques. *Procedia CIRP*, 87, pp.403–408.
doi:<https://doi.org/10.1016/j.procir.2020.02.082>.

Taylor Hobson (2022) 'Form Talysurf® i-Series PRO Range'. Available at: <https://www.taylor-hobson.com/products/surface-profilers/i-series-pro-range/talysurf-pro>.

Temmler, A., Willenborg, E. and Wissenbach, K. (2012) 'Laser Polishing', in. doi: 10.1117/12.906001.

Thomas, D. S. and Gilbert, S. W. (2014) 'Costs and Cost Effectiveness of Additive Manufacturing'. doi: 10.6028/NIST.SP.1176.

Townsend, A., Senin, N., Blunt, L., Leach, R.K. and Taylor, J.S. (2016). Surface texture metrology for metal additive manufacturing: a review. *Precision Engineering*, [online] 46, pp.34–47. doi:<https://doi.org/10.1016/j.precisioneng.2016.06.001>.

Townsend, A. P. (2018) 'Characterisation of the Surface Topography of Additively Manufactured Parts', *A thesis submitted to the University of Huddersfield in partial fulfilment of the requirements for the degree of Doctor of Philosophy*, (March).

Tyagi, P., Goulet, T., Riso, C. and Garcia-Moreno, F. (2018). Reducing surface roughness by chemical polishing of additively manufactured 3D printed 316 stainless steel components. *The International Journal of Advanced Manufacturing Technology*, 100(9-12), pp.2895–2900. doi:<https://doi.org/10.1007/s00170-018-2890-0>.

Verma, A. and Mahato, D. (2013) *ROLLER BURNISHING-A Literature Review of Developments and Trends in Approach to Industrial Application*, *Asian Journal of Engineering and Technology*. Available at: www.ajouronline.com.

Vijayaraghavan, V. and Castagne, S. (2018) 'Measurement of surface characteristics of Ti6Al4V aerospace engineering components in mass finishing process', *Measurement: Journal of the International Measurement Confederation*. doi: 10.1016/j.measurement.2017.10.054.

Violante, M. G., Marcolin, F., Vezzetti, E., Nonis, F., and Moos, S.(2019) *Emotional design and virtual reality in product lifecycle management (PLM)*, *Smart Innovation, Systems and Technologies*. Springer Singapore. doi: 10.1007/978-981-13-9271-9_17.

Wang, Z., Jia, Y.-F., Zhang, X.-C., Fu, Y., Zhang, C. and Tu, S.-T. (2019). Effects of Different Mechanical Surface Enhancement Techniques on Surface Integrity and Fatigue Properties of Ti-6Al-4V: A Review. 44(6), pp.445–469. doi:<https://doi.org/10.1080/10408436.2018.1492368>.

Wu, K.L., Yan, B.H., Huang, F.Y. and Chen, S.C. (2005). Improvement of surface finish on SKD steel using electro-discharge machining with aluminum and surfactant added dielectric. *International Journal of Machine Tools and Manufacture*, 45(10), pp.1195–1201. doi:<https://doi.org/10.1016/j.ijmactools.2004.12.005>.

Yang, G., Wang, B., Tawfiq, K., Wei, H., Zhou, S. and Chen, G. (2016). Electropolishing of surfaces: theory and applications. *Surface Engineering*, 33(2), pp.149–166. doi:<https://doi.org/10.1080/02670844.2016.1198452>.

Yap, C.Y., Chua, C.K., Dong, Z.L., Liu, Z.H., Zhang, D.Q., Loh, L.E. and Sing, S.L. (2015). Review of selective laser melting: Materials and applications. *Applied Physics Reviews*, [online] 2(4), p.041101. doi:<https://doi.org/10.1063/1.4935926>.

Ye, C., Zhang, C., Zhao, J. and Dong, Y. (2021). Effects of Post-processing on the Surface Finish, Porosity, Residual Stresses, and Fatigue Performance of Additive Manufactured Metals: A Review. *Journal of Materials Engineering and Performance*, 30(9), pp.6407–6425. doi:<https://doi.org/10.1007/s11665-021-06021-7>.

Yung, K.C., Wang, W.J., Xiao, T.Y., Choy, H.S., Mo, X.Y., Zhang, S.S. and Cai, Z.X. (2018). Laser polishing of additive manufactured CoCr components for controlling their wettability characteristics. *Surface and Coatings Technology*, 351, pp.89–98. doi:<https://doi.org/10.1016/j.surfcoat.2018.07.030>.

Zeithaml, V. A. (1988) 'Consumer Perceptions of Price, Quality, and Value: A Means-End Model and Synthesis of Evidence', *Journal of Marketing*, 52(3), p. 2. doi: 10.2307/1251446.

Zhang, J., Xiang Toh, A.Y., Wang, H., Lu, W.F. and Fuh, J.Y.H. (2018). Vibration-assisted conformal polishing of additively manufactured structured surface. *Proceedings of the Institution of Mechanical Engineers, Part C: Journal of Mechanical Engineering Science*, 233(12), pp.4154–4164. doi:<https://doi.org/10.1177/0954406218811359>.

Zhang, L., Zhang, S., Zhu, H., Hu, Z., Wang, G. and Zeng, X. (2018). Horizontal dimensional accuracy prediction of selective laser melting. *Materials & Design*, [online] 160, pp.9–20. doi:<https://doi.org/10.1016/j.matdes.2018.08.059>.

Zhang, L., Zhu, H., Zhang, S., Wang, G. and Zeng, X. (2019). Fabricating high dimensional accuracy LPBFed Ti6Al4V part by using bi-parameter method. *Optics & Laser Technology*, [online] 117, pp.79–86. doi:<https://doi.org/10.1016/j.optlastec.2019.04.009>.

Zhang, L., Zhang, S. and Zhu, H. (2021) 'Effect of scanning strategy on geometric accuracy of the circle structure fabricated by selective laser melting', *Journal of Manufacturing Processes*. Elsevier Ltd, 64(October 2020), pp. 907–915. doi: 10.1016/j.jmapro.2021.02.015.

Zhihao, F., Libin, L., Longfei, C. and Yingchun, G. (2018). Laser Polishing of Additive Manufactured Superalloy. *Procedia CIRP*, 71, pp.150–154. doi:<https://doi.org/10.1016/j.procir.2018.05.088>.

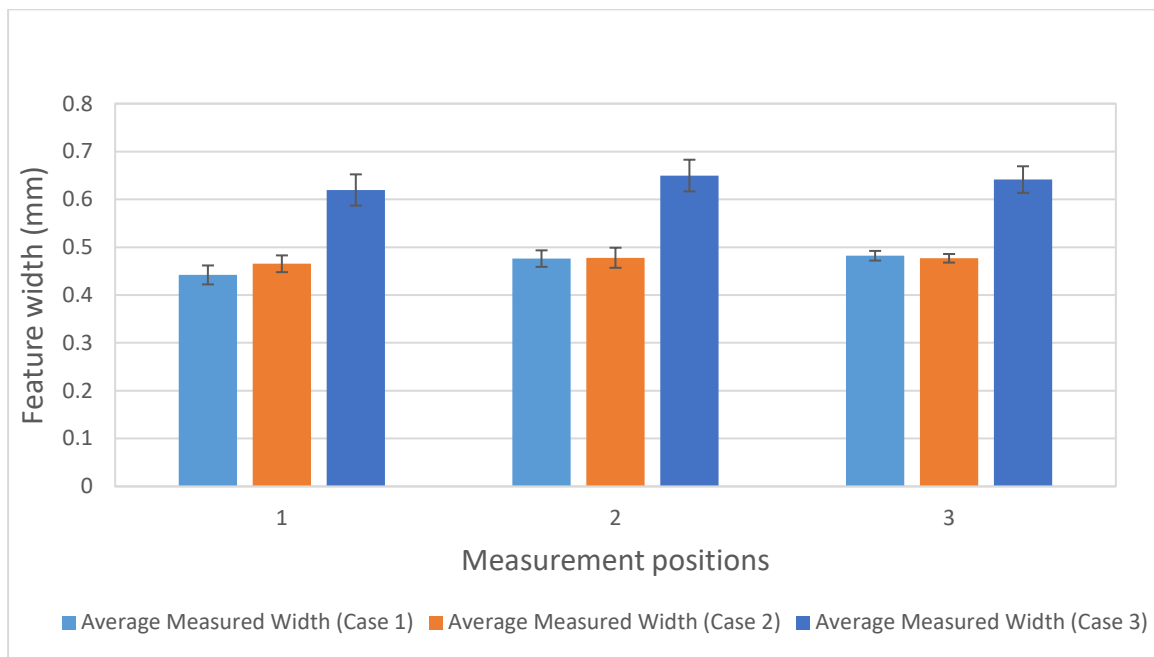
Zmarzły, P., Koziar, T. and Gogolewski, D. (2023) 'The Effect of Non- Measured Points on the Accuracy of the Surface Topography Assessment of Elements 3D Printed Using Selected Additive Technologies', *Materials*, 16(1). doi: 10.3390/ma16010460.

Zuo, H. (2010) 'The Selection of Materials to Match Human Sensory Adaptation and Aesthetic Expectation in Industrial Design', *METU Journal of Faculty of Architecture*. Middle East Technical University, Faculty of Architecture, 27(2), pp. 301–319. doi: 10.4305/metu.jfa.2010.2.17.

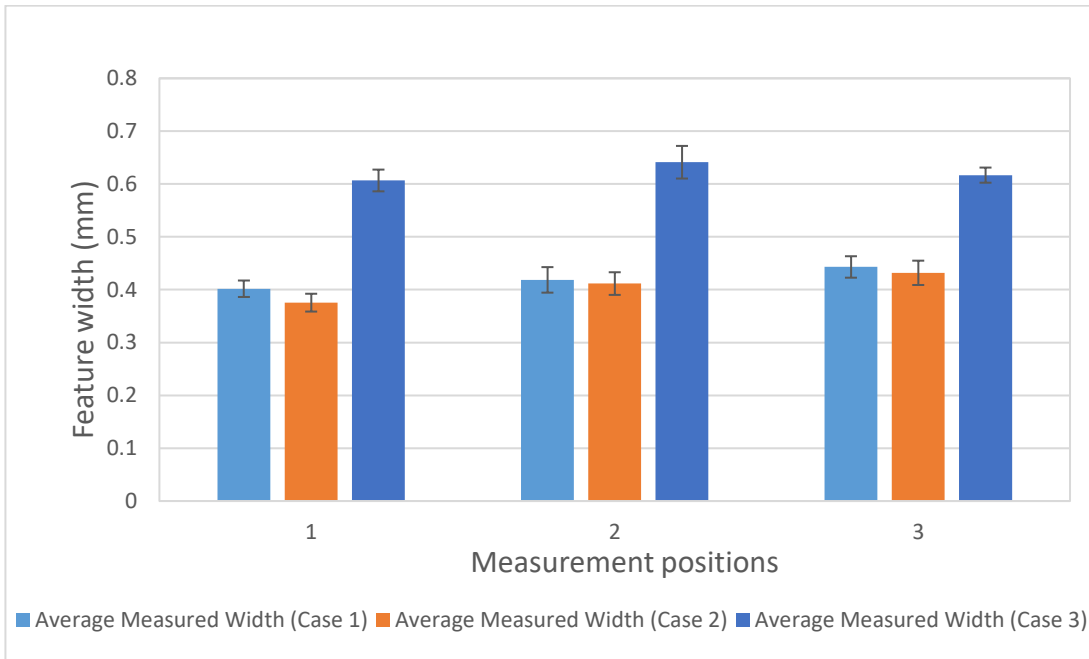
Zuo, H. and Jones, M. (2005) 'Exploration into formal aesthetics in design: (material) texture', *Design*, pp. 1–11.

9 Appendix

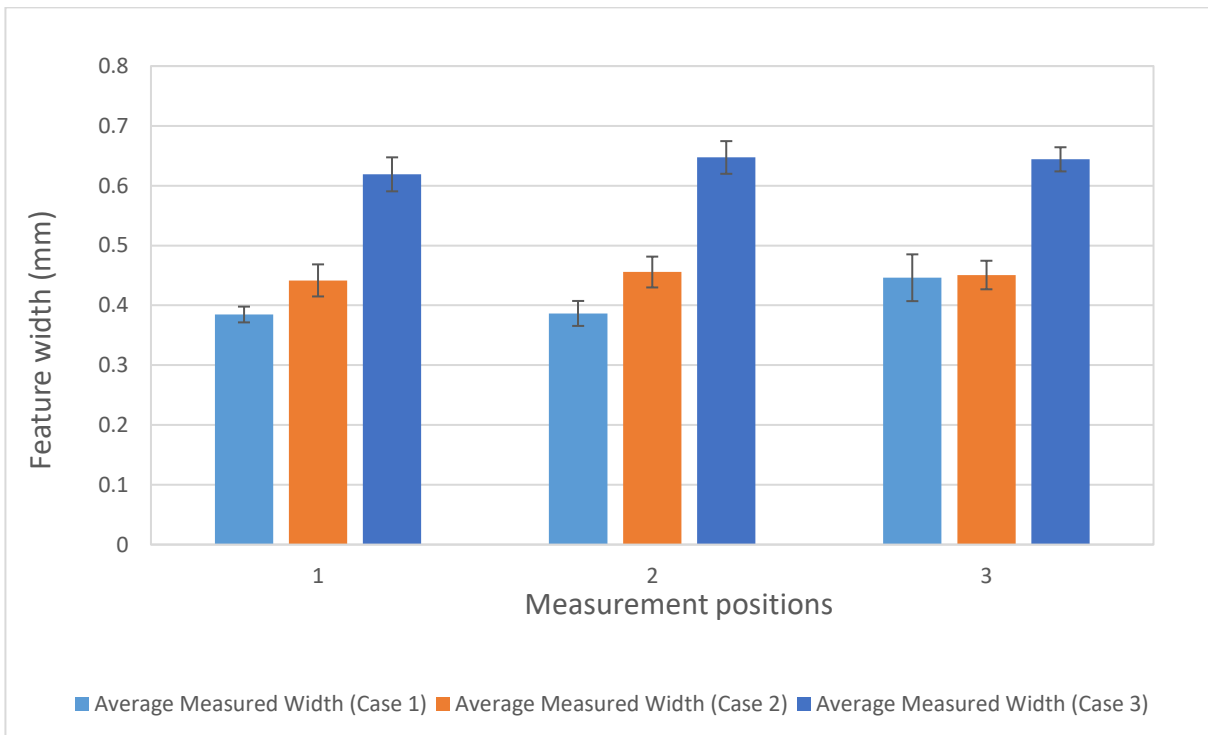
9.1 Appendix 1: Chapter 4



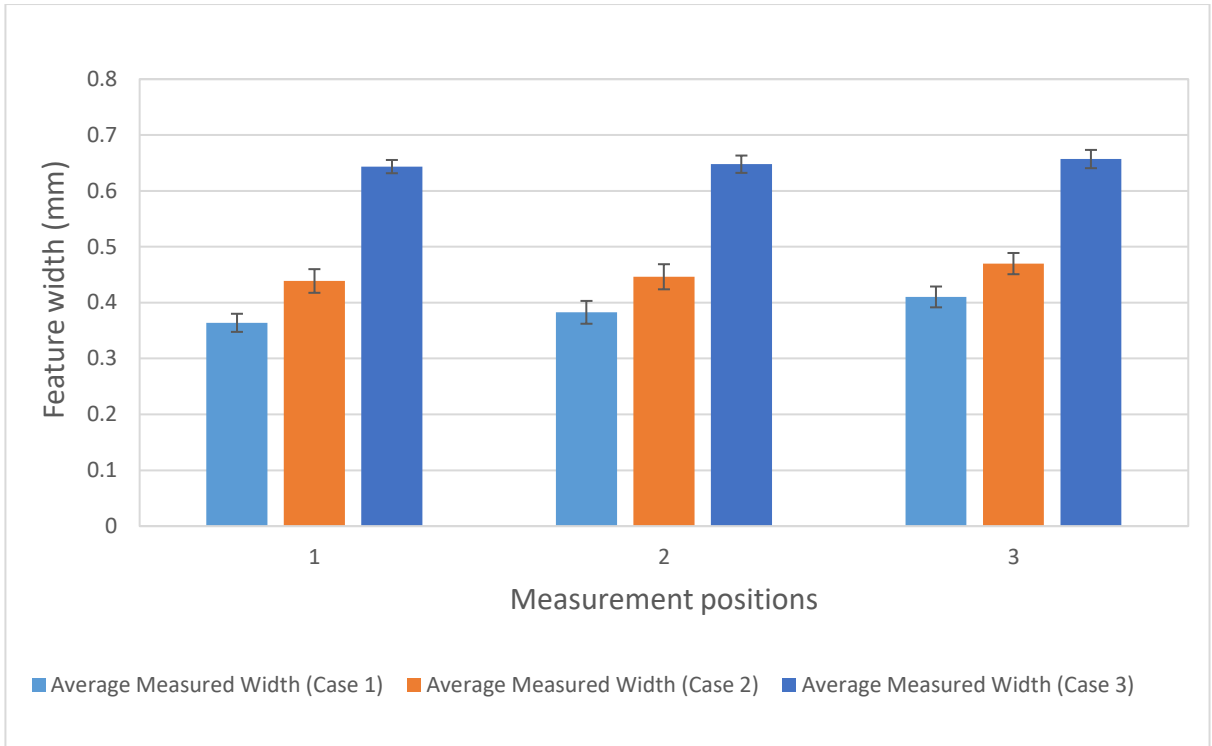
Average measured width and standard deviations for Sample 2



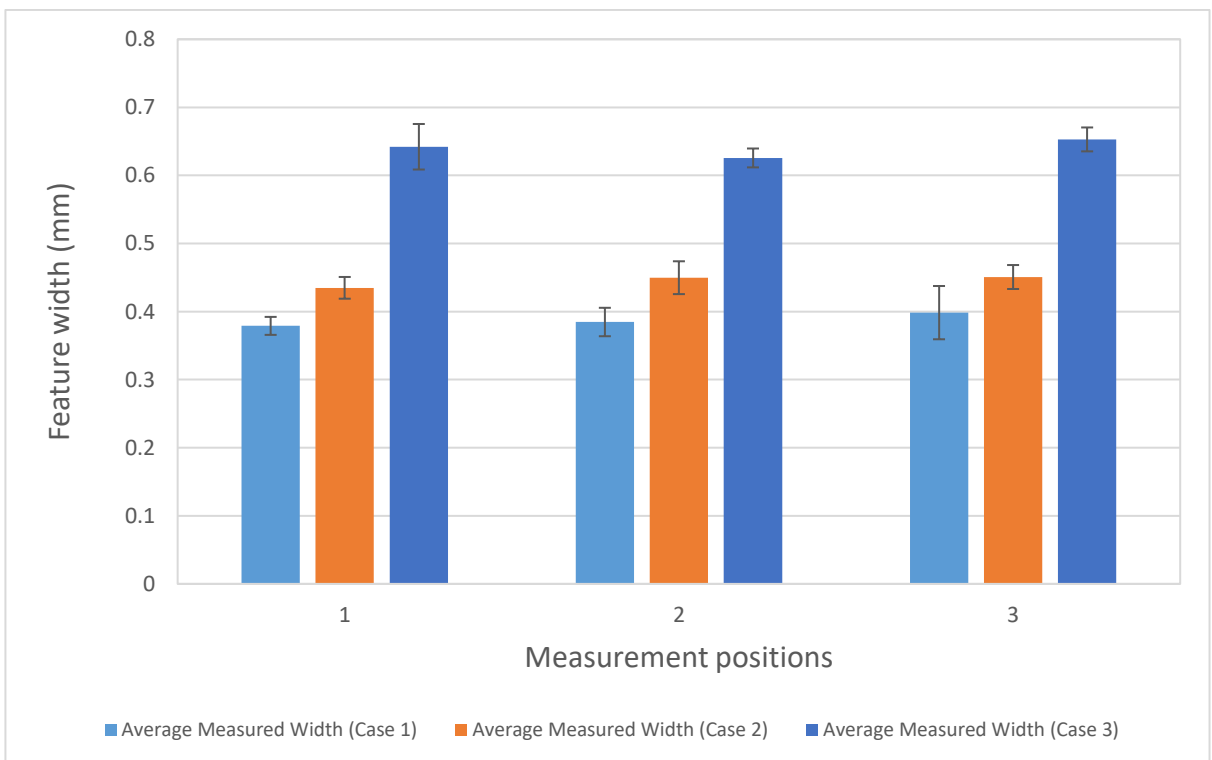
Average measured width and standard deviations for Sample 3.



Average measured width and standard deviations for Sample 4

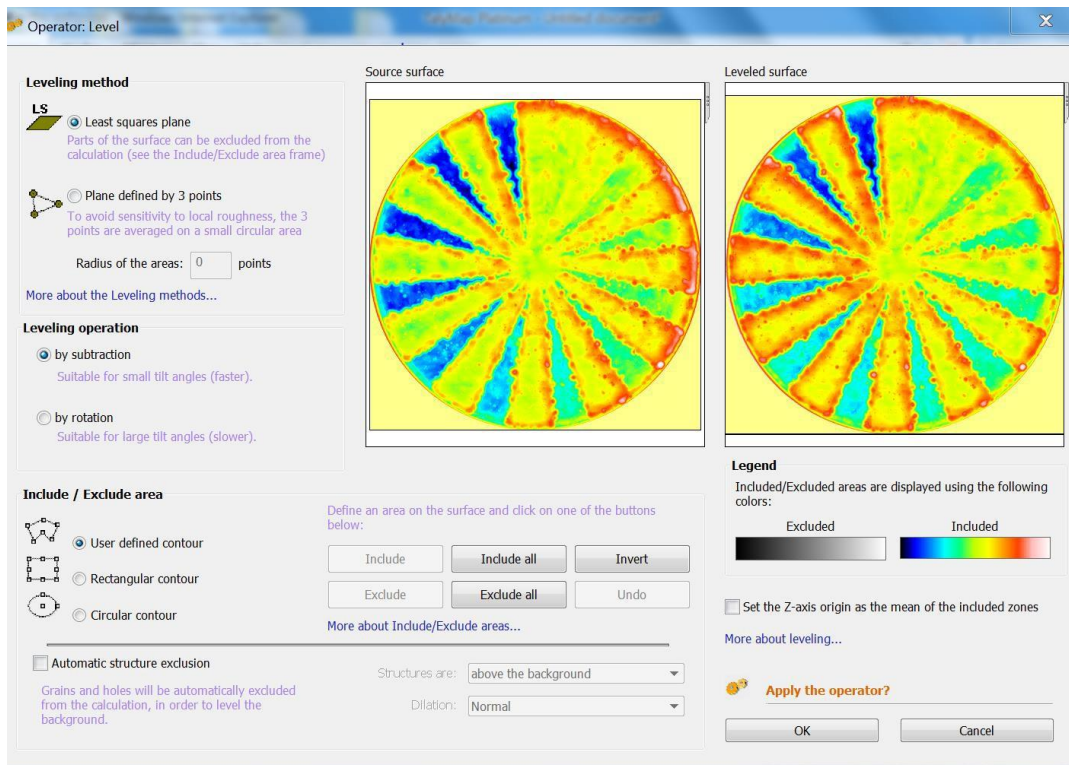


Average measured width and standard deviations for Sample 5



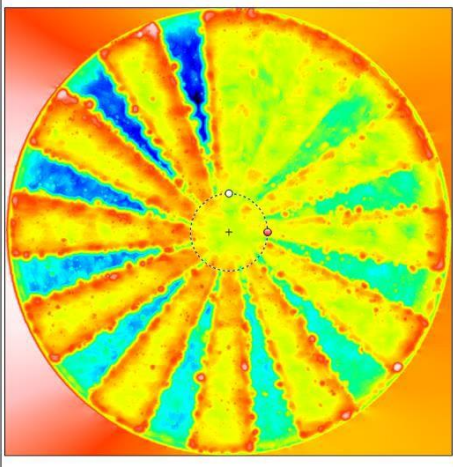
Average measured width and standard deviations for Sample 6.

9.2 Appendix 2: Chapter 5



Procedure for Extracting Profiles Leveling Operation

Operator: Extract profile



Extraction type

West-East
 North-South
 Oblique
 Zigzag
 Circular
 X-Axis in degrees

Direction

Click on the button below to change the direction of the circular extraction.

ClockWise
 AntiClockWise

Units

Points
 mm
 %

Center

Radius

Profile

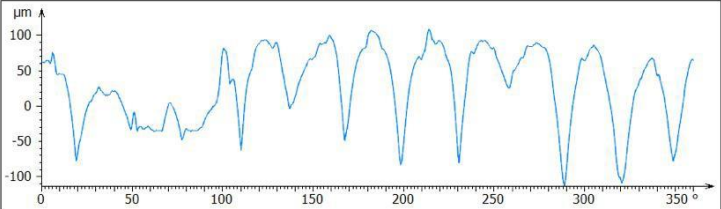
360 °
2792 points

Z-range used for preview

Profile resolution
 Surface resolution

Apply the operator?

OK Cancel

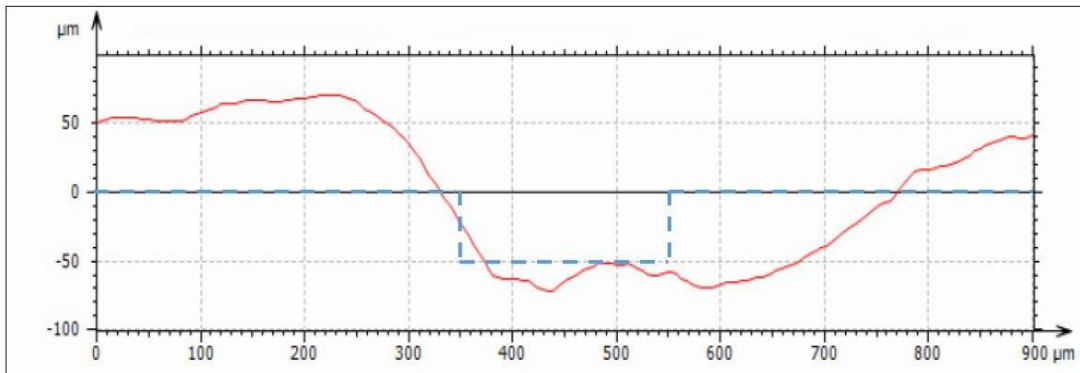


Extract Profile Operation

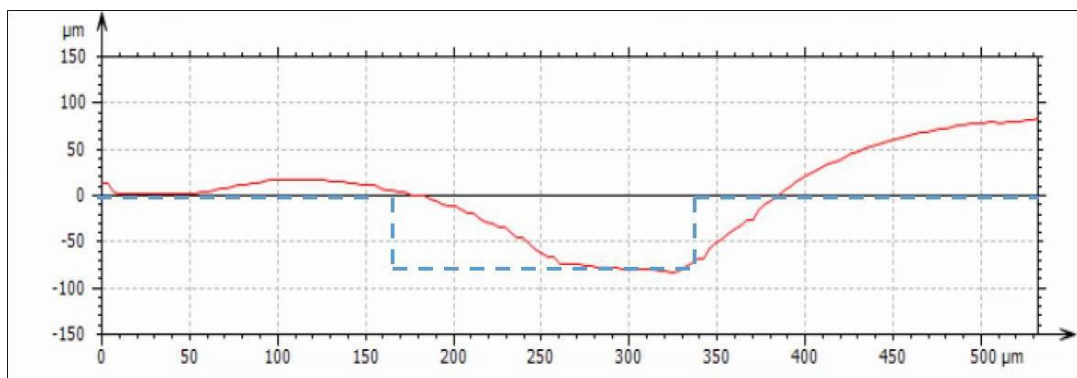
Parameter Table for Defining Extracted profile radius.

Measured Radius (mm)	Feature width (mm)
1	0.000
1.05	0.000
1.1	0.000
1.15	0.000
1.2	0.000
1.25	0.000
1.3	0.000
1.35	0.000
1.4	0.013
1.45	0.026
1.5	0.039
1.55	0.053
1.6	0.066
1.65	0.079
1.7	0.092
1.75	0.105
1.8	0.118
1.85	0.132
1.9	0.145
1.95	0.158
2	0.171

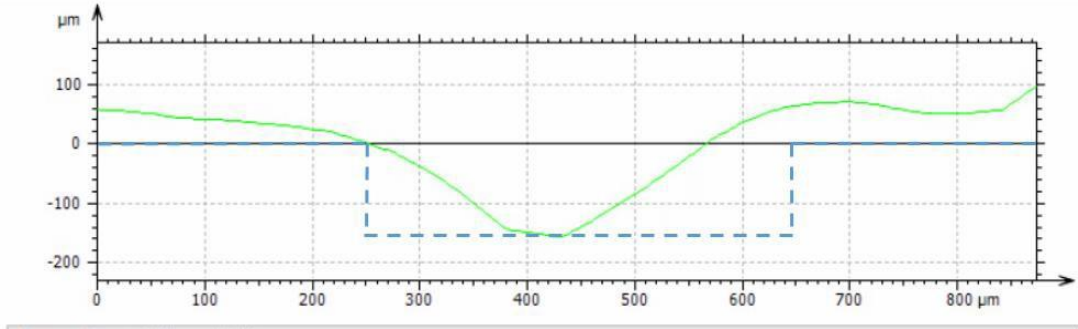
Measured Radius (mm)	Feature width (mm)
2.05	0.184
2.1	0.197
2.15	0.211
2.2	0.224
2.25	0.237
2.3	0.250
2.35	0.263
2.4	0.276
2.45	0.290
2.5	0.303
2.55	0.316
2.6	0.329
2.65	0.342
2.7	0.355



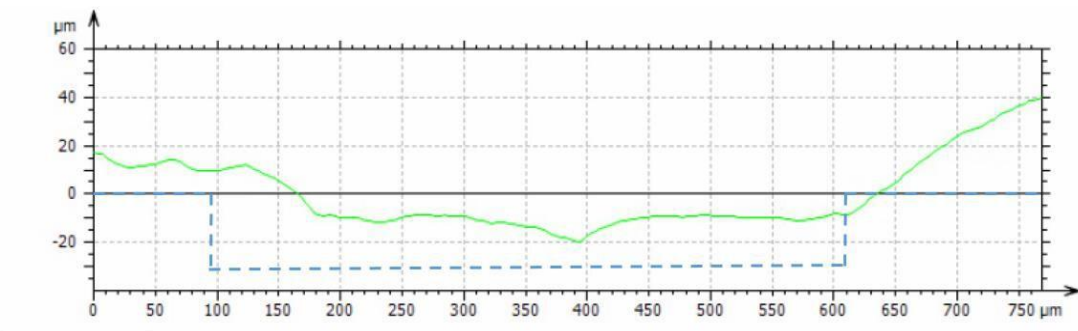
Comparison between measured (red) and design feature (dotted blue) for 0.2mm spacing and 50µm feature height.



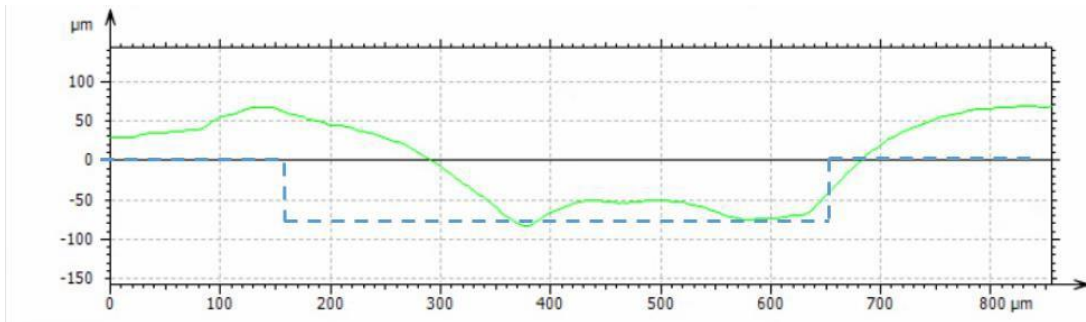
Comparison between measured (red) and design feature (dotted blue) for 0.2mm spacing and 75µm feature height.



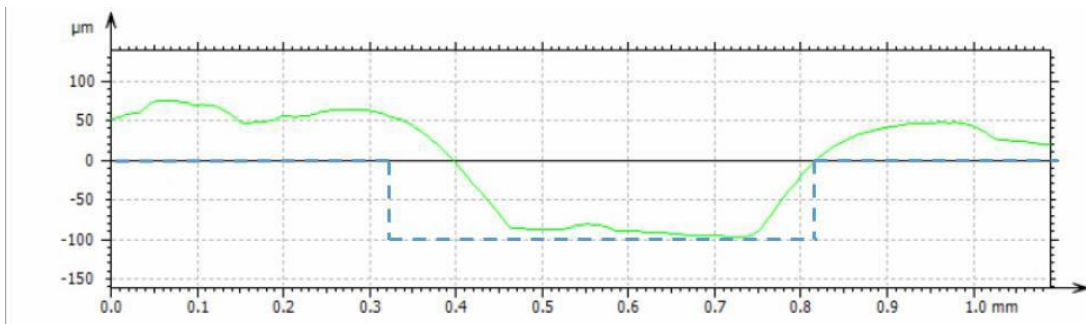
Comparison between measured (green) and design feature (dotted blue) for 0.4mm spacing and 175 μm feature height



Comparison between measured (green) and design feature (dotted blue) for 0.5mm spacing and 25 μm feature height.



Comparison between measured (green) and design feature (dotted blue) for 0.5mm spacing and 75µm feature height.



Comparison between measured (green) and design feature (dotted blue) for 0.5mm spacing and 100µm feature height.